SCUOLA DI DOTTORATO
UNIVERSITÀ DEGLI STUDI DI MILANO-BICOCCA

Department of

Physics

PhD program in Physics and Astronomy Cycle XXXI

Curriculum in Subnuclear Physics and Physics Technologies

Advances in instruments and methods for neutron transmission imaging

Surname Vitucci Name Giuseppe

Registration number 805464

Tutor: Prof. Francesco Terranova

Co-tutor: Prof. Giuseppe Gorini

Supervisor: Dr. Triestino Minniti

Coordinator: Prof. Marta Calvi

ANNO ACCADEMICO / ACADEMIC YEAR 2017-2018

UNIVERSITÀ DEGLI STUDI DI MILANO-BICOCCA

Department of Physics

Ph.D. Program in Physics and Astronomy – XXXI cycle

ADVANCES IN INSTRUMENTS AND METHODS FOR NEUTRON TRANSMISSION IMAGING

Ph.D. Thesis of

GIUSEPPE VITUCCI

Tutor: Prof. Francesco Terranova

Co-tutor: Prof. Giuseppe Gorini

Supervisor: Dr. Triestino Minniti

Coordinator: Prof. Marta Calvi

Academic year: 2017 - 2018

– Puoi compilare questo documento?–
– Quando è la deadline? –
– Era ieri –
"Il Dottorato", Capitolo I.

Contents

List of papers

I. W. Kockelmann, T. Minniti, D. E. Pooley, G. Burca, R. Ramadhan, F. A. Akeroyd, G. D. Howells, C. Moreton-Smith, D. P. Keymer, J. Kelleher, S. Kabra, T. L. Lee, R. Ziesche, A. Reid, **G. Vitucci**, G. Gorini, D. Micieli, R. G. Agostino, V. Formoso, F. Aliotta, R. Ponterio, S. Trusso, G. Salvato, C. Vasi, F. Grazzi, K. Watanabe, J. W. L. Lee, A. S. Tremsin, J. B. McPhate, D. Nixon, N. Draper, W. Halcrow and J. Nightingale. "Time-of-Flight Neutron Imaging on IMAT@ISIS: A New User Facility for Materials Science". *Journal of Imaging 4.3. 2018. p.47.*

II. **G. Vitucci**, T. Minniti, D. Di Martino, M. Musa, L. Gori, D. Micieli, W. Kockelmann, K. Watanabe, A.S. Tremsin and G. Gorini. "Energy-resolved neutron tomography of an unconventional cultured pearl at a pulsed spallation source using a microchannel plate camera". *Microchemical Journal 137. 2018. 473-479.*

III. **G. Vitucci**, T. Minniti, G. Angella, G. Croci, A. Muraro, C. Höglund, C. C. Lai, E. Perelli Cippo, G. Albani, R. Hall-Wilton, Linda Robinson, G. Grosso, M. Tardocchi and G. Gorini. "Measurement of the thickness of B4C deposits over 3D grids via multi-angle neutron radiography". Under review. *Measurement Science and Technology.*

IV. T. Minniti, A.S. Tremsin, **G. Vitucci** and W. Kockelmann. "Towards high-resolution neutron imaging on IMAT". *Journal of Instrumentation. Vol 13. 1. 2018.*

V. **G. Vitucci**, T. Minniti, A.S. Tremsin, W. Kockelmann and G. Gorini. "Investigation of image distortion due to MCP electronic readout misalignment and correction via customized GUI application". *Journal of Instrumentation. Vol.13. 4. 2018*

Abstract

The work presented in this thesis focuses on the development and improvement of instrumentation and methods applied to neutron transmission imaging. In particular, the research activities have been performed at the "Imaging and Materials Science and Engineering" (IMAT) instrument.
This facility is a part of the ISIS neutron source at the Rutherford Appleton Laboratory, in UK. The neutrons here are produced by spallation reactions of a tungsten target hit by protons with energy of 800 MeV. The resulting neutrons are then slowed down by a 18 K hydrogen moderator and convoyed through beam guides towards the IMAT experimental area. The neutrons spectrum in this case is characterized by the presence of thermal and cold neutrons with a wavelength in the range of 0.68 - 6.8 Å.
IMAT has been designed to acquire neutron pulses in Time-Of-Flight mode, by recording the time of arrival of neutrons, related to their energy, with a maximum of 10 ns timing resolution. This analysis is performed with a new generation detector, that is a combination of a MicroChannel Plate neutron converter with a quad Timepix electronic readout. By means of this apparatus, radiographies and tomographies with a field of view of 28 mm^2 can be generated with a spatial resolution of 55 µm and with respect to specific neutron energies. Beside this device, a larger CMOS camera can be used in combination with ^{6}LiF/ZnS based neutron screen scintillators to acquire images up to 211 $\times$ 211 mm^2 in white-beam imaging.
Such a configuration opens several possibilities in different case scenarios. In one hand, the energy-resolved neutron imaging technique can be used to investigate the phase fraction composition and texture of the samples via Bragg Edge analysis software tools, at the cost of a reduced field of view. On the other hand, bigger samples can be studied with standard CMOS or CCD based white-beam imaging cameras, but loosing any information about the energy of the incoming neutrons.
In this work, the first part is devoted to the description of the IMAT instrumentation, including the beamline design, the experimental area and the detectors.
The second part is directed to case studies that made use of these novel instrumentation and imaging techniques. In particular, the cultural heritage science takes advantage of such non-destructive methods where small and delicate specimens must be analysed. In this class of examples, a "soufflè" pearl was considered. The peculiarity of these cultured pearls resides in the fact that they are empty inside. The inspection of the morphological structure of the inner part, as well as the individuation of the different orientations of the nacres crystallites was conducted with

energy-resolved imaging techniques. A second experiment, presented in this thesis, regards the diagnosis of a batch of metallic grids with a size up to 200 $\times$ 10 mm^2. For this case, a fast and non destructive way to verify the thickness of 1 µm boron carbide layer deposited over their lamellae was successfully implemented, within an uncertainty of 120 nm.
The third part is directed to show two new methods developed to improve the MCP detector camera in terms of spatial resolution and reliability. For what concerns the spatial resolution, a new procedure based on a centroiding algorithm has been tested. This acquisition method enables the possibility to go over the physical constraint given by the dimension of the pixels of the electronic readout and to acquire images with a resolutions up to four times higher. Furthermore, an improvement to the resulting images generated by the MCP detector has been developed, based on a post-processing approach. Actually, one of the weak spots of the quad Timepix readout installed on the MCP detector is that it is constituted by four matrices of pixels assembled together. This brings to noticeable artifacts which, in some cases, may produce issues in the data analysis. A procedure, including a customized software, was implemented to fix such a problem.
Finally, the summary of the results brought by the aforementioned works is given, with a discussion on the future improvements at the IMAT facility.

1 | Neutron Imaging: a background

1.1 Neutron physics

The neutron is one of the subatomic particles constituting the nucleus of an atom. Among its most relevant peculiarities, there is the absence of an electric charge, which makes it capable of penetrating the coulombian barrier of the target atoms and interacting directly with their nuclei.
Free neutrons can be created naturally, for instance by the interaction of cosmic radiations with the molecules permeating our atmosphere, or by means of artificially created nuclear reactions, such as the fission [1] and spallation reactions [2]. There are two main kinds of interactions that can have place between free neutrons and target nuclei [3]:

1. **Absorption**. The target nucleus captures the incoming neutrons. At this point, the result may be the fission of the target (n,f) or its excitation followed by the emission of electromagnetic radiations (n,γ), charged particles (n,p),(n,α) ... or neutrons (n,Nn), where $N \in \mathbb{N}, N \geq 1$.

2. **Scattering**. The incoming neutron suffers from a change in its propagation after its interaction with the target nucleus. In the case that the neutron kinetic energy is not transferred to the nucleus, this process is named *elastic* scattering. On the other hand, if its energy changes, the process is classified as *inelastic* scattering.

Such interactions have a certain probability to happen, related to the kind of target nucleus and the neutron velocity or, in equivalent way, its energy or wavelength. In fact from the classical expression for the kinetic energy:

$$E = \frac{m_n v^2}{2} = \frac{p^2}{2m_n} \tag{1.1}$$

with E being the kinetic energy of the neutron, m_n its mass, v its velocity and p the particle momentum, one can use the relation given by the DeBroglie law, which associates the momentum of a moving particle to the wavelength λ through the Planck constant h in the following way:

$$\lambda = \frac{h}{m_n v} = \frac{h}{p} \tag{1.2}$$

Energy	**Wavelength**	**Energy Classification**
$0 \rightarrow \sim 0.025$ eV	$\gtrsim 1.8$ Å	cold
~ 0.025 eV	~ 1.8 Å	thermal
~ 0.025 eV $\rightarrow \sim$100 eV	~ 1.8 Å$\rightarrow \sim 0.028$ Å	epithermal
~ 100 eV $\rightarrow \sim$ 1MeV	0.028 Å$\rightarrow \sim$ 2.8E-4 Å	slow
$\sim$ 1MeV $\rightarrow \sim$ 20 MeV	2.8E-4 Å$\rightarrow \sim$ 9.0E-5 Å	fast

Table 1.1: Classification of neutrons with respect to their energy (in electronvolts) and wavelength (in Ångstrom).

Inserting the momentum in the equation 1.1, one finally gets:

$$E = \frac{h^2}{2m_n\lambda^2} \tag{1.3}$$

showing the inverse proportionality between the neutron energy and its wavelength.

Actually, two methods are often use to generate neutrons: fission [4] and spallation nuclear reactions[5]. In the first case, fissile atomic nuclei, such as ^{235}U, are bombarded with neutrons and undergo nuclear fission, splitting into two atomic nuclei and releasing further free neutrons. In the second case, protons are accelerated at high energy, usually $\sim$ 800 MeV, and launched in short pulses towards a heavy-metal target. When they collide with the target, the latter is fragmented into several smaller particles, gamma rays and free neutrons.
In both cases, the neutrons coming out from the source after the reaction have, usually, much more energy than needed for condensed matter physics and must be slowed down, with a process called *moderation*. It is common to define several energy ranges classifying the neutrons with respect to their "temperature" (Tab. 1.1). The neutrons, when in thermodynamic equilibrium with the moderator medium, have an energy distribution described by the Maxwell-Boltzmann function [6]:

$$N(E) = \frac{2\pi N_0}{(\pi kT)^{3/2}} \cdot \sqrt{E} \cdot e^{-\frac{E}{kT}} \tag{1.4}$$

with $N(E)$ being the number of neutrons at a particular energy E, k the Boltzmann constant, N_0 the total number of neutrons per unit volume and T the temperature. From the 1.4, the average energy can be deduced:

$$E_{avg} = \frac{\int_0^\infty N(E)E\,\mathrm{d}E}{\int_0^\infty N(E)\,\mathrm{d}E} = \frac{3}{2}k_BT \tag{1.5}$$

which states the direct proportionality between the neutron energy and the moderator temperature (Fig.1.1).

The neutron absorption probability is, generally, inversely proportional to the neutron velocity, while the scattering probability has a more irregular trend (Fig. 1.2).

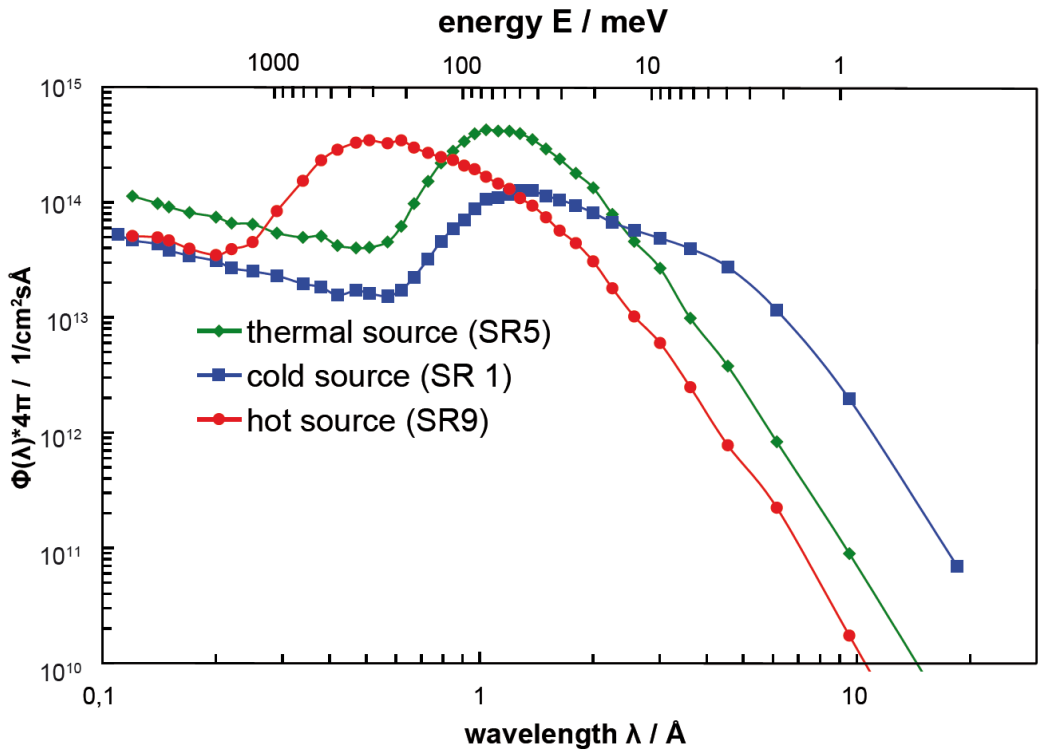

Figure 1.1: Neutron spectra moderated by cold, thermal and hot media at FRM II reactor, MLZ research centre[7]. The higher the temperature, the more the peaks of the gaussian neutron energy distributions move towards higher values.

Such interaction probability is called *cross-section*, and it is measured in *barns*, defined as 10^{-24} cm^2. Furthermore, there are two ways to refer to this likelihood of interaction:

1. the **microscopic cross section**, usually defined with σ, which describes the interaction probability of a neutron with a single nucleus. It can be defined by the following:
$$\sigma = \frac{C}{\Delta t} \cdot \frac{1}{\Phi} \cdot \frac{1}{N_t} \tag{1.6}$$
where C is the number of the events occurred, Δt the unit of time, Φ the neutron flux per unit of time and N_t the number of nuclei in the target. This value shows the probability of interaction per single target nucleus and has the dimension of an area;

2. the **macroscopic cross section**, indicated with Σ, is defined as follows:
$$\Sigma = \sigma \cdot N \tag{1.7}$$
with N being the nuclei density in the target and having the dimension of [cm^{-3}]. Such a value shows the likelihood of the interaction considering all the nuclei contained in the target.

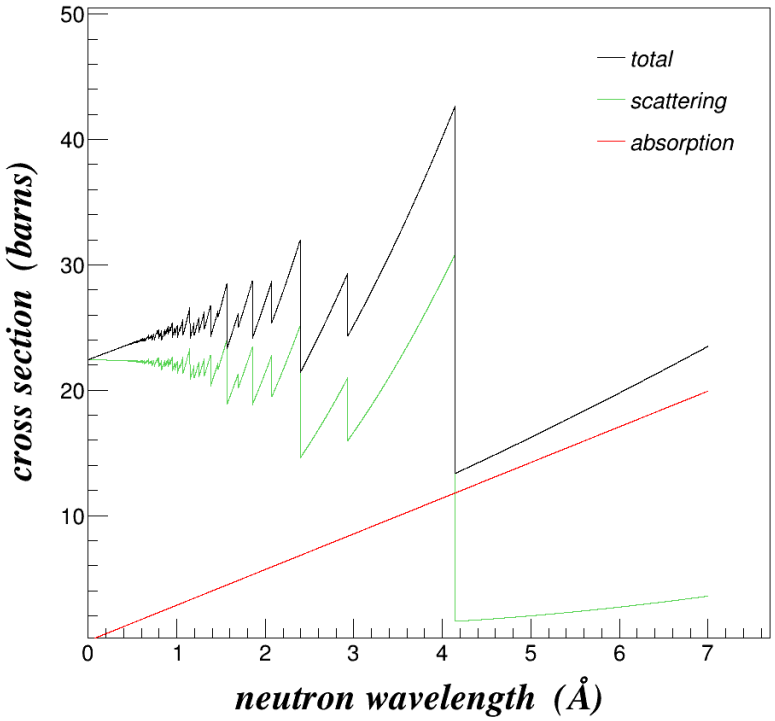

Figure 1.2: Dependence of the absoprtion and the scattering cross sections with respect to the neutron wavelength, for the ferrite. The total cross section, given by their sum, is also shown.

On the other hand, there are further phenomena affecting the neutron cross-sections. For instance, the thermal neutron scattering is influenced by the interaction of the strong forces depending on the detailed structure of the nuclei [8]. Such parameter is called *scattering length* and it is generally indicated with b. A first order estimate of it can be done with quantum mechanics arguments, determining a relation between the scattering length and the radius and the potential well of the target nucleus [9]. It's clear that the scattering cross section thus varies among the isotopes of the same element.
In the case that no interaction between the free neutrons and the target atoms occurs, the phenomenon of *transmission* takes place.
There are different types of experiments exploiting the neutron-nucleus interactions, ranging from diffractometry, spectrometry and radiography [10]. In particular, this work focuses on the imaging technique, where the transmitted neutrons are revealed and analysed to create two- and three-dimensional representations of the sample under study.

1.2 Neutron imaging technique

1.2.1 Overview

The story of neutron imaging starts about a century ago, when the first attempts to produce neutron radiographies of objects were made, to get an idea of the potentiality that such a new technique could bring to scientific research (Fig.1.3). Today,

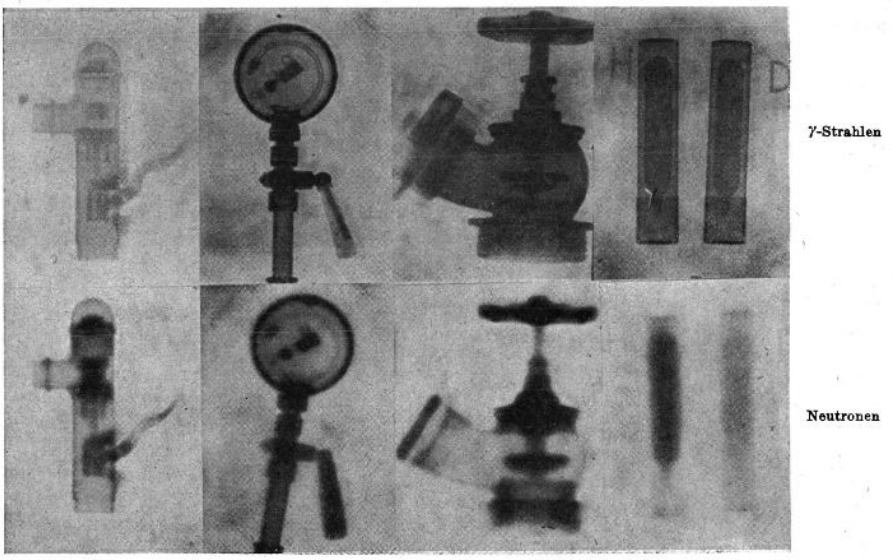

Figure 1.3: Neutron radiography compared with γ-ray radiography [11], 1946.

despite the issues related to the cost and the difficulties of realizing neutron instrumentation, especially if compared to X-ray technique, neutron imaging is still a well-established method with a positive future outlook [12]. Actually, there are numerous remarkable advantages which make this technique attractive: for instance, the nuclear interaction of the neutron with the target nucleus allows to reveal light elements, like hydrogen, and also to distinguish between isotopes of the same element. Also, heavy materials, like lead or titanium, may be easily penetrated in a non-destructive way.
The outcome of experimental neutron imaging techniques are images whose contrast is determined by the level of interaction between the neutrons and the sample under analysis. The higher the interaction, the higher the contrast obtained in the output image, the clearer the result.
Different phenomena can be exploited for this purpose [13]. Among the most relevant one can cite:

- the mechanisms of absorption and scattering of neutrons impinging the target nuclei, described by the related cross sections[14, 15];
- the phase shift of the neutrons intended as *de Broglie* waves, imposed by the structure of the sample [16] ;

- the magnetic polarization of neutrons influenced by the sample magnetic field [17]

Each technique is especially efficient in probing a particular aspect of the sample, ranging from the morphological structure, the material composition or the crystalline orientation of its atomic structure.

1.2.2 Transmission imaging

The transmission imaging technique takes into account the different contributions to the total cross sections over a neutron beam passing through a sample. In fact, the incident beam will suffer of a loss of intensity which can be mapped by a position sensitive neutron detector placed behind the specimen. By the mathematical point of view, this attenuation of the intensity I of the beam can be expressed with a differential equation. In fact, if one wants to calculate the intensity variation suffered by the beam passing through the sample of thickness t along the z-direction:

$$\frac{\partial I(x,y,z,E)}{\partial z} = -N\sigma(x,y,z,E)I(x,y,z,E) \tag{1.8}$$

stating that the rate of change of the beam intensity is given by the total microscopic cross sections of the target nuclei (that are a function of the impinging neutrons energy E) and N, the number of nuclei per volume. The solution, also known as Lambert-Beer law, is:

$$I_{tr}(x,y,E) = I_0(x,y,E)e^{-\int_0^t N\sigma(x,y,z,E)\,\partial z} = I_0(x,y,E)e^{-\int_0^t \Sigma_{tot}(x,y,z,E)\,\partial z} \tag{1.9}$$

where ∂z is integrated with respect to the path length of the neutrons through the sample. This gives the value of the transmitted beam I_{tr} as result of the exponential attenuation of the entering beam I_0 related to the total macroscopic cross section Σ.
A further aspect concurs in the formation of the output image: the beam divergence. In a typical experimental setup, the main parameters to consider are:

1. the pinhole diameter, that is the aperture size from which the neutrons are coming out to be directed towards the sample;

2. the distance between such aperture and the detector;

3. the distance between the sample and the detector.

In Fig. 1.4, a sketch about the relation of these parameters is shown. The L/D ratio has a primary importance, because it defines the "geometric blur" of the radiography. This phenomenon, recognizable as a shadow around the edges of the image, is given by:

$$\lambda_g = \frac{zD}{L-z} \approx \left.\frac{zD}{L}\right|_{L\gg z} \tag{1.10}$$

and it can be reduced either by decreasing the size of the pinhole, or increasing the distance between the pinhole and the detector. In both case, the drawback is the significant reduction of the flux directed towards the sample. A third option is to place the sample as close as possible to the detector, i.e. decreasing the z value. In this way, λ_g is again reduced, but the detector is more likely to be exposed to background noise, such as γ-radiations coming from the activation of the sample. To further push the precision of the acquisition systems, new optical solutions are under development [18, 19].

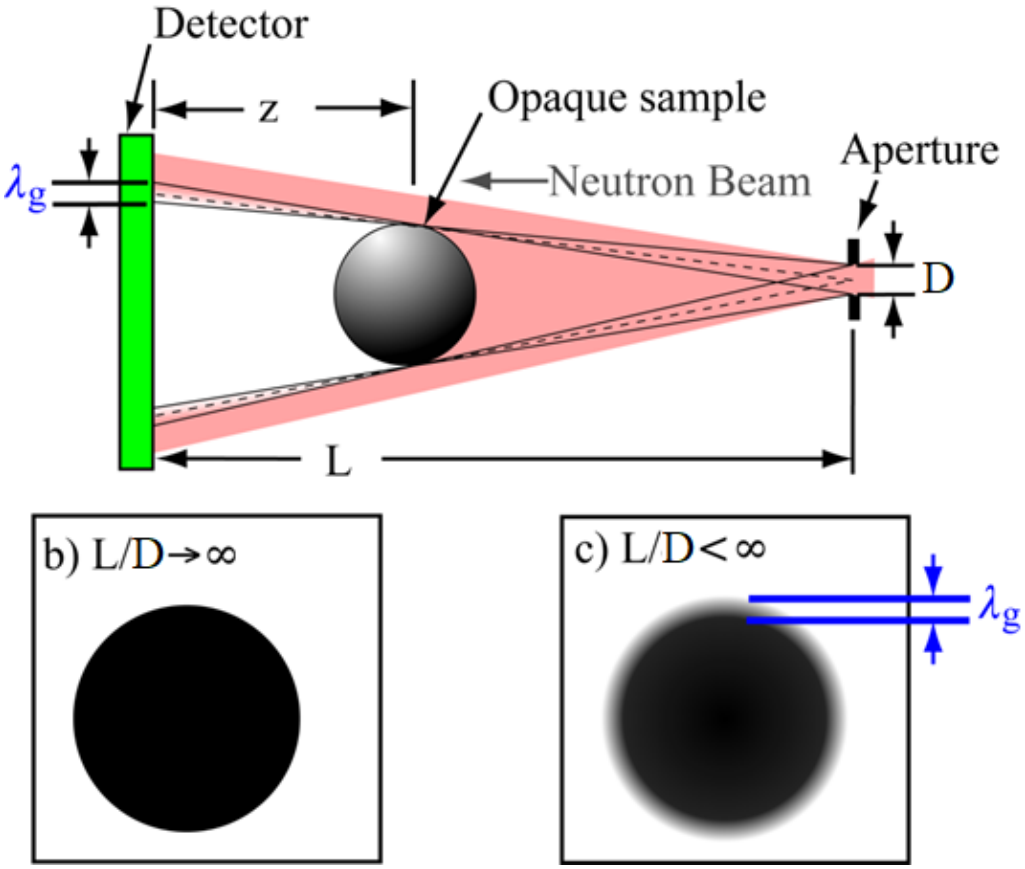

Figure 1.4: Image formation by neutron radiography technique [20].

Not only the optics, but also the intrinsic detector resolution plays a role in the determination of a clear radiography. The resolution can be intended in two ways: the *contrast* resolution and the *spatial* resolution.
In the first case, one refers to the gray scale representation given by the imaging detector. Actually, modern electronic-based detectors digitize the intensity variation of the signal they record in the form of a shift range from a absolute black (usually associated to the value of 0) to absolute white (with a value equal to 2^n, where n is the number of the bits of the data register where such value is saved). The higher the number of the bits available, the wider the gray scale, the lower the measurement error, as showed by (Fig.1.5).
In the second case, the pixel size defines the minimum appreciable feature of the

sample. Generally, the lower this parameter, the higher the resolution. Nonetheless, when the pixel size gets smaller, the probability of revealing neutrons decreases as well, since it is proportional to the detecting area of each pixel. This affects the signal to noise ratio (SNR). Therefore, a balance must be reached between these two aspects.

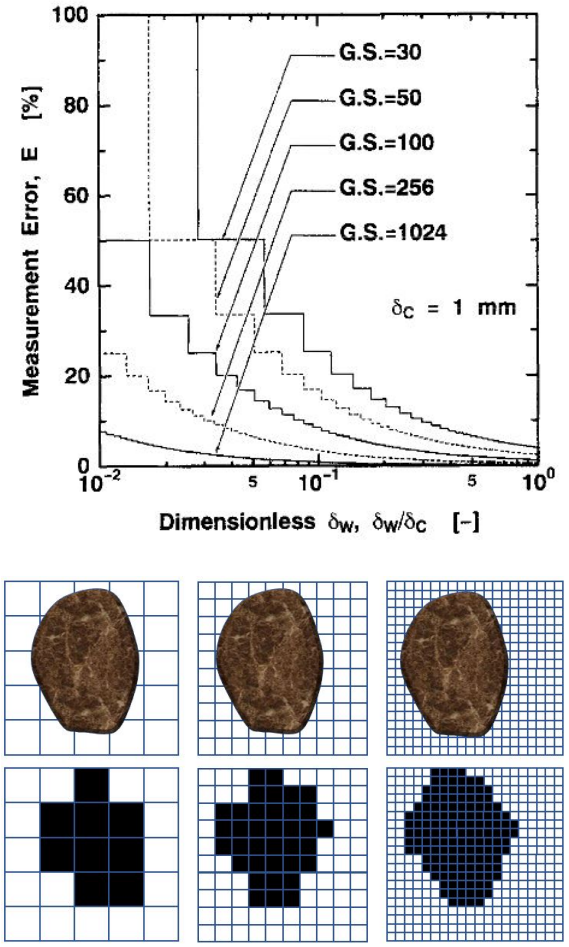

Figure 1.5: Top: Dependence of the measurement error of the thickness δ_w of a water sample normalized to its maximum thickness δ_c. The descrepancy grows when the sample becomes thinner and it is reduced when a larger gray scale is used [21]. Bottom: Difference between original and acquired shape due to pixel resolution.

1.2.3 Tomographic reconstructions

An important extension to the acquisition of single radiographies can be applied when the knowledge of the volumetric shape of the sample under analysis is needed. In fact, the computed tomography technique permits the three-dimensional reconstruction of the specimen, assuming that at least a minimum number of radiographies (projections of a three-dimensional sample onto a two-dimensional plane, i.e.

the detector) at different angles is acquired. This number is defined by the following equation [22]:

$$N_p = \pi \frac{D_{min}}{2} \tag{1.11}$$

with N_p being the required number of projections and D_{min} the ratio between the maximum width of the sample and the pixel size of the electronic readout.

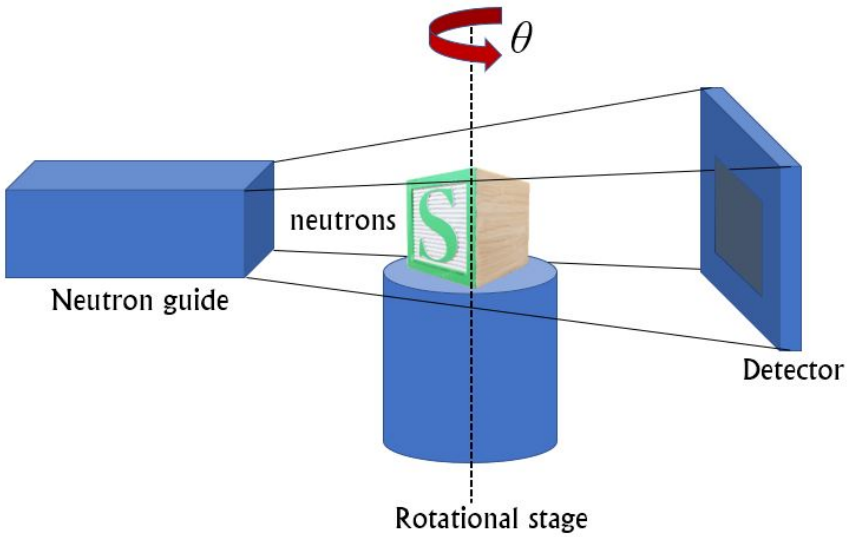

Figure 1.6: Sketch of the multiple radiography acquisition system by sample rotation available at IMAT .

The theorethical basis of such method was given by Radon in 1917 [23], where he defined a generic line function $p(t, \theta)$, or projection function, whose points result from the linear integration of a function of two variables $f(x, y)$ satisfying suitable regularity conditions. The coordinate t represents the distance of the projection lines from the center of the xy plane, while θ is the angle between the projection lines and the x-axis (Fig.1.7). This relation can be expressed with the following:

$$p(t, \theta) = \int_L f(x(s), y(s))\, ds \tag{1.12}$$

with L being the family of the integration lines. This equation is known as Radon transform.
The line function $p(t, \theta)$ is, in other words, a sum of the values of the two-dimensional function f taken at the angle θ. By the experimental point of view, the integration lines can be seen as the neutron rays passing through the sample, while the function $f(x, y)$ describes the spatial distribution of the cross section values in the sample. Finally, $p(t, \theta)$ is the neutron radiography of the sample taken at a particular angle. In this model, several approximations are made, such as the assumption that all the beams passing through the sample are parallel and with the same energy. Also, scattered neutrons are neglected.

The fastest way to reconstruct the original function $f(x, y)$ is based on the "smearing" of the values of the line functions over the related integration lines (this process is called back-projection) and the sum of the results for all the projection angles (Fig. 1.8). The higher the number of considered angles, the better the result. Nonetheless, this technique has an intrinsic problem, since by summing non-negative functions (the projection functions) each point in the image receives non-negative contributions from its neighbours [22]. This brings to a "blurring effect" onto the resulting reconstruction, which can be described by the following equation:

$$g(x, y) = f(x, y) \times \frac{1}{\sqrt{x^2 + y^2}} \tag{1.13}$$

Nevertheless, there are several techniques to solve this problem. Two of the most diffused ones are called "filtered back-projections" (in short FBP), based on the relation between the Radon transform and the Fourier transform, and the "Algebraic Reconstruction Technique" (or ART), which is based on an iterative scheme of convergence. [24]

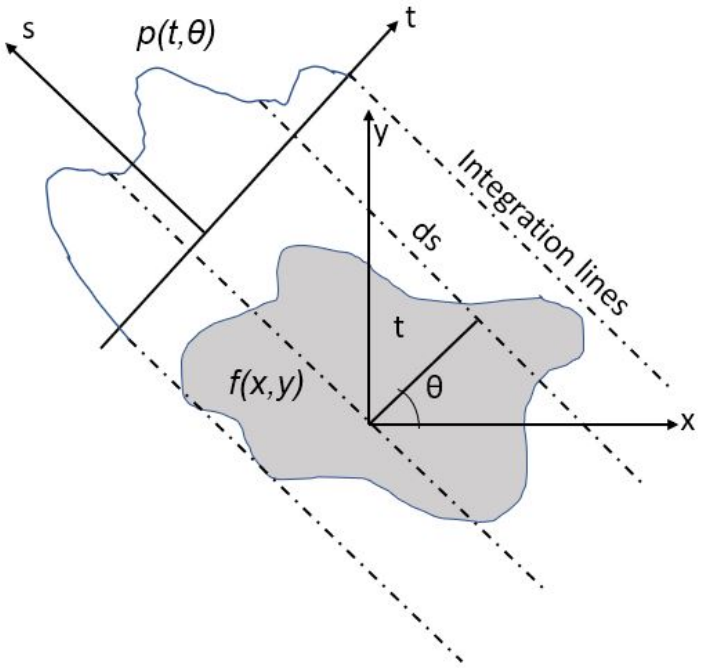

Figure 1.7: Representation of the projection function $p(t, \theta)$. The points in this function are the result of the sum of the values of the (x, y) points of the function $f(x, y)$ taken along the integration lines.

Filtered Backprojection

The Filtered Backprojection technique is based on the relation between the Radon transform and the Fourier transform. In fact, it is possible to demonstrate (Central

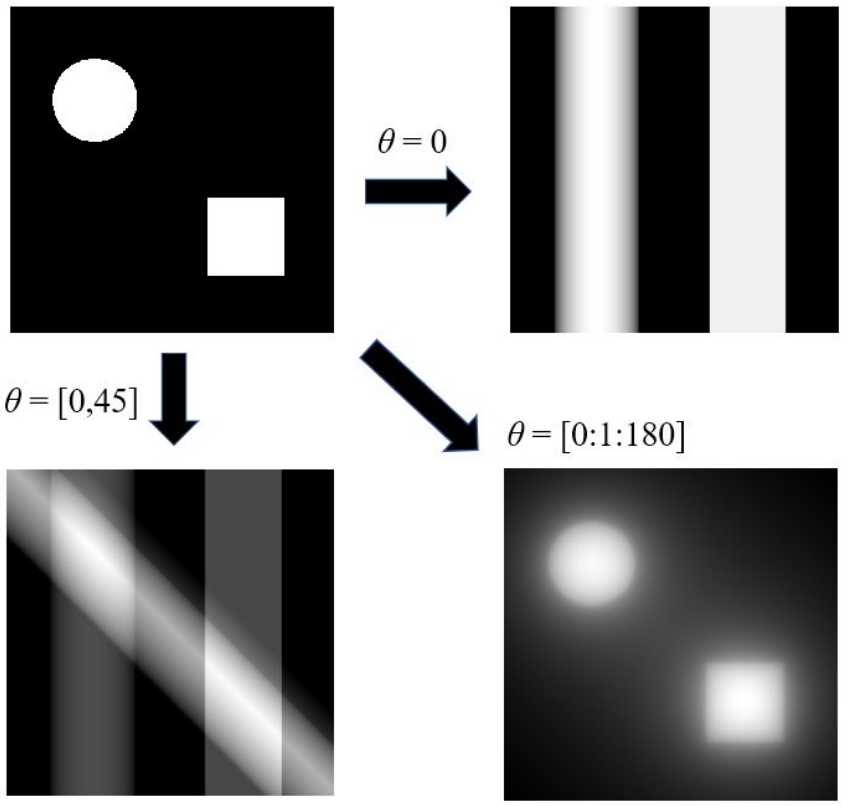

Figure 1.8: Image reconstruction through simple back-projection superposition. In the top left panel the original figure is shown. In the top right panel, a single back-projection at the angle $\theta = 0$ is applied. In the bottom left, two back-projections at $\theta = 0$ and $\theta = 45$. Bottom right: all the integer angles in between 0° and 180° have been considered. The higher the number of angles considered, the better the result. Nontheless, the blur is still present.

Slice Theorem) that there is an equivalence between the central section of the two-dimensional Fourier transform of $f(x, y)$ taken at an angle θ' and the one-dimensional Fourier transform of the function projection $p(t, \theta')$ [25]. This can be summerized by the following equation:

$$\mathscr{F}_1\{p(t, \theta')\} = \mathscr{F}_2\{f(x, y)\}_{|\theta=\theta'} \tag{1.14}$$

Therefore one can express the initial function $f(x, y)$ via the inverse Fourier transform:

$$f(x, y) = \mathscr{F}_2\{F(v_x, v_y)\} = \int_{-\infty}^{+\infty} dv_x \int_{-\infty}^{+\infty} dv_y F(v_x, v_y) e^{2\pi i(v_x x + v_y y)} \tag{1.15}$$

with v_x and v_y being the coordinates in the frequency domain. With a change to the polar coordinates $v_x = \omega \cos\theta$, $v_y = \omega \sin\theta$ and $dv_x dv_y = \omega \, d\omega \, d\theta$, Eq.1.15 becomes:

$$f(x,y) = \int_0^{2\pi} d\theta \int_0^{+\infty} d\omega\, \omega F(\omega\, cos\theta, \omega\, sin\theta) e^{2\pi i \omega (x\cos\theta + y\sin\theta)} \tag{1.16}$$

Since in the $[0, 2\pi)$ interval the following relation holds:

$$F(w, \theta + 180°) = F(-w, \theta) \tag{1.17}$$

changing the integration limits and considering the equivalence defined by the Central Slice Theorem in 1.14, the Eq.1.16 can be rewritten as:

$$f(x,y) = \int_0^{\pi} d\theta \int_{-\infty}^{+\infty} d\omega\, |\omega| P(\omega, \theta) e^{2\pi i \omega (x\cos\theta + y\sin\theta)} \tag{1.18}$$

where ω is the ramp filter operating on the projection function. Eq.1.18 sums up the routine for the tomography reconstruction via filtered back-projections:

1. One-dimensional Fourier transform of projections $p(t, \theta)$;
2. Multiplication by the filter ω;
3. One-dimensional inverse transform of this product;
4. Back-projection of the filtered projection;
5. Sum over all the filtered back-projections.

Algebraic reconstruction technique

An alternative approach to the image reconstruction can be carried out using the so called "algebraic reconstruction techniques". These ART methods rely on the fact that the sample projections are always discretized, due to the inner technical design of the detectors based on pixel matrices. In fact, the whole image is represented by a system of linear equations in the form:

$$\begin{cases} a_{11}f_1 + a_{12}f_2 + \dots\ a_{1N}f_N = p_1 \\ a_{21}f_1 + a_{22}f_2 + \dots\ a_{2N}f_N = p_2 \\ \qquad\qquad \vdots \\ a_{M1}f_1 + a_{M2}f_2 + \dots\ a_{MN}f_N = p_M \end{cases} \tag{1.19}$$

with M and N the total number of projections and detector pixels respectively. Such equations state that every projection p determined by a single ray passing through the sample is the sum of the contributions f_{ij} given by each pixel in the image weighted by a parameter a_{ij}, which takes into account the effective amount of the contribution given by that single ray in the pixel.
Typically, the most precise method considers the area of the pixel irradiated by the ray divided by the total pixel area (strip model), but there are other ways to

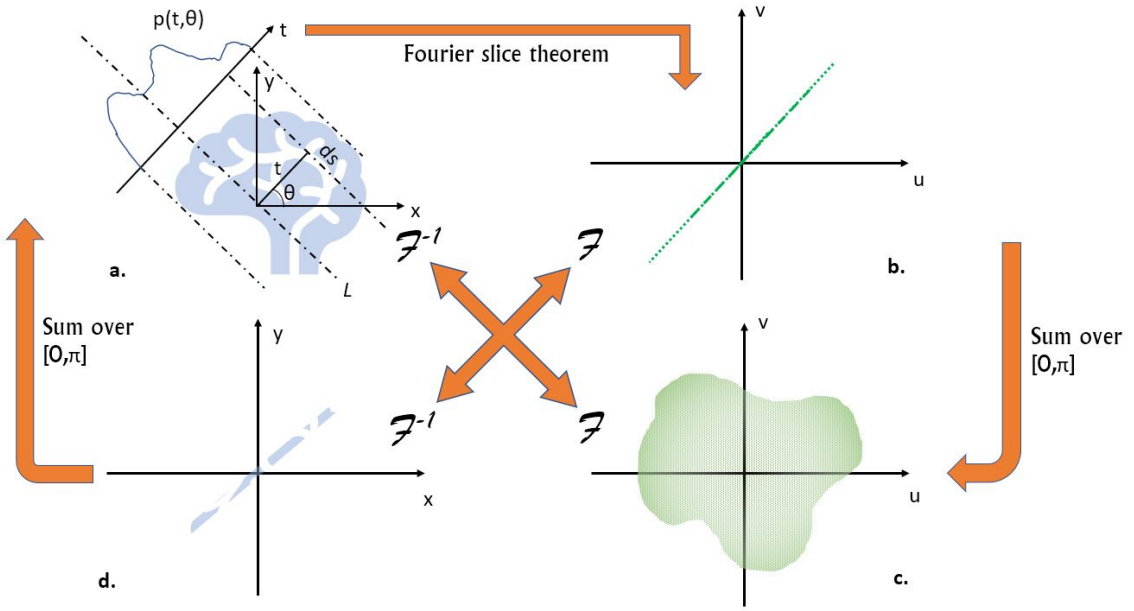

Figure 1.9: Example of image analysis through filtered backprojection algorithm. In (a), the sample is radiographed at angle θ and the projection function $p(t,\theta)$ is created. This projection is equivalent to the one dimensional Fourier transform at same angle passing through the origin of the coordinate system in the Fourier space (b). By collecting all the projections and Fourier transforming them at all the angles in the [0,π] range, one can get the full two-dimensional Fourier transform of the original image (c). The less computationally expensive way to reconstruct the image is the one-dimensional inverse Fourier transform (d) of the slice in (b) and summing for all the angles.

quantify such weighting parameters, such as the line length method or the Joseph's method [26]. Eq. 1.19 can be presented as a $M \times N$ matrix multiplied by a vector, in the form:

$$p = \mathbf{A}f \tag{1.20}$$

with p being the vector of the projection values, $\mathbf{A}$ the matrix of the weighting factors and f the attenuation values expressed by the pixels forming the image. In such equation $\mathbf{A}$ is interpreted as the Radon transform operator.
The most direct way to obtain the vector of the attenuation values is the calculation of the matrix $\mathbf{A}^{-1}$. This cannot be done because the matrix is often not square and it is computationally arduous to find. One way to overcome the problem is the implementation of an iterative algorithm. The generic procedure is [22]:

1. determination of an initial arbitrary image with same size of the image to be reconstructed. At the begin of the routine, the image is generally set to 0 for every pixel, so $f = (0, 0 \ldots 0)$;

2. calculation of the new projections;

3. determination of the difference between the projections of the last (n-th) estimation and the projections of the previous $(n-1)$ estimation. The vector f is updated with these results;

4. iteration from step 2 until the convergence criteria previously set is obtained.

The basic sequential ART algorithm [27] can be expressed in the form:

$$f^{k+1} = f^k + (a_i)^T \cdot \frac{(p_i - a_i^T f^k)}{a_i^T a_i} \tag{1.21}$$

with j being the index of the j-th column of the matrix $\mathbf{A}$. In this case, the algorithm considers the interceptions between one single ray and the pixels and then updates the value in order to find an equivalence between the ray sum and the projections. Despite being very fast, this algorithm also generates artifacts, since every pixel in the image is intercepted by more than one ray. This brought to the elaborations of further algorithms, such as the simultaneous iterative reconstruction technique (SIRT) or the simultaneous algebraic reconstruction technique (SART) where each pixel value is updated only when all the equations related to every ray have been considered [28].

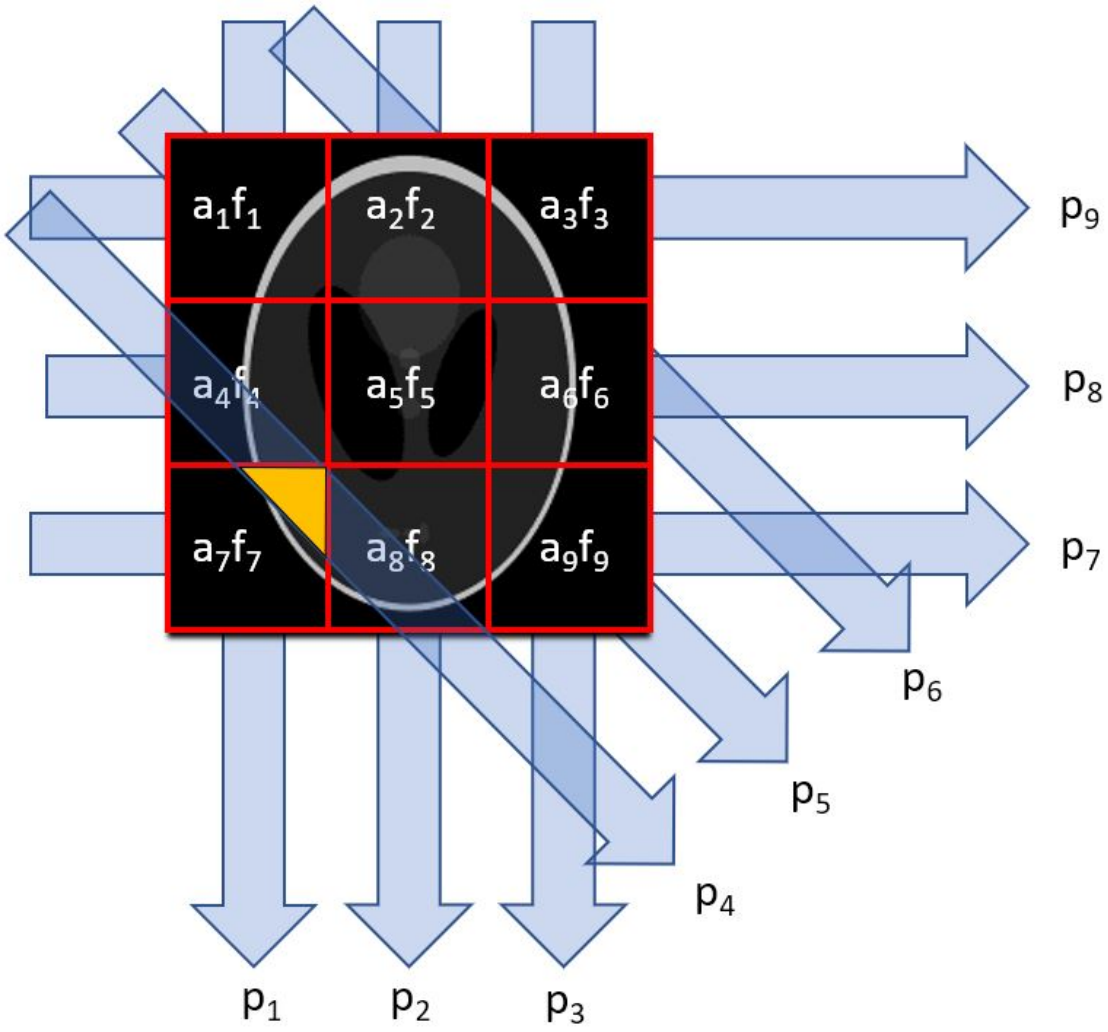

Figure 1.10: Sketch of the discretization operated by the algebraic reconstruction algorithm on a sample image. The image is subdivided in pixels, each pixel expresses a value (f) which is related to the attenuation coefficient of the sample material. The blue arrows represent the neutron rays going through the sample. They can perfectly fit the pixel row (for instance in case of projection p_9) or they can cross adjacent pixels (as marked in yellow in projection p_4). The weighting factors a_{ij} take into account such cases.

2 | IMAT neutron imaging facility

2.1 Beamline design

The IMAT neutron imaging facility is located at the ISIS neutron spallation source, which is a part of the Rutherford Appleton Laboratory (RAL), located in the South Oxfordshire, UK.
The neutron beam is generated 10 times per second by a spallation process of 800 MeV protons directed towards a tungsten target. After the reaction, the neutrons are slowed down by a 18 K hydrogen moderator to make them usable for imaging experiments, providing a cold-thermal spectra of neutron with wavelength in the range of 0.68 - 6.8 Å. Such spectrum is defined by means of a couple of mechanical disk choppers made of an aluminium alloy and covered by a 10 mm layer of B_4C. They are positioned at 12 m and 20 m from the moderator, while a third chopper is located at 12.8 m from the moderator and serves as fast neutrons and gamma filter.
The neutron beam is then transported to the entrance of the IMAT instrument with a supermirror neutron guide with a multilayer reflective coating whose m-parameter is equal to 3. Such parameter determine the maximum critical angle at which the neutron can enter the guide without being loss. The higher the m-parameter, the higher the maximum critical angle, but as a drawback the loss along the path become more important.
In order to collimate and shape the beam, five sets of mechanical jaws made of 10 mm thick B_4C blades are integrated in the flight path.
At the end of the guide the pinhole selector is located. There are five different pinholes with aperture diameter in the range between 5 and 80 mm, corresponding to L/D ratio between 2000 and 125.
Finally, at a distance of 56 meters from the source, an heavy-duty 7-axis Sample Positioning System (SPS) is located in the central part of the experimental area. The rotational stage permit the acquisition of radiographies at different angles, thus enabling the possibility to make a tomographic reconstruction of the specimen. In front of the sample positioner, the detector camera is held by a 7-axis robotic camera positioning system. Either the CMOS camera or the MCP detector can be connected here. In the left part of the blockhouse, two 90 deg diffraction banks prototypes with 200-element neutron scintillators are located.

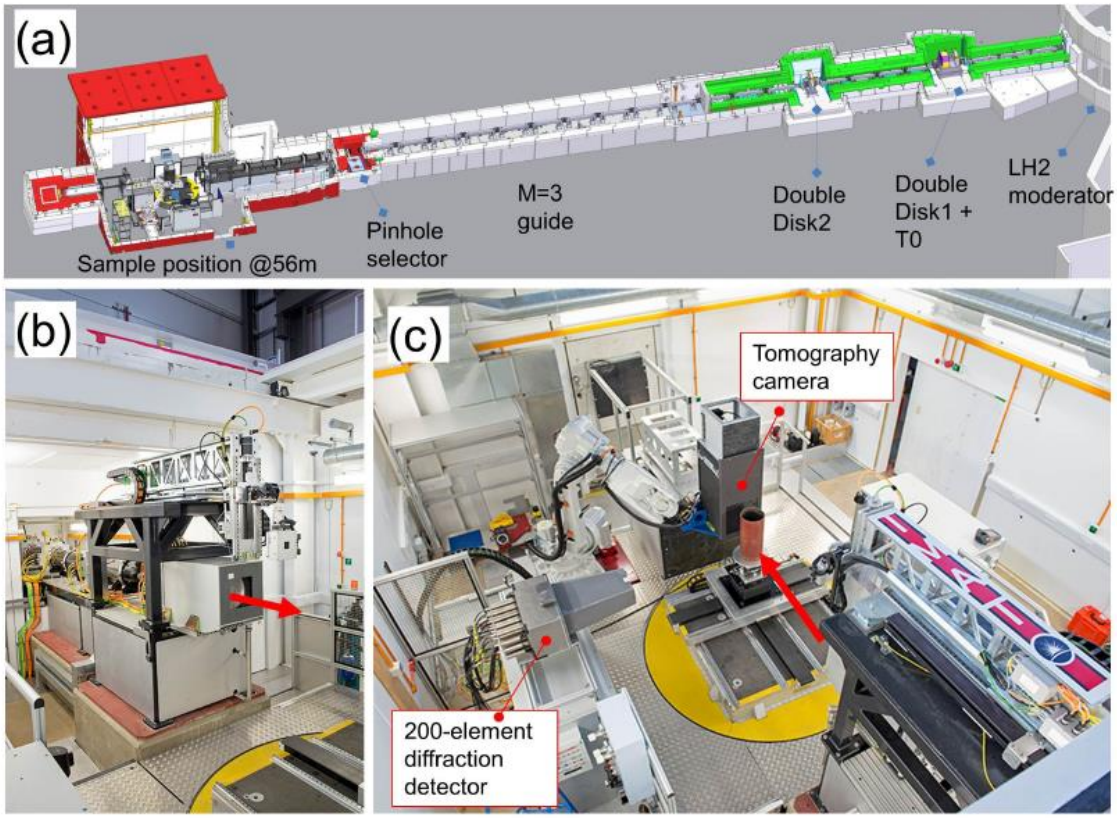

Figure 2.1: *a)* Sketch of the IMAT beamline from the spallation source to the experimental area. *b)* Termination of the neutron guide: the red arrow shows the direction where the neutrons go after leaving the guide. *c)* Top view of the experimental hall: the diffraction detector (bottom left) is visible, as well as the robotic positiong arm (central left). The tomography camera (central upper) where either the CMOS detector or the MCP detector can be positioned to acquire images at different angles. This is possible thanks to the rotation stage placed in the centre of the room. [29]

2.2 Detectors

Two detectors are now implemented in the IMAT instrument. Each one with its own peculiarities.

2.2.1 Microchannel Plate (MCP) neutron detector

The MCP neutron counting detector is a combination of a solid neutron converter with a electronic readout. The layout of the solid converter is the result of the evolution of the conventional photomultiplier tubes invented in the early 1930s [30], which were not usable in difficult environments, such as in space applications. The overall layout of the MCP device is a glass disk with a diameter of tens of mm

and thickness of $\sim$ 1 mm, with pores (the channels) of $\sim$ 10 µm in diameter. The main idea relies on the fact that when electrons are expulsed from their atoms in the glass bulk, due to an external impinging radiation, they bump on the channels internal walls, causing the expulsion of secondary electrons. These are accelerated by the voltage applied all over the channels (usually $\sim$ 2 kV) and create an internal electron avalanche. There is also the possibility to assemble a stack of MCPs in order to reduce the ion-feedback effect and to improve the measurement [31].
The traditional MCP is an assemble of thousands of fibers with a borosilicate layer and a proprietary etchable glass core. These fibers are drawn and fuse together to form a unique billet, which is later sliced and polished to obtain single MCP wafers. These are later chemically processed in a bath of acid which is able to etch out the fibers cores only, leaving the cladding material intact. In this way the empty channels are made. The final part of the process is the formation of the electric contacts through metal evaporation [32]. Recently, new methods have been developed for the fabrication, including micromachining techniques on silicon, largely performed in the microelectronics industry and then well established and reliable [33]. The advantages are numerous, from the full integration directly into ASICs chips to the full customization of their shape and length.
The potentialities of such device can be extended to the world of the neutrons by including an element with high absorption cross-section into the bulk structure, as firstly introduced by [34]. Currently, the most common dopant is the boron with its enriched ^{10}B isotope, which shows to thermal neutrons a cross section of 3800 barns, through which the neutron-induced nuclear reaction ^{10}B(n,α)^{7}Li brings to the formation of α-particles and ^{7}Li nuclei. Such reaction can have two outcomes: it can brings, in 94% of the cases, to the formation of an excited ^{7}Li* nucleus, which shortly decades to its stable form, having a kinetic energy of 838 keV and releasing a γ-radiation of 478 keV, or in the remaining 6% of the cases, to the emission of a α-particle at 1777 keV and a ^{7}Li nucleus at 1014 keV. These particles are emitted in opposite directions, after the nuclear reaction, and struck the inside walls of the channels, thus triggering the electron avalanche (Fig.2.2). Once generated, the output charge cloud must be collected by a readout. The electronic chip implemented in the MCP neutron counting detector camera used at IMAT is based on the Timepix detector [36].
The Timepix is an ASIC chip developed at CERN, with a matrix of 256 $\times$ 256 pixels, each one with a size of 55 µm, and a total active area of 14 $\times$ 14 mm^2. Being the area of a single Timepix chip very small, the readout implemented at IMAT was chosen to be an evolution of the Timepix. It is the quad Timepix, developed by Tremsin et al. [37], that is a set of 2 $\times$ 2 single Timepix chips forming a bigger sensitive matrix with a size of 28 $\times$ 28 mm^2, and with a new parallel electronic readout. By means of this setup, the acquisition of all the events registered in the 14 bit shift register of each pixel, in one time frame (the acquisition time set by the user), takes $\sim$ 320 µs, during which an electronic shutter is raised, preventing the recording of further events. A maximum amount of 1200 frames per second can be acquired.

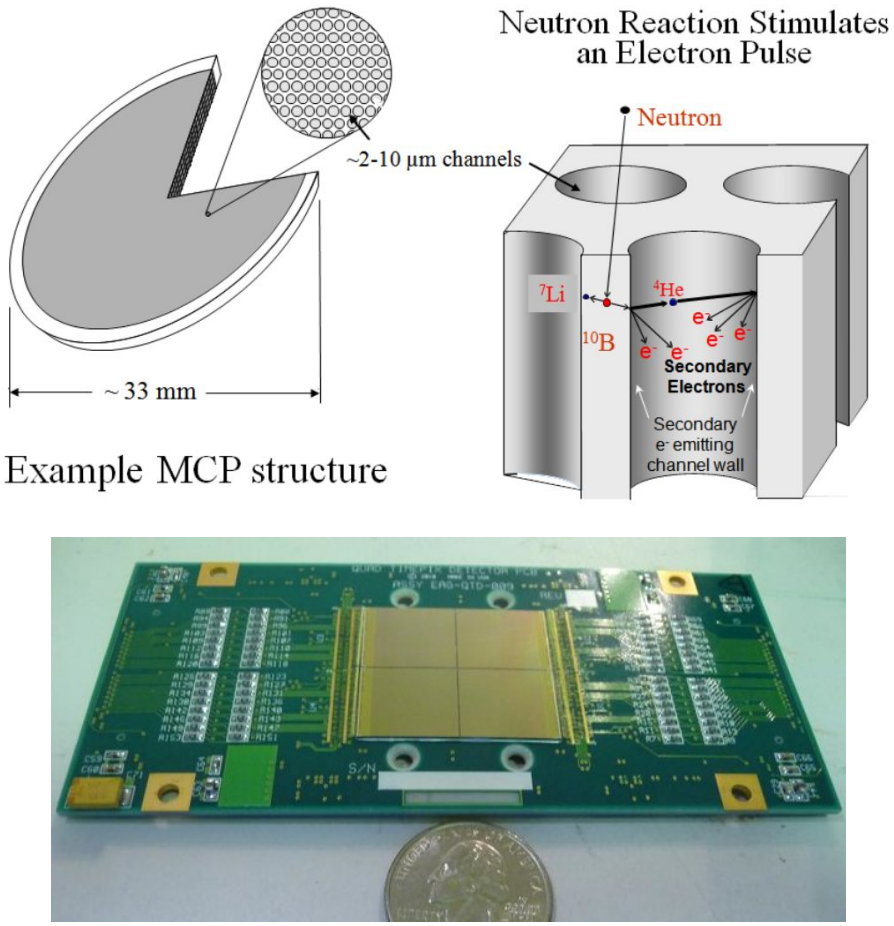

Figure 2.2: Top: Sketch of the MCP device and schematic of induced nuclear reaction. Courtesy of *NOVA Scientific, Inc.* Bottom: quad Timepix electronic readout [35].

The quad Timepix obviously inherits all the peculiarities of the Timepix chip, including the three different modes of operation:

1. *event counting mode*: the chip counts the number of events above a set threshold. Up to 11000 events can be registered by each pixel in a single time frame;
2. *time over threshold mode (ToT)*: the chip records the time in which the collected charge is over a threshold, with a time resolution defined by a reference clock up to 10 ns and a timing range of 11000 time bins;
3. *time of arrival mode (ToA)*: the chip records the time of the event arrival, with same ToT timing features.

The third mode is extremely useful, since the time resolving capability enables the possibility to conduct studies on a wide range of applications, including stress and phase mapping via Bragg Edge analysis, when a pulsed neutron source is used for the experiment.

2.2.2 CMOS camera detector

The CMOS camera is the neutron detector developed at the italian CNR laboratories [38] with the largest field of view (FOV) at the IMAT instrument, allowing acquisitions up to 211 × 211 mm^2. The CMOS chip integrated in such a detector is the "Zyla 4.2 sCMOS" produced by ANDOR, which is 13.3 × 13.3 mm^2 large, with a matrix of 2048 × 2048 pixels of 6.5 µm in size. The sensor is Peltier-cooled to reduce the dark current down to 0 °C. The converters in this case are ^{6}LiF/ZnS based neutron screen scintillators with a thickness in the range of 50 - 450 µm. They convert the incoming neutrons in visible light in the 450 - 520 nm range, which is reflected by an internal mirror at 45° and directed towards the optical lens. The latter can be changed depending on the resolution and contrast needed for the analysis, as well as the focal length, which can selected in a range from 50 mm to 135 mm with f-number from 1.2 to 2.0. The autofocus system is based on the projection of a matrix of 13 × 13 dots by a 3 mW laser diode at 635 nm onto the scintillator plane. A contrast-based algorithm analyses such dots in both horizontal and vertical direction and find the optimum, that is the best distance between the scintillator and the optical lens, the latter moved by a motorized linear stage, at which the degree of spreading of the dots is minimum. The whole system is inserted in a black anodized aluminium box, to prevent noise coming from external light sources.

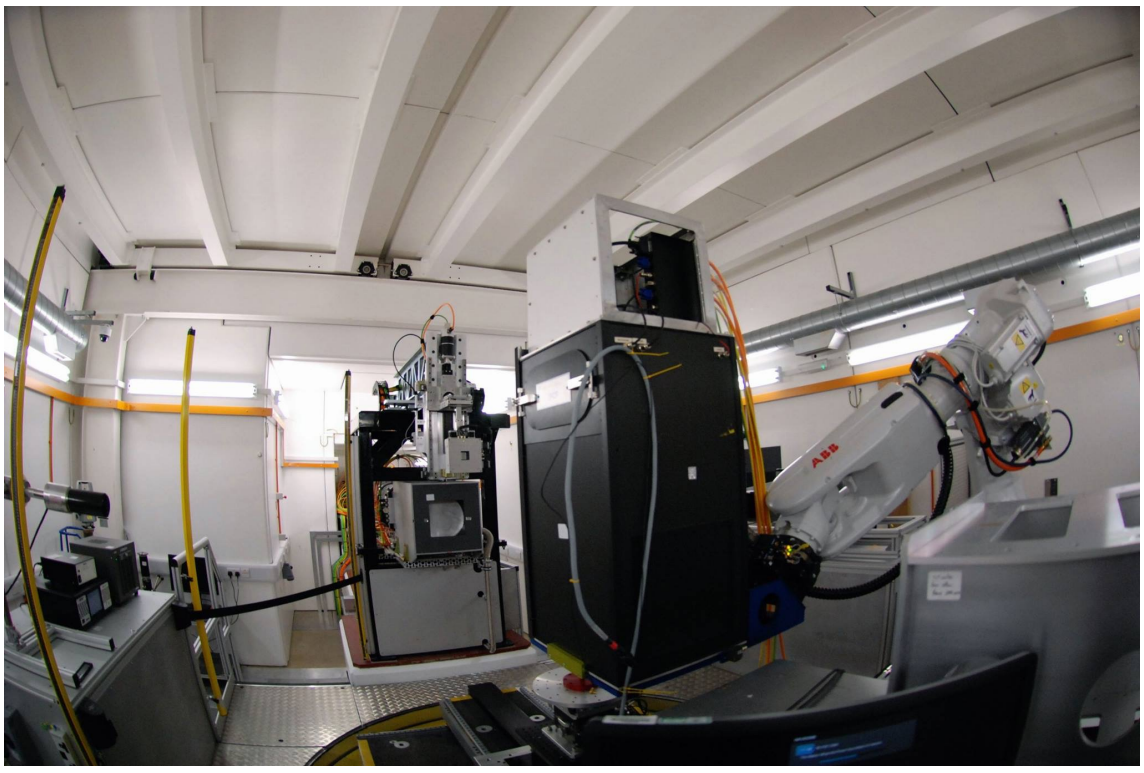

Figure 2.3: Detail of the CMOS camera hold by the robotic arm. The exit of the neutron guide is visible in the back.

3 Applications of transmission neutron imaging

3.1 Energy resolved analysis

One of the main peculiarities of the IMAT facility is the possibility to conduct studies on samples in energy-resolved mode.
In fact, on a pulsed source, energy-resolved imaging is enabled by a time of flight (TOF) analysis of the neutrons transmitted or scattered by the sample. This mode requires synchronization of the beamline components with respect to the pulse generation, thus including choppers, monitors and cameras. The correct timing is guaranteed by an external trigger signal which is provided by the source, marking the generation of neutrons in the target. For each pixel of a neutron camera, the time of the neutron arrival related to this trigger is measured. The wavelengths of the detected neutrons are then calculated from their time of flight by the following equation:

$$\lambda = \frac{h(T + \Delta T_0)}{mL} = 3957 \times \frac{(T + \Delta T_0)}{L} \tag{3.1}$$

where λ is the neutron wavelength (in Ångstrom), h the Planck's constant, T the neutron time of flight (in seconds), ΔT_0 is the time offset of the source trigger received by the data processing electronics (in seconds), m is the neutron mass, and L is the flight path from source to camera (in meters).
Such technique can be thoroughly exploited to study the crystalline state of the specimen under investigation. Polycrystalline materials are constituted by a large number of tiny crystals, whose atoms are arranged in an ordered and periodical lattice. The latter is characterized by a primitive cell, which can assumes several shapes, like a cube (the simplest one, formed by eight atoms), an hexagon, a parallelogram and so on. Such cells are periodically repeated to form the whole atomic lattice. The orientation of the planes formed by this arrangement is indicated by means of the *Miller* indices: these are integer numbers representing the reciprocal of the intercept of the plane along the crystallographic axes [39]. They are usually labelled in the following ways, depending on which property one wants to specify:

- (h,k,l): this represents a single plane in the atomic lattice;
- {h,k,l}: this represents a family of planes, i.e. all the planes which are equiva-

lent to the one specified by the Miller because of the symmetry of the lattice;

- [h,k,l]: this represents a direction defined by the vectors associated to the Miller indices;
- <h,k,l>: this represents the set of all the directions equivalent to [h,k,l] by symmetry.

These concepts come useful when dealing with energy-resolved transmission pattern analysis, that takes fully advantage of the wide neutron energy spectrum available at IMAT. Such technique relies on the Bragg equation, which describes the way in which radiations impinging on a periodical atomic lattice are diffracted. This equation is still valid for the neutrons, since they can be seen as waves with a wavelength λ, as already stated by De Broglie in Eq.1.2:

$$n\lambda = 2 \cdot d_{hkl} \cdot sin\theta_{hkl} \tag{3.2}$$

where n is an integer representing the order of diffraction, λ is the wavelength of the impinging neutrons, d_{hkl} is the distance between the (hkl) lattice planes, θ_{hkl} is the diffraction angle between the impinging neutrons and the (hkl) planes.
According to such equation, as long as the incoming radiation wavelength λ is less than $2d_{hkl}sin\theta$, the diffraction takes place at the angle fulfilling such relation. In the particular case where $\lambda = 2d_{hkl} \cdot sin\,90° = 2d_{hkl}$, there is backscattering of the neutrons, which are diffracted in the opposite direction from where they were coming. If λ has a value greater than that, no scattering takes place. The transmission then abruptly increases because the neutrons can now pass towards the atomic lattice producing a *Bragg edge* in the transmitted intensity as a function of the wavelength. The advantages of such a technique are many: it is possible, for instance, to individuate the residual stress causing a deformation in the atomic lattice of the sample. Furthermore, one can recognize different materials inside one specimen, since the crystallographic structure changes according to the kind of elements constituting it. Finally, crystallographic phases of the same material can be distinguished as well, making possible the individuation of different polimorphs in the same specimen. This property can be exploited in the analysis of biological samples, since their formation is often subject to a plethora of different ambient conditions, ranging from high pressure due to stratification of rock layers to changes in temperature.

In particular, the analysis performed at IMAT through Bragg edge transmission imaging focused on a so-called soufflè pearl. This is a kind of cultured pearl where an hydrophilic bead is injected in the pearl nucleus and put into water, where it starts to expand. At the end of the whole process, when the pearl nacre is formed, the bead degrades leaving an empty space in the inner part. According to the literature, the main material of the pearl bulk is the calcium carbonate, present in two phases, calcite and aragonite, the second organized in a typical "tablets" microstructure. This property was confirmed in a non-destructive way by making a comparison between the spectrum of the aragonite related to its crystallographic d-spacing and transmission spectrum acquired in the experiment. The latter can be analysed and

Figure 3.1: Cultured soufflè pearl.

plotted with the public domain Java image processing program called ImageJ [40]. A clear advantage of this software is the possibility to easily integrate plugins developed by users according to their needs. In fact, a plugin was created for IMAT users to accelerate the creation of transmission images trough the normalization of the sample radiographies with respect to the open beam.
Furthermore, the plugin permits the correction of the transmission spectrum affected by the problem of the "overlap effect" [41], when the MCP detector camera is used (Fig. 3.2). This problem comes from a limitation of the Timepix readout, since the 14 bit register associated to each pixel in the matrix can store only one event per time frame. This means that, until all the data are transfered to the memory and a new time frame is initialized, not more then a single event is registered per pixel, so a loss of information happens. This problem can be overcome in data post-processing when the neutron flux has a periodic structure. The solution proposed by [41] relies on the calculation of the probability $P(t_i)$ that a pixel at the time bin t_i has already registered an event and therefore cannot reveal anything more until the next time frame of acquisition starts. In fact, considering that the neutron pulse repetition rate at IMAT is 10 Hz, all the equal pulses can be acquired in m time frames, where the duration of a single time frame is not greater than the duration of a whole neutron pulse , one can write:

$$P_{occ}(t_i) = \frac{\sum_{j=0}^{i} N(t_j)}{S^m} \tag{3.3}$$

where $N(t_j)$ is the number of events detected at the j-th time bin and S^m is the repetitions number of the m-th time frame (or simply the total number of neutron pulses). Knowing the probability of occupation, one can calculate the number of events in an alternative way:

$$N(t_i) = N'(t_i) \cdot P_{free}(t_i) = N'(t_i) \cdot (1 - P_{occ}(t_i)) \tag{3.4}$$

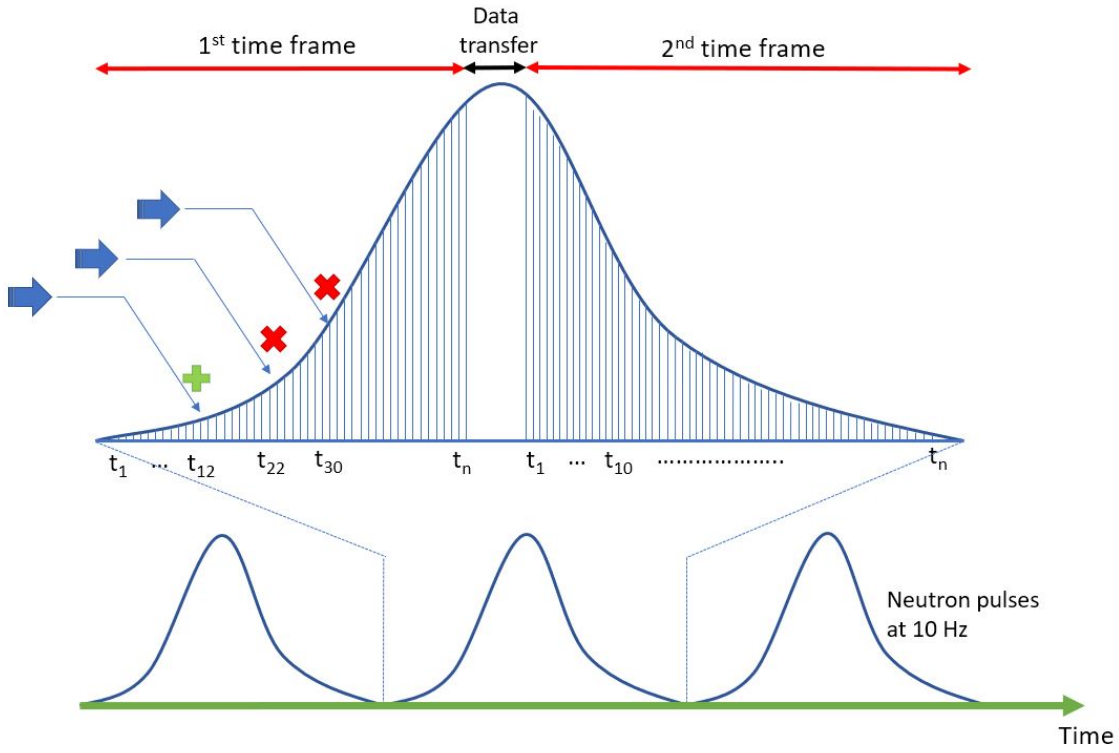

Figure 3.2: Sketch of an event acquisition for every pixel in the Timepix readout. In the example, the neutron pulse is acquired in two distinct time frames. In each frame, there are n time bins. In the first frame, an event occurs at t_{12}. This event is saved in the pixel 14 bit register. Later, further events happens at t_{22} and t_{30}, but they are not recorded, because of the overlap issue. The pixel register will be locked until the data transfer will take place. After this point, the pixel register will be clean and ready to acquire again.

which means that the number of events counted in one pixel at the i-th time bin is equal to the number of all the events $N'(t_i)$ times the probability that the pixel is free. $N'(t_i)$ is the value we need, because it represents the real neutron count without overlap. Rewriting the equation:

$$N'(t_i) = \frac{N(t_i)}{1 - P_{occ}(t_i)} = f \cdot N(t_i) \tag{3.5}$$

with f being the overlap correction factor. The improvement brought by this algorithm are clearly noticeable. In fact, the corrections were applied to the transmission spectrum extracted during the analysis of the soufflè pearl (Fig. 3.3).
Despite the fact that applying this correction is relatively easy, the time needed can grow noticeably when a large collection of data needs to be fixed. Therefore, this issue will be definitely resolved via hardware with the implementation of the new version of the Timepix, the Timepix3. This chip will include a sparcified readout to eliminate the dead time problem and overcome the overlap effect [42].

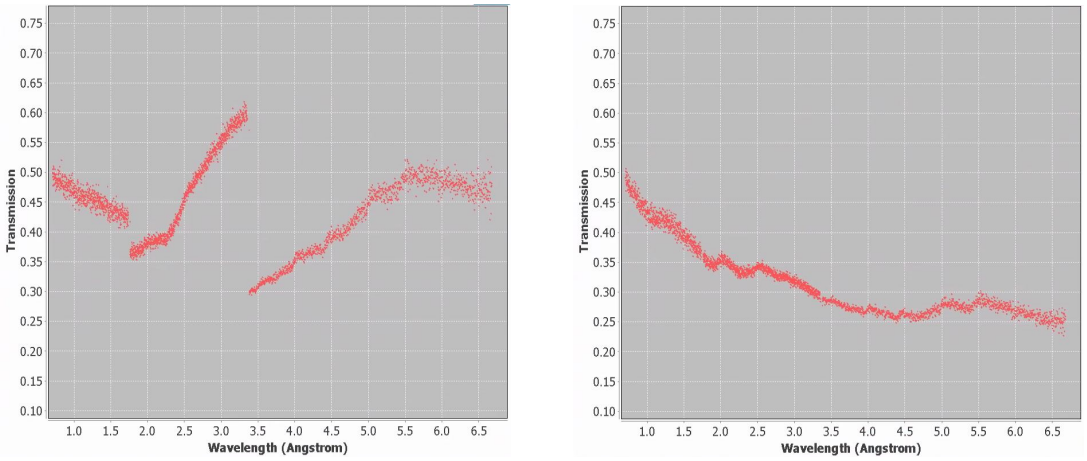

Figure 3.3: Bragg edge transmission spectrum of the pearl nacre before (left) and after (right) overlap correction.

Miller index	d-value [Å]	Intensity [a.u.]
201	2.7004	1000
210	2.4845	503.5
122	1.9769	459.7
121	2.1894	294.0
211	2.3718	268.2

Table 3.1: Table of Bragg edge intensities related to the main crystalline orientations of the aragonite.

Once the overlap correction was applied, the presence of the aragonite phase was revealed by considering the transmittance variation of the neutrons in the sample with respect to different wavelengths (Fig.3.4). The positions of the Bragg edges were compared with the ones tabulated in Tab.3.1 and the (201) plane orientation resulted to be the most present. Moreover, a novel software tool developed by Minniti [43] was able to elaborate a two-dimensional colored map of the distribution of the main crystalline orientation of the aragonite all over the specimen.
Finally, the stack of 450 projections collected within the [0° - 180°] angular range with steps of 0.4° permitted the tomographic reconstruction of the sample by means of the Simultaneous Iterative Reconstruction Technique, with a resolution of 60 µm (Fig.3.5). The peculiarities of the nacre are visible, from the morphological and compositional point of view. Firstly, one may appreciate the inner bilobated nature of the pearl due to its particular culture technique; secondly the study of the gray map indicates specific characteristic of the biomineralic sample: for instance the white parts indicate a high interaction of the pearl with the neutron beam, showing the presence of organic compounds.
Such experimental results, described with more details in *PAPER II*, demonstrated the efficiency of the neutron Bragg-edge imaging, showing that the field of the cul-

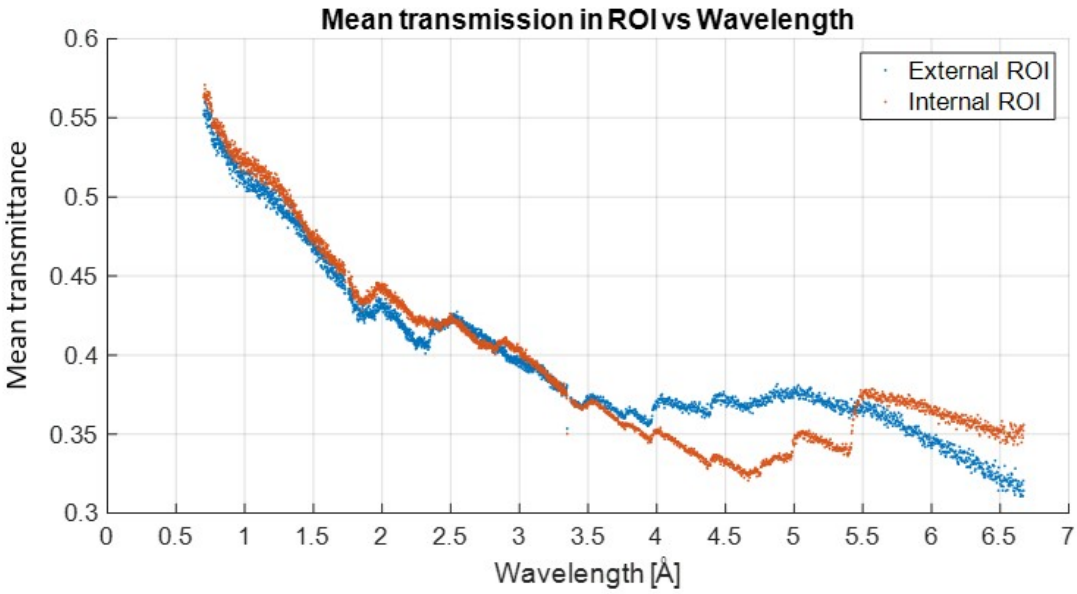

Figure 3.4: Pearl transmittance vs neutron wavelength of its shell (blue) and core (orange). The Bragg edges related to the aragonite presence in the sample are visible. Figure from *PAPER II*.

tural heritage science may largely benefits from this non-destructive energy resolved imaging technique.

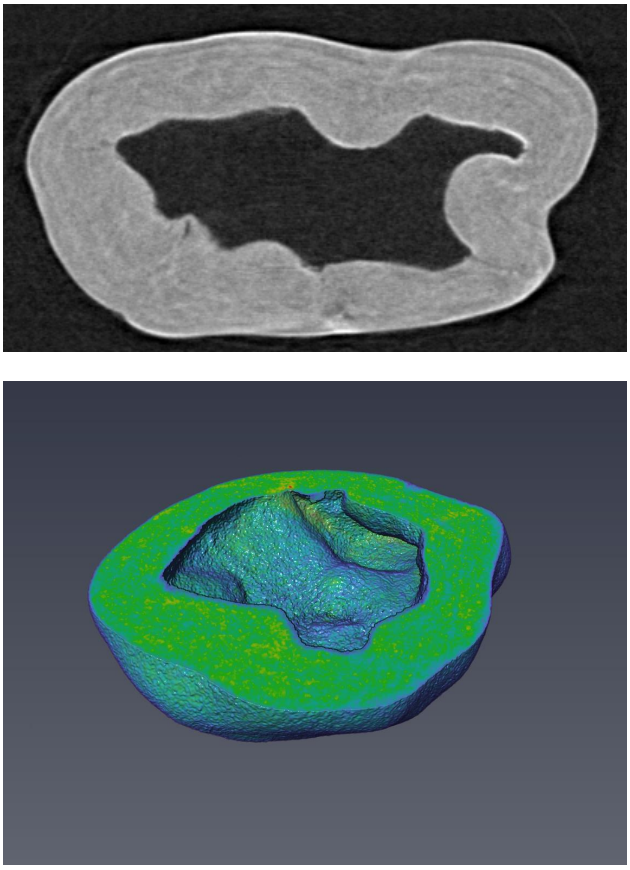

Figure 3.5: Top: virtual slice reconstruction of the central part of the pearl under analysis, obtained with SIRT technique. Bottom: three-dimensional reconstruction of the whole pearl volume by stacking the virtual sections with a cut in the central part, to emphasize the inner morphology of the specimen.

3.2 Multiple radiography analysis

Despite the advantages offered by the neutron transmission analysis, in terms of sensitivity to hydrogen-based compounds or heavy elements to name a few, there are still limitations for what concerns the maximum image resolution available in the sample analysis. While such a demand of high precision images in the last years pushed the maximum resolution up to $\sim$ 5 µm [44], the target of 1 µm and below, which is already feasible in the X-ray imaging [45], is still out of reach.
By contrast, a different approach can be used to get information at micrometer level from the sample under analysis, by interpolating the data extracted by images acquired at different angles. This method has been implemented for the non-destructive diagnosis of a new neutron detector: the BAND-GEM (Boron Array Neutron Detector with Gas Electron Multiplier).
This is a new detector based on two principal components: a three-dimensional neutron converter, consisting of a stack of aluminium grids covered with 1 µm thick layer of $^{10}B_4C$ and immersed in a argon-carbon dioxide gas mixture, and by a triple GEM [46], used for charge signal amplification. The conversion exploits the following reaction:

$$n^0 + {}^{10}B \rightarrow {}^{7}Li + {}^{4}He \tag{3.6}$$

where the alpha particles and the lithium particles ionize the gas mixture, creating a cloud of free electrons which are drained towards the gas multiplier by the applied voltage between the anode and the cathode and finally transformed into an electric signal (Fig.3.6). The $^{10}B_4C$ layer thickness has a fundamental importance in this case, since it determines the actual amount of total interactions of the neutrons passing through the lamellae. It must not vary along the grids, because such a difference would bring to a position-dependent measurement of the neutron flux impinging the detector. Therefore, every grid must be checked to be sure that the boron distribution is uniform and close to the theoretical parameter decided in the design phase.

The multiple radiography approach relies on the basic relation between the thickness of the boron converter and the angle of the impinging beam. In fact, in terms of transmitted neutrons and macroscopic cross section, the following equation holds:

$$I = I_0 \cdot e^{-\Sigma \cdot t_{eff}} \Rightarrow -\frac{ln\frac{I}{I_0}}{\Sigma} = t_{eff} = t_{real} \cdot \frac{1}{cos\theta} \tag{3.7}$$

with I the transmitted neutrons, I_0 the incoming neutrons, Σ the macroscopic cross section, t_{eff} the effective thickness and t_{real} the real thickness, as represented in Fig.3.7.
Being the grids of a size in the range of tens of centimeters, the experiment carried out at IMAT involved the use of the CMOS camera coupled with a neutron sensitive scintillator screen, whose field of view was of 211 x 211 mm^2. The focal length of the optical lens was of 50 mm, giving a final resolution of 103 µm. The radiography generated by its electronic readout is characterized by a gray scale level of 16 bit

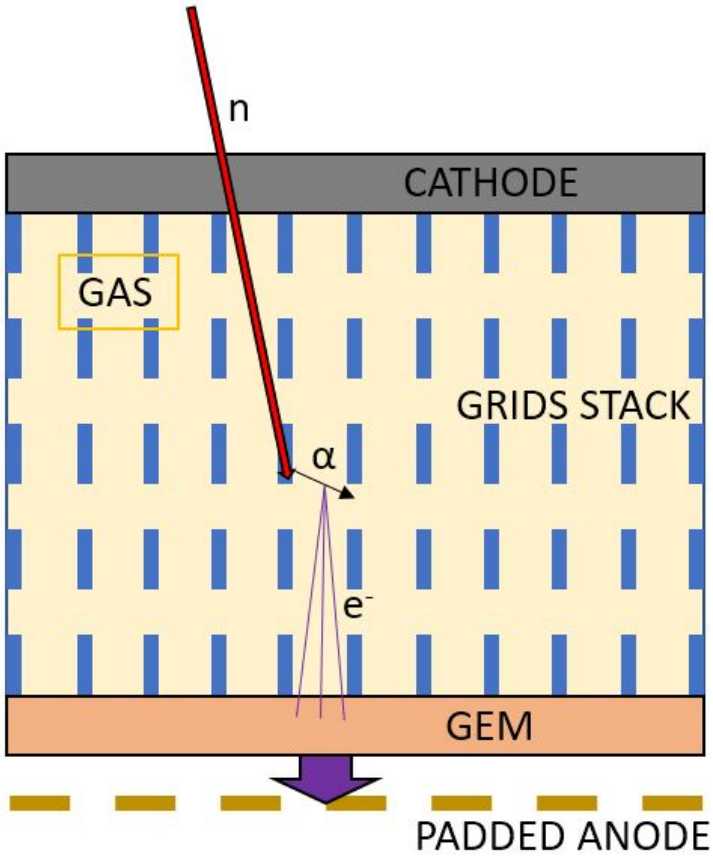

Figure 3.6: Sideview of the BAND-GEM detector. The blue lines in each row represent the lamellae forming one single grid. Several grids are stacked one over the other, thus covering a cubic volume. The incoming neutrons (red arrow) are converted by the boron layer covering the lamellae, generating alpha and lithium particles. Such particles ionize the surrounding volume of gas (light yellow), creating free electrons (purple lines) which are drained towards the GEM (orange) and amplified before reaching the electronic readout (dark yellow).

per pixel, which gives an evaluation of the neutron flux I hitting the area covered by each pixel. The darker the radiography, the higher the absorbance, the thicker the layer. In this way, by calculating the gray level average of a small area covering one segment of a lamella and by repeating this calculation for all the angles, it is possible to make a linear interpolation of the effective thickness and to extract the real thickness value from the slope of the line.
In order to get the t_{eff} value, according to Eq.3.7, two quantities must be computed. The ratio between the neutron flux before and after the sample is given by the normalization of the radiography with respect to the open beam, which is acquired by the detector camera when no sample is present. Also, the signal generated by the dark current of the detector camera must be taken into consideration and subtracted from both the sample image and the open beam image, so that the final transmission

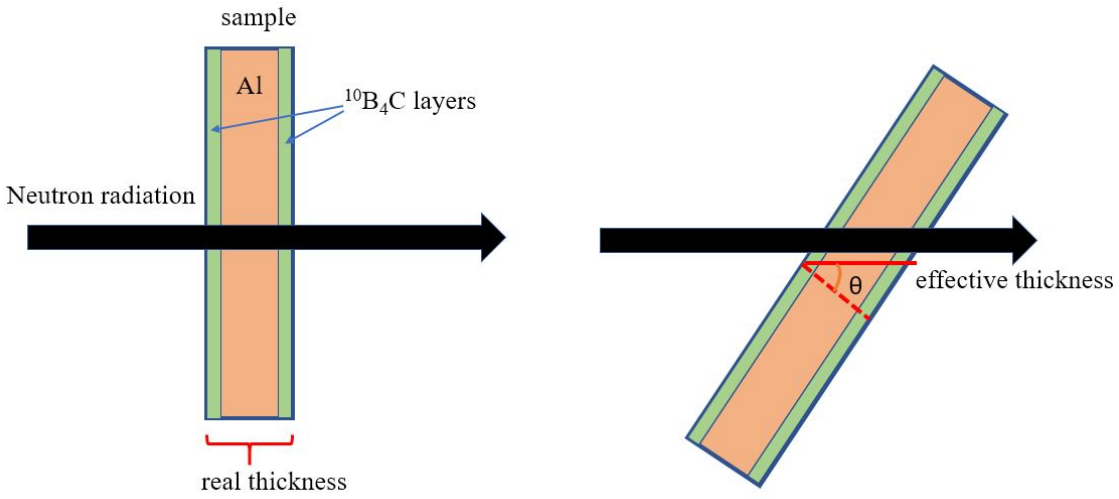

Figure 3.7: Sketch of one of the several lamellae forming a single grid. The real thickness of the layers is detected when the lamella is perpendicular to the neutron beam. By tilting the lamella, the neutron goes through an apparent thicker layer, whose thickness is proportional to the cosine of the tilting angle. Figure taken from *PAPER III*.

image is given by:

$$T = \frac{I - I_{dark}}{I_{OB} - I_{dark}} \tag{3.8}$$

The value of Σ, by contrast, must be calculated taking into account several aspects. The predominant element in the conversion process is the ^{10}B. Its microscopic cross section is tabulated and has been extracted from the NEA database [47]. It presents a strong dependence with respect to the energy of the impinging neutrons. Such aspect was considered during the analysis, since the contribution to the asborbance given by the ^{10}B macroscopic cross section was weighted with respect to the energy-dependent neutron flux in the IMAT beamline (Fig.3.9). At the same time, although much less significant, the weighted cross sections of the carbon and the aluminium were considered as well.

In order to build a map of the layer thickness over the grids, the algorithm subdivides each radiography into a matrix of sectors, each one containing 5×40 pixels (1×8 mm in the real space) thus covering a fraction of a single lamella, to have a sufficient statistics for the thickness estimation. The enormous amount of radiographies to process and analyse forced the implementation of an automatic routine able to follow the shift of the lamellae due to the rotation of the grids (Fig.3.10) and to assign the right transmission value to the same sector at different angles.

At the end, a three-dimensional matrix is created by the analysis code, two dimensions locating the sector in the grid and the third storing the averaged gray value at every angle. After the fitting, a color map is displayed for a rapid view of the thickness distribution (Fig.3.11).

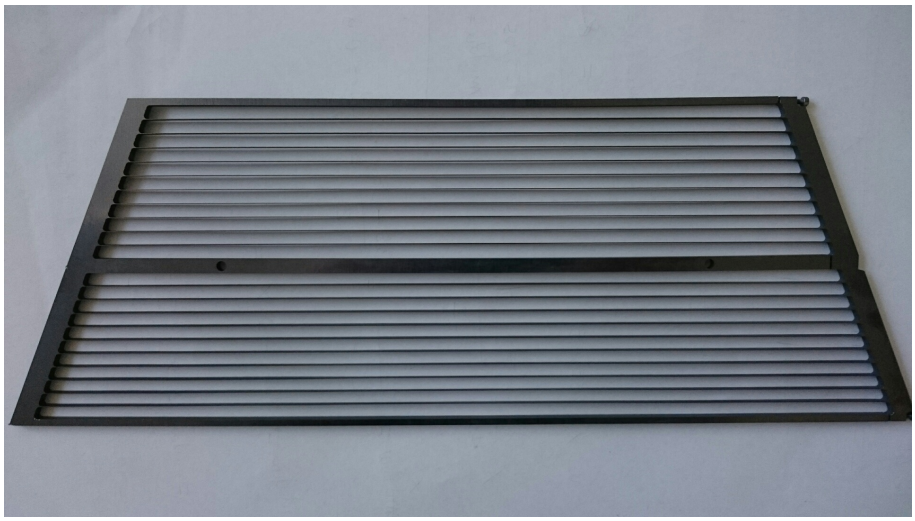

Figure 3.8: One aluminium grid. The 20 lamellae visible in the photo are covered on both sides with a 1 µm thick layer of $^{10}B_4C$.

The ^{10}B thickness distribution across the aluminium grid was compared with further analysis of the lamellae performed with the Scanning Electron Microscope (SEM). The analysis revealed an average boron thickness of 800 nm. Some lamellae located close to the edge of the grids were found to be prone to failure, revealing layers whose thickness was less than 500 nm. The SEM study resulted compatible with the outcome of this non-destructive analysis technique, considering the inner uncertainty brought by several elements: in fact, taking into account the uncertainty due to the precision of the angle of the rotation stage, the neutron flux measured at IMAT and the exact amount of the ^{10}B, carbon and aluminium over the lamellae, an overall uncertainty of 120 nm was estimated, which was still acceptable considering that thickness variations in this range would barely affect the overall detector efficiency.

This multiple radiography technique, as described in *PAPER III*, can be implemented in all the scientific cases where a non-destructive and extensive investigation of the thickness of neutron sensitive material is requested.

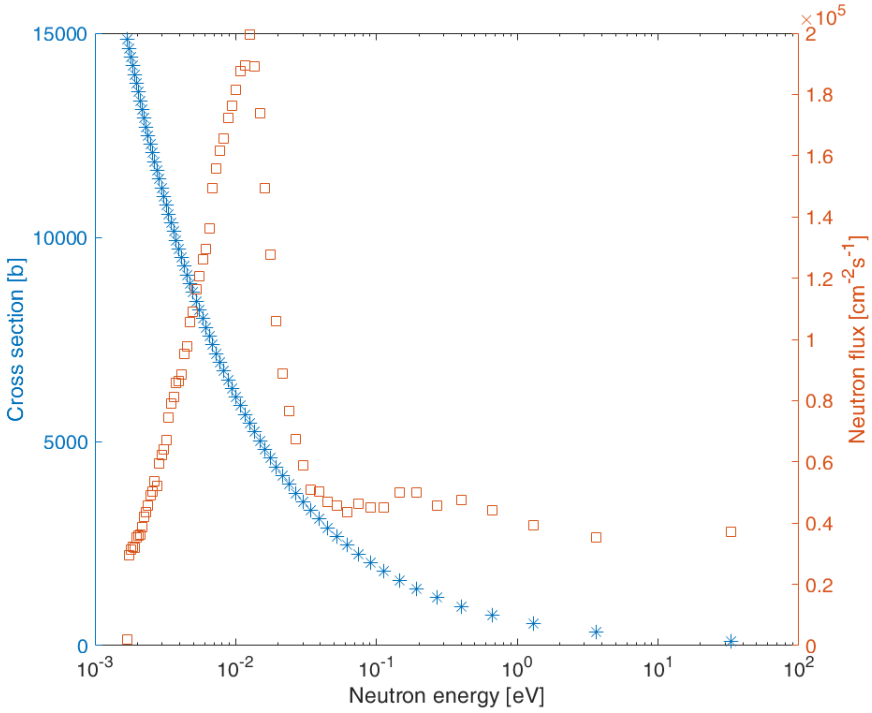

Figure 3.9: Microscopic cross section of the ^{10}B and IMAT neutron flux vs neutron energy.

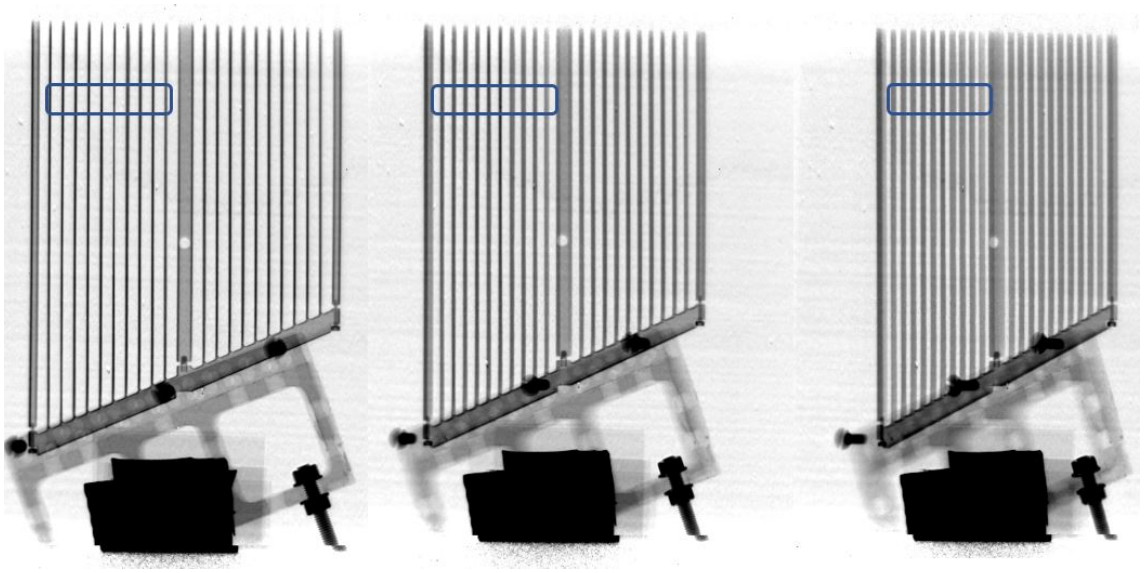

Figure 3.10: Example of one grid radiographed at three different angles. The perspective change influences the position of the lamella in the image and the spacing between them. A Fourier transform based routine included in the analysis algorithm is able to overcome this issue.

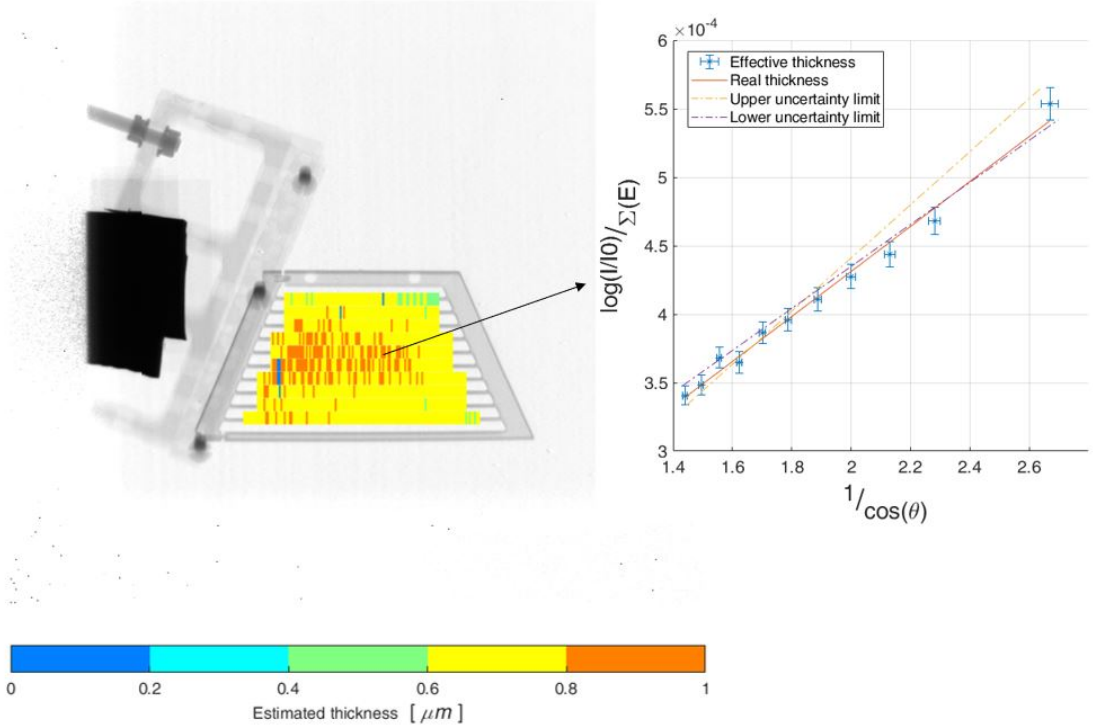

Figure 3.11: Thickness map of one grid. Each colored rectangle represents a sector. The color of the sector is determined by the slope extrapolated by the fitting of the values of the same sector at different angles.

4 | Improvements of imaging devices

4.1 Centroiding algorithm for TIMEPIX readout

In the field of imaging, the resolution plays a key role in the analysis of the experimental results. In the case of the MCP neutron detector camera, the resolution is limited by two main factors: the first is the diameter of the pores inside the borated MCP converter, which are currently limited at 4 - 10 µm; the second is the pixel size of the Timepix readout, which is of 55 µm. The latter, being the coarsest, defines the final resolution of the whole device.
Despite this, a higher resolution can still be obtained by means of an interpolation algorithm capable to reconstruct images from the event-mode collected datasets with a resolution up to $\sim$ 10 µm. Nonetheless, such a technique affects the maximum count rate of the detector, since the real-time data processing requires time to be performed, from $\sim$ 25 MHz to $\sim$ 3 MHz.
The algorithm used is based on a center of gravity centroiding routine, whose implementation can be done in several ways ([48, 49]) according to the needs in terms of elaboration speed and precision.
In the case of the MCP detector camera, some preparation must be done before starting the acquisition. The first step is the threshold equalization for each pixel in the matrix. Despite the fact that a global threshold can be set at once for the whole Timepix chip, small pixel-to-pixel variations are still present and must be checked and corrected with an automatized procedure, to achieve a totally flat and uniform response to the incoming radiations. The best threshold value must be choice with care, since setting a high value improves the signal to noise ratio (SNR), but at the expenses of some weak event which will not be detected at all.
A second step is focused on the equalization of the pre-amplifiers related to each pixel, since the signal amplification must be equal in every sector of the matrix as well. Even in this case, the right choice of the amplification parameter is crucial for the good outcome of the experiment.
The third step is related to the adjustment of the voltage in the space between the exit of the channels and the Timepix chip. Such voltage must be tuned in order to have a dispersion of the electron cloud generated by a single event over at least a cluster of 3 $\times$ 3 pixels, in order to be able to interpolate the charge values recorded in time over threshold mode (Fig.4.1). On the other hand, an extreme spreading of the electron cloud over multiple pixels can bring to an insufficient SNR and, as a

consequence, a blurring effect on the image.
Once the setup is completed, the detector can be used for the whole duration of the experiment with minimal or no adjustment. The core of the centroiding algo-

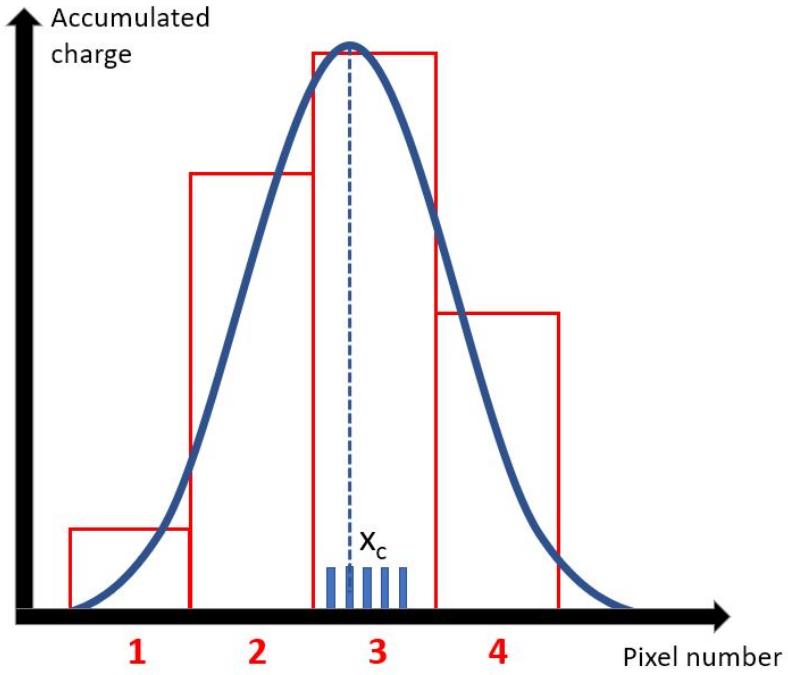

Figure 4.1: Sketch of the centroiding calculation, in one dimension. The electron cloud, here represented with a pseudo-gaussian distribution, created by one event is spread over four neighbour pixels, in different quantities. The algorithm individuates the centroid of the cluster and extimates its position, which, in this example, is located in some part inside the pixel number '3' (hence the definition of "sub-pixel resolution").

rithm implemented in the MCP detector camera relies on the individuation of the coordinates x_c and y_c of the event center of gravity [24], as described by Eq. 4.1:

$$\begin{aligned} x_c &= \left[i_c + F_x \cdot \left(\frac{\sum_{i=i_{c-}}^{i_{c+}} \sum_{j=j_{c-}}^{j_{c+}} (i - i_c)\, Q_{ij} \cdot G_{ij}}{\sum_{i=i_{c-}}^{i_{c+}} \cdot \sum_{j=j_{c-}}^{j_{c+}}} \right) \right] \cdot 55\,\mu m, \\ y_c &= \left[j_c + F_y \cdot \left(\frac{\sum_{j=j_{c-}}^{j_{c+}} \sum_{i=i_{c-}}^{i_{c+}} (j - j_c)\, Q_{ij} \cdot G_{ij}}{\sum_{j=j_{c-}}^{j_{c+}} \cdot \sum_{i=i_{c-}}^{i_{c+}}} \right) \right] \cdot 55\,\mu m \end{aligned} \tag{4.1}$$

where i_c and j_c are the coordinates of the pixel where the maximum charge value in the cluster created by the event is located. In this way each value is weighted by the distance $i - i_c$ from the event peak. Q_{ij} is the measured charge for every pixel, G_{ij} is the calibrated gain value, $i_{c\pm} = i_c \pm N_{pix}$ is the interval between the peak of the event and the half width of the charge cloud N_{pix} (analog to $j_{c\pm}$), $F_{x,y}$ is a correction function. These functions depend on he particular configuration of

the MCP detector camera, for what concerns the voltage applied to the MCPs and the threshold level on the Timepix. Also, there is a angular bias given by the tilt angle of the MCP with respect to the incoming neutron beam, which is in between 3 and 12 degrees. This permits to reduce the presence of fake signals due to the ions generated in the conversion process.
Once both the MCP detector and the sample were set for the measurement, the first attempt to reproduce a high resolution centroided radiography of a Siemens star was carried on at IMAT and published in *PAPER IV*. The results were analsyed with the calculation of the Modulation Transfer Function ([50]): while the standard radiography generated by the MCP detector camera shows a spatial frequency of 9 line pairs/mm at the 10% contrast cutoff, which, in terms of spatial resolution, is equivalent to the 55 µm of the pixels size in the electronic readout, the centroided image shows a higher spatial frequency of 28 line pairs/mm, which is equivalent to 18 µm (Fig.4.2). Such a results could be further improved by increasing the L/D ratio, thus reducing the blur due to optical reasons. An other issue is related to the long time of acquisition, since much more statistics must be collected by each pixel in order to calculate the center of gravity of the electron cloud generated by the neutrons. This problem is easily mitigated in facilities where the neutron flux is higher: for instance, the imaging facility at the future European Spallation Source will have, according to the preliminary simulations, a flux on the sample up to 30 times higher than IMAT [51].

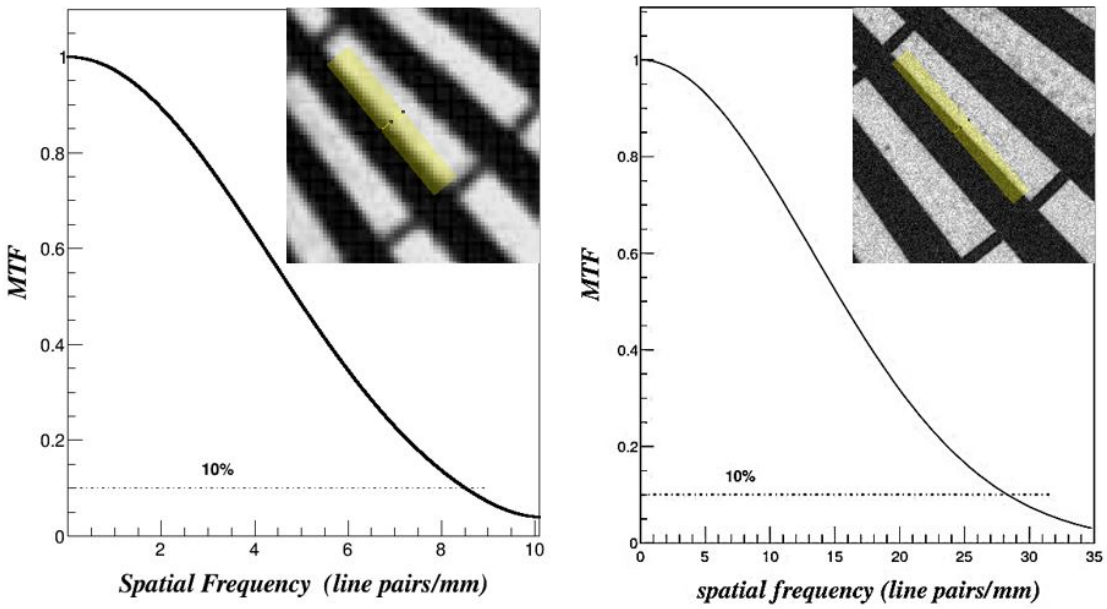

Figure 4.2: Modulation transfer function comparison between the standard radiography (left) and the high resolution centroided radiography (right) generated by the MCP detector camera.

4.2 Misalignment correction for TIMEPIX readout

4.2.1 Software design

The output of the quad Timepix readout is an image created by four Timepix devices arranged one next to the other to form a 2 × 2 sensitive detector. The clear advantage of such a setup is the increased field of view up to 28 × 28 mm^2, which extends the use scenarios of the neutron counting detector when the analysis of bigger samples is requested. By contrast, there are several drawbacks which affect the measurements as well. For instance, the increased sensitive area takes more time to be read, affecting the maximum frequency at which the detector can operate, even though such problem can be mitigated with the adoption of a parallel readout [35]. Another important issue comes from the way these pixel matrices are assembled together. In fact, the 2 × 2 chip configuration is problematic as each matrix of pixels should be ideally perfectly aligned to the neighbours to generate a perfect image. This was not possible so far, because of several constraints in the fabrication process and assembly. The result is that the images generated by the quad Timepix have systematic artifacts in the middle, where the gap between the chips is located. Since, as already discussed, such issue cannot be physically solved, a new method had to be implemented, thoroughly described in *PAPER V*.
This novel technique includes several steps. The initial one consists of finding a reference sample whose shape could be known with a precision higher than the uncertainty brought by the digital discretization of the pixels, which are, in the case of the TIMEPIX, 55 µm wide. The choice fell on a precision sphere, whose diameter was known with a precision higher than 1 µm. This geometrical shape is convenient for a fundamental reason: in fact there is an equation defining the degree of distortion of a circle (intended as the two-dimensional projection of the sphere onto a plane), known as *circularity factor*:

$$f_c = \frac{4 \cdot \pi \cdot A}{P^2} \tag{4.2}$$

with A being the area of the circle and P its perimeter. This value varies in the range between 0 (not a circle) and 1 (perfect circle) and is a powerful tool to understand the degree of deformation induced by the chip misalignment.
In fact, a set of transformations can be applied to each quarter of the image (created by each of the four chips) in order to obtain a circularity factor as close as possible to the value of 1. These operations include geometrical transformations on the vertical and horizontal axes and rotation clockwise and counter clockwise (Fig.4.3). Once found, this set of correction parameters is valid for every radiography recorded by that particular quad Timepix detector. Hence it can be used for other experiments, improving the precision of the analysis of single two-dimensional images and, in case of a tomography, the accuracy of a three-dimensional reconstruction of the sample.
The development of the algorithm to perform the full task was done with MATLAB by Mathworks [52], which provides a suite of comprehensive functions and classes needed for images elaboration [53].

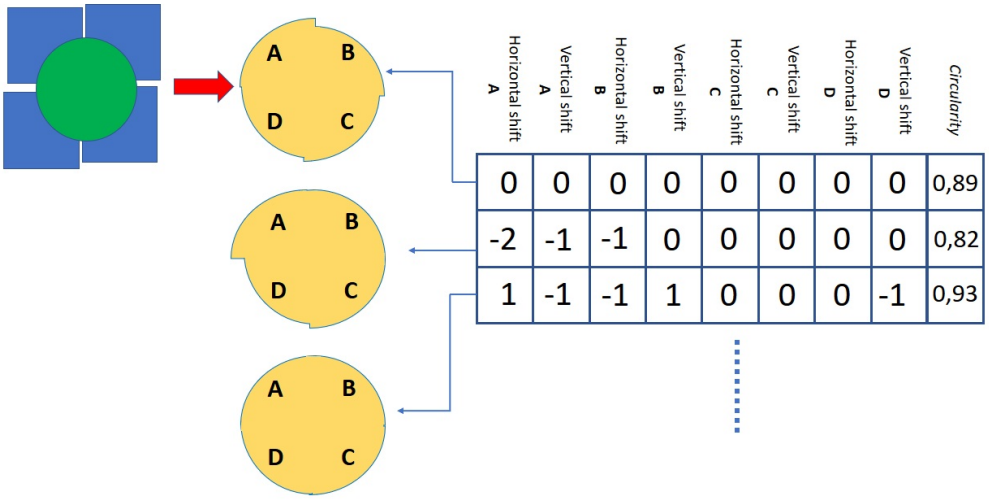

Figure 4.3: Graphical representation of the algorithm. The precision sphere (green circle) is placed in front of the quad Timepix (blue squares) and the radiography (yellow circle) is acquired. Because of the misalignment between the four matrices, the radiography presents artifacts in its shape, which are classified by the circularity factor. In the next steps, geometrical transformation are applied to radiography in order to maximize the circularity factor. When all the sets of transformations have been applied, the one genereting the best circularity factor is selected. Figure taken from *PAPER V* .

In order to facilitate the calculation of the optimum set of parameters, some operation must be executed before. The first step is the loading of the radiography followed by the image segmentation by thresholding, which is the conversion of a gray scale image into a simple black and white binary image, according to a certain value called *threshold value*. Such step is useful to isolate the relevant information inside the image, which is the circle in this case.
The second step of the algorithm is the computation of the perimeter length via polygonal approximation of a closed contour [54] and the area calculation, by summing all the pixels included in such perimeter.
Once both the perimeter and the area have been found, it is possible to classify the circle according to Eq.4.2, and to store this value in a dynamic vector. The program then apply the rototranslation transformations to each of the four sectors according to a new set of parameters, generating a new circle with slightly different perimeter and area. The routine starts again from the first step, accumulating time by time new values of the circularity factor. When all the set of parameters have been tested and all the circularity factors generated, a search for the highest value (the closest to 1) is done. This will univocally determine the best correction set and, as a consequence, an evaluation of how much the pixel matrices of the entire sensor were misaligned with respect to the ideal position.
Being the number of combinations exponentially dependent to the number of the po-

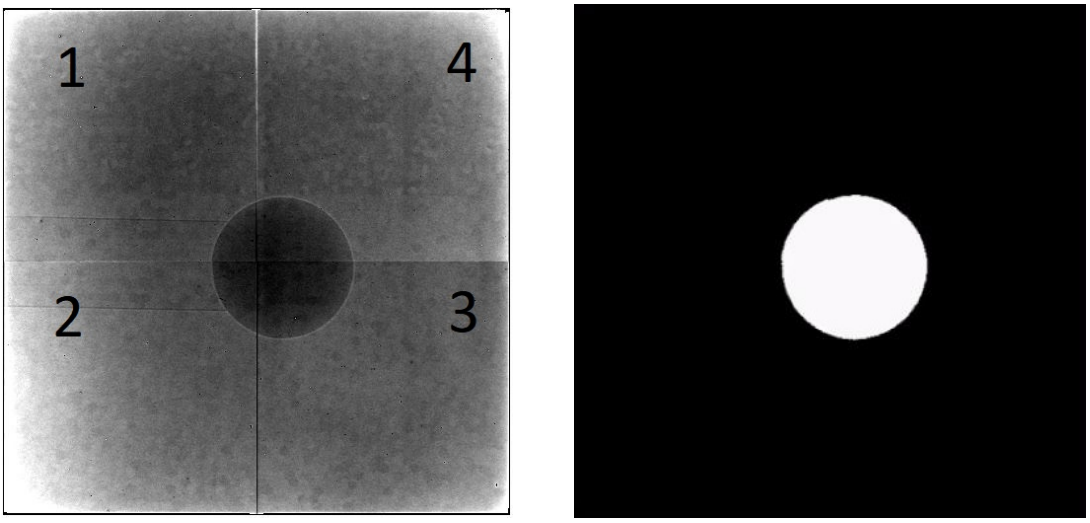

Figure 4.4: a) Left: radiography of the precision sphere without normalization. Four distinct regions, related to the pixel matrices, are clearly visible. The misalignment of the chips brings to a deformation of the circle. b) Right: same radiography after binarization.

tential transformations, a parallel-computation algorithm was implemented, able to route part of the elaboration processes to all the cores available in the the multi-core computer processor. The final step is the application of the calculated corrections on the original collected radiographies. In order to simplify and speed up this procedure, a graphical user interface was implemented. In this way, it is possible to select the folder where all the radiographies are saved and to apply such corrections with an automatized routine. This can be especially useful in the case where a volumetric reconstruction of the sample is needed, since these corrections must be applied to the entire stack of projections taken at several angles.
Despite the improvement brought by the alignment, the output generated by this software still shows some artifact (Fig.4.6), localized at the boundaries of the image. This is due to the lack of data in the region where the physical gap is located. In the current version of the correction algorithm, the missing portion of the image between two adjacent matrices of the quad Timepix sensor is reconstructed by a bilinear interpolation of the four nearest neighbour pixels [55]. Future development of the algorithm will include more sophisticated reconstruction methods.

4.2.2 Experimental design

The experiment was designed in order to comply the constraints of the high precision measurement. Four spheres of different materials (brass, teflon, stainless steel and brass) were tested on the neutron beam (Fig.4.5), to verify with an empirical procedure which of these was the most suitable for the test. After a comparison of the

contrast difference at the border of the circle generated by the electronic readout, the teflon and the chrome spheres resulted as the ones producing the image with the most defined contours, which was a fundamental prerequisite for the success of the experiment. The next step was the definition of the pinhole aperture. Taking into

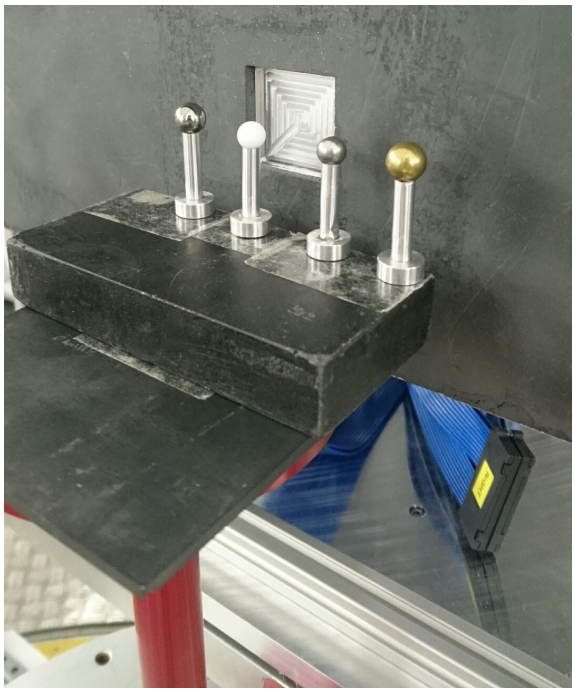

Figure 4.5: Four precision spheres of different material placed in front of the MCP detector camera.

account the blurring effect and the distance of the sample from the virtual neutron source, a pinhole size of 20 mm (L/D = 500) was chosen, to get a maximum blur width of 50 µm, below the size of one single pixel of the Timepix, which is 55 µm. In this way, the uncertainty of the measurement was reduced to the one related to the discretization of the image by the pixels, at the cost of a longer time of acquisition for the radiography.

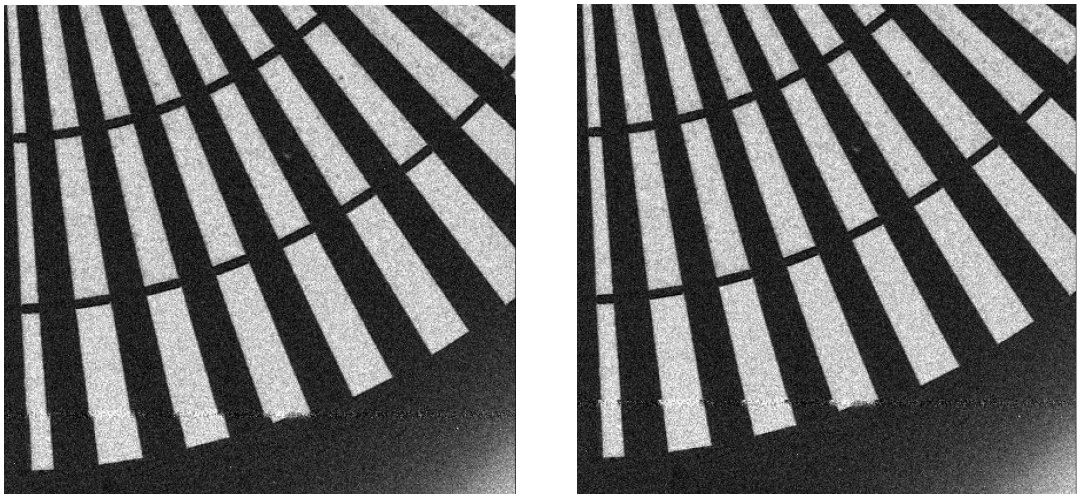

Figure 4.6: Left: detail of the Siemens star radiography used for image calibration before the correction with the algorithm. The artifact is visible at the edge between the two adjacent chips. Right: detail of the Siemens star radiography after the automatic correction. The misaglinement is reduced.

5 | Conclusions and outlook

In this thesis, the work carried out at the new cold neutron imaging and diffraction instrument IMAT (Imaging and Materials Science & Engineering) has been described. Due to its specifications, extensively described in *PAPER I*, IMAT is a world class beamline, capable to deal with a wide range of experimental studies. The combination of a pulsed spallation source and the suitable beamline design permits the time-of-flight analysis of samples in the wavelength range of 0.68 - 6.8 Å and a timing resolution up to 10 ns guaranteed by the Microchannel Plate neutron counting detector camera.
Such a detector enables the Bragg edge transmission imaging technique, providing a tool for the investigation of several case studies, including the crystallographic phase mapping of the specimens. This has been demonstrated in the experiment described in *PAPER II* , where the energy-dispersive analysis of a biological sample has been successfully carried out.
The effectiveness of the IMAT instrument was demonstrated in the non-destructive diagnosis of mechanical equipment as well. In fact, in the experiment described in *PAPER III* the possibility of revealing layers of neutron sensitive material whose thickness was below the pixel size of the detector camera was shown. This was done by exploiting a multiple radiography acquisition to achieve up to ~ 1 µm resolution. Moreover, a new technique has been implemented to exploit the hardware and software flexibility of the detector, called "centroiding mode", to achieve image resolutions up to ~ 20 µm. Despite the improvements brought by a higher spatial resolution, this operation mode can hardly be exploited in the experiments at IMAT facility. In fact, considering an integral neutron flux on sample of $\sim 2 \times 10^7$ [n/cm2/sec] and the statistics needed to make the centroiding algorithm working, the number of neutrons collected by each pixel in the Timepix readout is relatively low to permit a reasonable time of measurement of sample besides a white beam radiography. Anyway, the feasibility of the technique at IMAT instrument has been demonstrated in *PAPER IV* and can be considered in neutron research facilities characterized by a higher neutron flux. An example could be the future European Spallation Source (ESS) in Lund, Sweden, where the expected neutron flux is going to be ~ 30 times stronger.
A further aspect of the quad Timepix detector concerns the presence of artifacts in the radiographies, due to the misalignment of the four Timepix chips forming the electronic readout. In fact, although the assembly of four Timepix chips quadruples the field of view of the detector, the imperfect alignment among them causes the

formation of artifacts in the generated radiographies. This issue would be ideally resolved by the adoption of a single matrix of pixels with equivalent size with respect to the quad Timepix chip, but such solution has not been developed yet. By contrast, it is possible to correct the artifact with post-processing operations, like the one shown in this thesis, with acceptable results, as shown in *PAPER V*.
The work done so far paved the way for a strong innovation in the rising field of neutron imaging. The new IMAT facility will permit a wide variety of scientific studies, ranging from earth science to soft matter. Nonetheless, its flexible design enables the possibility of adding more features, one of the most interesting being the implementation of the new Timepix3 chip for TOF analyses without issues given by limited electronic readout capabilities. Such a feature could be exploited in the real time analysis of other biological samples with a particular inner morphology, as this aspect has been demonstrated to be effective in this thesis. Moreover, new experiments could be carried out to optimize the time needed for the creation of high resolution images by centroiding algorithm, acting on both the optics and the settings of the MCP detector, in view of the more powerful neutron beam which will be provided by the ESS in the next decades. Such high resolution radiographies would be nonetheless useful to improve the correction algorithm for the quad Timepix chip misalignment, for instance in the pixel interpolation methods at the image borders. This would substantially improve the final experimental outcomes, in terms of robustness and reliability in real case scenarios.

Acknowledgements

I wish to acknowledge the CNR-STFC Agreement 2014–2020 (N. 3420 2014–2020) concerning collaboration in scientific research at the ISIS Spallation Neutron Source, for financial support, as well as the University of Milano Bicocca for both the logistic and financial support.

Ci sono tante persone che hanno contribuito alla realizzazione di questo progetto di ricerca. A partire da Milano, dove ringrazio davvero il prof. Gorini, per aver risposto alla mia email con oggetto "Info per PHD" più di tre anni fa. Ovviamente, non posso che ringraziare tutto il nutrito gruppo della "Sala Break": Davidone, per tutte le perle di saggezza che mi ha regalato (e che ho anche registrato), Davidino, perché "Ma che fantastica storia è la vita?", Daniela, perché mi ha aiutato tanto con gli articoli e viziato altrettanto con i biscotti per celiaci, Mauro (o Maurizio?) per le sessioni di stretching in pausa caffè, Stefano, per la rubrica "Forse non tutti sanno che...", Mostafa, per le utili parole in persiano che mi ha insegnato, Roberto, per le utili frasi milanesi che mi ha insegnato, Silvia, perché mancano ancora quattro giorni a Natale, Giorgia, per lo stile "Shabby chic", Marica per lo stile metal, Enrico perché è sempre in pole-position. Devo per forza di cose ringraziare Roberta e Giovanni, per il loro indispensabile supporto nell'affrontare i mille problemi della burocrazia accademica.
Volando in Inghilterra, non posso che ringraziare almeno un migliaio di volte Tino, che mi ha aiutato in tutto e senza il quale questa tesi non ci sarebbe. Ringrazio Winfried, perché mi ha sempre dato tutto il supporto di cui avevo bisogno per svolgere gli esperimenti. Tra una radiografia e l'altra, una birra al pub era più che d'obbligo, insieme a "Quei di Abingdon", che ringrazio tutti per le chiacchierate al "The Narrows" e al "Nag's Head".
Al di fuori del mondo del dottorato, ringrazio i miei amici "di giù" che ci sono sempre stati: Sergio, Vincenzo, Ciccio e tutti gli altri, e i miei amici "di su", che non ho dimenticato.
Ringrazio tantissimo la mia famiglia, perché mi ha davvero sempre sostenuto e aiutato, e mio fratello, per l'approccio CFK che abbiamo ideato insieme e che mi è stato utile più di una volta.
Infine ringrazio Milano, perché nella sua vita diurna e notturna mi ha dato più di quanto avrei immaginato.

Bibliography

[1] Paul Breeze and Paul Breeze. Chapter 8 – Nuclear Fission. In *Nuclear Power*, pages 75–83. 2017.

[2] World Nuclear Association. Accelerator-driven Nuclear Energy. *World Nuclear Association*, pages 1–5, 2014.

[3] P Rinard. Neutron interactions with matter. *Passive Nondestructive Assay of Nuclear Materials, Los Alamos Technical Report NUREG/CR-5550, LA-UR-90-732*, pages 357–377, 1991.

[4] Niels Bohr and John Archibald Wheeler. The mechanism of nuclear fission. *Physical Review*, 1939.

[5] Gary J Russell. Spallation Physics - An Overview. *International Collaboration on Advanced Neutron Sources KEK. Tsukuba*, 1990.

[6] R E Masterson. *Introduction to Nuclear Reactor Physics*. 500 Tips. CRC Press, 2017.

[7] Heinz Maier-Leibnitz Zentrum. Neutron spectra at the entrance of the beam tubes at 20 MW reactor power at FRM II. https://www.mlz-garching.de/englisch/neutron-research/neutron-source.html.

[8] Javier Dawidowski, José Rolando Granada, Javier Roberto Santisteban, Florencia Cantargi, and Luis Alberto Rodríguez Palomino. Neutron Scattering Lengths and Cross Sections. pages 471–528. 2013.

[9] Boualem Hammouda. A TUTORIAL ON SMALL -ANGLE NEUTRON SCATTERING FROM POLYMERS. Technical report, National Institute of Standards and Technology, 1995.

[10] Heinz Maier-Leibnitz Zentrum. Experimental methods. https://www.mlz-garching.de/englisch/neutron-research/experimental-methods.html.

[11] O. Peter. Neutronen-Durchleuchtung. *Naturforsch*, 1:557, 1946.

[12] Markus Strobl. The Scope of the Imaging Instrument Project ODIN at ESS. In *Physics Procedia*, volume 69, pages 18–26, 2015.

[13] Nikolay Kardjilov, Ingo Manke, Robin Woracek, André Hilger, and John Banhart. Advances in neutron imaging, 2018.

[14] Anton S. Tremsin, Jason B. McPhate, Winfried A. Kockelmann, John V. Vallerga, Oswald H.W. Siegmund, and W. Bruce Feller. Energy-Rresolving neutron transmission radiography at the isis pulsed spallation source with a high-resolution neutron counting detector. *IEEE Transactions on Nuclear Science*, 56(5):2931–2937, 2009.

[15] J. R. Santisteban, L. Edwards, A. Steuwer, and P. J. Withers. Time-of-flight neutron transmission diffraction. *Journal of Applied Crystallography*, 2001.

[16] M. Strobl, W. Treimer, N. Kardjilov, A. Hilger, and S. Zabler. On neutron phase contrast imaging. *Nuclear Instruments and Methods in Physics Research, Section B: Beam Interactions with Materials and Atoms*, 266(1):181–186, 2008.

[17] M. Strobl, N. Kardjilov, A. Hilger, E. Jericha, G. Badurek, and I. Manke. Imaging with polarized neutrons. *Physica B: Condensed Matter*, 404(17):2611–2614, 2009.

[18] D. Liu, D. Hussey, M. V. Gubarev, B. D. Ramsey, D. Jacobson, M. Arif, D. E. Moncton, and B. Khaykovich. Demonstration of achromatic cold-neutron microscope utilizing axisymmetric focusing mirrors. *Applied Physics Letters*, 102(18), 2013.

[19] Pavel Trtik and Eberhard H. Lehmann. Progress in High-resolution Neutron Imaging at the Paul Scherrer Institut-The Neutron Microscope Project. In *Journal of Physics: Conference Series*, volume 746, 2016.

[20] Daniel S. Hussey. An overview of neutron imaging. Technical report, NIST - Physical Measurement Laboratory, 2012.

[21] Takashi Hibiki and Kaichiro Mishima. Prediction of measurement error due to low gray scale and spatial resolution of an imaging system on quantification of neutron radiographic image. *Nuclear Instruments and Methods in Physics Research, Section A: Accelerators, Spectrometers, Detectors and Associated Equipment*, 388(1-2):204–211, 1997.

[22] Thorsten Buzug. *Computed tomography: From photon statistics to modern cone-beam CT.*

[23] J Radon. Über die {B}estimmung von {F}unktionen durch ihre {I}ntegralwerte längs gewisser {M}annigfaltigkeiten. *Akad. Wiss.*, 69:262–277, 1917.

[24] Anton S. Tremsin, John V. Vallerga, Jason B. McPhate, Oswald H. W. Siegmund, and Rick Raffanti. High Resolution Photon Counting With MCP-Timepix Quad Parallel Readout Operating at $>$ 1 kHz Frame Rates. *IEEE Transactions on Nuclear Science*, 60(2):578–585, apr 2013.

[25] Tom Malzbender. Fourier volume rendering. *ACM Transactions on Graphics*, 1993.

[26] Kees Joost Batenburg, Willem Jan Palenstijn, and Jan Sijbers. Projection and backprojection in tomography: design choices and considerations. In *Workshop on Applications of Discrete Geometry and Mathematical Morphology*, pages 106–110, 2010.

[27] A. H. Andersen and A. C. Kak. Simultaneous algebraic reconstruction technique (SART): A superior implementation of the art algorithm. *Ultrasonic Imaging*, 1984.

[28] Van Hemelryck Tessa, Wuyts Sarah, Goossens Maggie, Batenburg Kees Joost, and Sijbers Jan. The implementation of iterative reconstruction algorithms in MATLAB. *Sciences-New York*, 2007.

[29] Triestino Minniti, Kenichi Watanabe, Genoveva Burca, Daniel E. Pooley, and Winfried Kockelmann. Characterization of the new neutron imaging and materials science facility IMAT. *Nuclear Instruments and Methods in Physics Research, Section A: Accelerators, Spectrometers, Detectors and Associated Equipment*, 888:184–195, 2018.

[30] J. Gethyn Timothy. Microchannel plates for photon detection and imaging in space. *Observing Photons in Space*, (1930):365–390, 2010.

[31] Joseph Ladislas Wiza and Others. Microchannel plate detectors. *Nucl. Instrum. Methods*, 162(1-3):587–601, 1979.

[32] Bruce Laprade and Ron Starcher. The 2 micron pore microchannel plate. Development of the world's fastest detector. Technical report, BURLE Electro-Optics, Inc., 2001.

[33] A. Franco, J. Geissbühler, N. Wyrsch, and C. Ballif. Fabrication and characterization of monolithically integrated microchannel plates based on amorphous silicon. *Scientific Reports*, 4, 2014.

[34] G. W. Fraser and J. F. Pearson. The direct detection of thermal neutrons by imaging microchannel-plate detectors. *Nuclear Inst. and Methods in Physics Research, A*, 293(3):569–574, 1990.

[35] J. Vallerga, R. Raffanti, A. Tremsin, J. McPhate, and O. Siegmund. MCP detector read out with a bare quad Timepix at kilohertz frame rates. In *Journal of Instrumentation*, 2011.

[36] X. Llopart, R. Ballabriga, M. Campbell, L. Tlustos, and W. Wong. Timepix, a 65k programmable pixel readout chip for arrival time, energy and/or photon counting measurements. *Nuclear Instruments and Methods in Physics Research, Section A: Accelerators, Spectrometers, Detectors and Associated Equipment*, 581(1-2 SPEC. ISS.):485–494, 2007.

[37] Anton S. Tremsin, John V. Vallerga, Jason B. McPhate, Oswald H.W. Siegmund, and Rick Raffanti. High resolution photon counting with MCP-timepix quad parallel readout operating at more than 1 KHz frame rates. *IEEE Transactions on Nuclear Science*, 60(2):578–585, 2013.

[38] V. Finocchiaro, F. Aliotta, D. Tresoldi, R. C. Ponterio, C. S. Vasi, and G. Salvato. The autofocusing system of the IMAT neutron camera. *Review of Scientific Instruments*, 84(9), 2013.

[39] W. H. Miller. *Treatise on Crystallography*. For J. & J. J. Deighton, 1839.

[40] National Institutes of Health (NIH). ImageJ. https://imagej.nih.gov/ij/index.html.

[41] A. S. Tremsin, J. V. Vallerga, J. B. McPhate, and O. H W Siegmund. Optimization of Timepix count rate capabilities for the applications with a periodic input signal. In *Journal of Instrumentation*, 2014.

[42] T Poikela, J Plosila, T Westerlund, M Campbell, M De Gaspari, X Llopart, V Gromov, R Kluit, M van Beuzekom, F Zappon, V Zivkovic, C Brezina, K Desch, Y Fu, and A Kruth. Timepix3: a 65K channel hybrid pixel readout chip with simultaneous ToA/ToT and sparse readout. *Journal of Instrumentation*, 9(05):C05013, 2014.

[43] Triestino Minniti. Bragg Edge Analysis for TRansmission Imaging eXperiments software tool : BEATRIX. *Journal of Applied Crystallography*, (under review).

[44] M M Organo, P T Rtik, M M Eyer, E H L Ehmann, H Ovind, and M S Trobl. Unlocking high spatial resolution in neutron imaging through an add-on fibre optics taper. *Optics Express*, 2018.

[45] Alessandra Giuliani, Serena Mazzoni, Alessandra Ruggiu, Barbara Canciani, Ranieri Cancedda, and Sara Tavella. High-resolution X-Ray tomography: A 3D exploration into the skeletal architecture in mouse models submitted to microgravity constraints, 2018.

[46] F. Sauli. GEM: A new concept for electron amplification in gas detectors. *Nuclear Instruments and Methods in Physics Research, Section A: Accelerators, Spectrometers, Detectors and Associated Equipment*, 1997.

[47] JANIS 4.0 - OECD Nuclear Energy Agency. https://www.oecd-nea.org/janis/.

[48] Klaus Suhling, Robert W. Airey, and Brian L. Morgan. Optimisation of centroiding algorithms for photon event counting imaging. *Nuclear Instruments and Methods in Physics Research, Section A: Accelerators, Spectrometers, Detectors and Associated Equipment*, 1999.

[49] Klaus Suhling, Robert W. Airey, and Brian L. Morgan. Minimization of fixed pattern noise in photon event counting imaging. *Review of Scientific Instruments*, 2002.

[50] Peter D Burns. Slanted-Edge MTF for Digital Camera and Scanner Analysis. *Burns*, 2000.

[51] M. Strobl. ESS Instrument Construction Proposal: ODIN – Optical and Diffraction Imaging with Neutrons. Technical report, 2012.

[52] Mathworks. MATLAB. https://it.mathworks.com/products/matlab.html.

[53] Mathworks. *Image Processing Toolbox™, Reference.*

[54] A. M. Vossepoel and A. W.M. Smeulders. Vector code probability and metrication error in the representation of straight lines of finite length. *Computer Graphics and Image Processing*, 1982.

[55] Earl J. Kirkland. Bilinear Interpolation. In *Advanced Computing in Electron Microscopy*. 2010.

List of Figures

Synopsis of attached papers

The abstracts of the papers presented in this thesis are listed here.

I. **Time-of-Flight Neutron Imaging on IMAT@ISIS: A New User Facility for Materials Science.**
The cold neutron imaging and diffraction instrument IMAT at the second target station of the pulsed neutron source ISIS is currently being commissioned and prepared for user operation. IMAT will enable white-beam neutron radiography and tomography. One of the benefits of operating on a pulsed source is to determine the neutron energy via a time of flight measurement, thus enabling energy-selective and energy-dispersive neutron imaging, for maximizing image contrasts between given materials and for mapping structure and microstructure properties. We survey the hardware and software components for data collection and image analysis on IMAT, and provide a step-by-step procedure for operating the instrument for energy-dispersive imaging using a two-phase metal test object as an example.

II. **Energy-resolved neutron tomography of an unconventional cultured pearl at a pulsed spallation source using a microchannel plate camera.**
A non-destructive neutron analysis technique performed at the IMAT beamline of the STFC (Science and Technology Facility Council), UK, is presented. In this experiment, neutrons of different energy have been exploited to obtain a tomographic reconstruction of a biomineralic sample, more specifically a cultured pearl, by using a time-resolving pixel camera, the MicroChannel Plate (MCP) detector, utilizing an array of 2×2 Timepix readout chips. The MCP camera is capable of energy-resolved two-dimensional mapping of neutron transmission with a spatial resolution of 55 µm. By using a Simultaneous Iterative Reconstruction Technique (SIRT), virtual sections of the internal part of the sample have been created, thus revealing several features inside its bulk. The crystallographic phase map via Bragg edge analysis, showing a phase fraction distribution on the entire specimen, has been generated as well. Finally, 3D volume rendering of the pearl is presented.

III. **Measurement of the thickness of B4C deposits over 3D grids via multi-angle neutron radiography.**

At the present time, different kinds of thermal neutron detectors are under development at the European Spallation Source research facility, in order to overcome the well-known problem of the ^{3}He shortage. One of these new systems relies on the use of a three-dimensional neutron converter cathode that consists of a stack of aluminum grids, covered by a 0.9 µm ^{10}B enriched boron carbide layer ($^{10}B_4C$). As the conversion efficiency is a function of the boron thickness and the mean free path of the charged particles produced in the neutron induced reaction, the characterization of the boron carbide layer uniformity over the grids becomes crucial. In this work, a non-destructive method to map the thickness distribution of the converter layer over the grids is shown. The measurements exploit the white-beam neutron radiography technique where the specimen is irradiated at different angles. This experiment has been performed at the IMAT beamline operating at the ISIS spallation neutron source (UK). The results confirm that this non-destructive, wide-ranging technique allows a reliable and fast sample characterization and that it may be exploited in similar analyses where equivalent requirements are requested.

IV. **Towards high-resolution neutron imaging on IMAT.**
IMAT is a new cold-neutron imaging facility at the neutron spallation source ISIS at the Rutherford Appleton Laboratory, U.K.. The ISIS pulsed source enables energy-selective and energy-resolved neutron imaging via time-of-flight (TOF) techniques, which are available in addition to the white-beam neutron radiography and tomography options. A spatial resolution of about 50 µm for white-beam neutron radiography was achieved early in the IMAT commissioning phase. In this work we have made the first steps towards achieving higher spatial resolution. A white-beam radiography with 18 µm spatial resolution was achieved in this experiment. This result was possible by using the event counting neutron pixel detector based on micro-channel plates (MCP) coupled with a Timepix readout chip with 55 µm sized pixels, and by employing an event centroiding technique. The prospects for energy-selective neutron radiography for this centroiding mode are discussed.

V. **Investigation of image distortion due to MCP electronic readout misalignment and correction via customized GUI application.**
The MCP-based neutron counting detector is a novel device that allows high spatial resolution and time-resolved neutron radiography and tomography with epithermal, thermal and cold neutrons. Time resolution is possible by the high readout speeds of $\sim$ 1200 frames/sec, allowing high resolution event counting with relatively high rates without spatial resolution degradation due to event overlaps. The electronic readout is based on a Timepix sensor, a CMOS pixel readout chip developed at CERN. Currently, a geometry of a quad Timepix detector is used with an active format of $28 \times 2\ 28$ mm^2 limited by the size of the Timepix quad (2×2 chips) readout. Measurements of a set of high-precision micrometers test samples have been performed at the Imaging and Materials Science & Engineering (IMAT) beamline operating at the ISIS spallation neu-

tron source (U.K.). The aim of these experiments was the full characterization of the chip misalignment and of the gaps between each pad in the quad Timepix sensor. Such misalignment causes distortions of the recorded shape of the sample analyzed. We present in this work a post-processing image procedure that considers and corrects these effects. Results of the correction will be discussed and the efficacy of this method evaluated.

Paper I

Journal of *Imaging*

MDPI

Article

Time-of-Flight Neutron Imaging on IMAT@ISIS: A New User Facility for Materials Science

Winfried Kockelmann [1,*], Triestino Minniti [1], Daniel E. Pooley [1], Genoveva Burca [1], Ranggi Ramadhan [2], Freddie A. Akeroyd [1], Gareth D. Howells [1], Chris Moreton-Smith [1], David P. Keymer [1], Joe Kelleher [1], Saurabh Kabra [1], Tung Lik Lee [1], Ralf Ziesche [3], Anthony Reid [4], Giuseppe Vitucci [5], Giuseppe Gorini [5], Davide Micieli [6], Raffaele G. Agostino [6], Vincenzo Formoso [6], Francesco Aliotta [7], Rosa Ponterio [7], Sebastiano Trusso [7], Gabriele Salvato [7], Cirino Vasi [7], Francesco Grazzi [8], Kenichi Watanabe [9], Jason W. L. Lee [10], Anton S. Tremsin [11], Jason B. McPhate [11], Daniel Nixon [1,12], Nick Draper [1,12], William Halcrow [1] and Jim Nightingale [1]

1 STFC-Rutherford Appleton Laboratory, ISIS Facility, Harwell OX11 0QX, UK; triestino.minniti@stfc.ac.uk (T.M.); daniel.pooley@stfc.ac.uk (D.E.P); genoveva.burca@stfc.ac.uk (G.B.); freddie.akeroyd@stfc.ac.uk (F.A.A.); gareth.howells@stfc.ac.uk (G.D.H.); c.m.moreton-smith@stfc.ac.uk (C.M.-S.); david.keymer@stfc.ac.uk (D.P.K.); joe.kelleher@stfc.ac.uk (J.K.); saurabh.kabra@stfc.ac.uk (S.K.); tung-lik.lee@stfc.ac.uk (T.L.L.); daniel.nixon@stfc.ac.uk (D.N.); nick.draper@stfc.ac.uk (N.D.); william.halcrow@stfc.ac.uk (W.H.); jim.nightingale@stfc.ac.uk (J.N.)
2 Centre for Manufacturing and Materials Engineering, University of Coventry, Coventry CV1 5FB, UK; ramadhar@uni.coventry.ac.uk
3 Department of Chemical Engineering, University College London, London WC1E 7JE, UK; ralf.ziesche.16@ucl.ac.uk
4 Department of Mechanical Engineering, University of Sheffield, Sheffield S1 3JD, UK; agpreid1@sheffield.ac.uk
5 Department of Physics, University of Milano Bicocca, 20125 Milan, Italy; g.vitucci@campus.unimib.it (G.V.); gorini@ifp.cnr.it (G.G.)
6 Department of Physics, University of Calabria, 87036 Rende (Cosenza), Italy; Micielidavide@gmail.com (D.M.); raffaele.agostino@fis.unical.it (R.G.A.); vincenzo.formoso@fis.unical.it (V.F.)
7 CNR—Istituto per i Processi Chimico-Fisici (IPCF), 98158 Messina, Italy; francesco.aliotta@cnr.it (F.A.); ponterio@ipcf.cnr.it (R.P.); trusso@me.cnr.it (S.T.); gabriele.salvato@cnr.it (G.S.); cirinosalvatore.vasi@cnr.it (C.V.)
8 CNR—Istituto di Fisica Applicata (IFAC), 50019 Sesto Fiorentino, Italy; f.grazzi@ifac.cnr.it
9 Graduate School of Engineering, Nagoya University, Furo-cho, Chikusa-ku, Nagoya 464-8603, Japan; kenichi.watanabe@stfc.ac.uk
10 Department of Chemistry, University of Oxford, Oxford OX1 3TA, UK; jason.lee@chem.ox.ac.uk
11 Space Science Laboratory, University of California at Berkeley, Berkeley, CA 94720, USA; ast@ssl.berkeley.edu (A.S.T.); mcphate@ssl.berkeley.edu (J.B.M.)
12 Tessella, Abingdon OX14 3YS, UK
* Correspondence: winfried.kockelmann@stfc.ac.uk; Tel.: +44-1235-446731

Received: 11 January 2018; Accepted: 23 February 2018; Published: 28 February 2018

Abstract: The cold neutron imaging and diffraction instrument IMAT at the second target station of the pulsed neutron source ISIS is currently being commissioned and prepared for user operation. IMAT will enable white-beam neutron radiography and tomography. One of the benefits of operating on a pulsed source is to determine the neutron energy via a time of flight measurement, thus enabling energy-selective and energy-dispersive neutron imaging, for maximizing image contrasts between given materials and for mapping structure and microstructure properties. We survey the hardware and software components for data collection and image analysis on IMAT, and provide a step-by-step procedure for operating the instrument for energy-dispersive imaging using a two-phase metal test object as an example.

Keywords: time-of-flight; energy-selective imaging; energy-dispersive imaging; pulsed neutron source; Bragg edge imaging; neutron tomography; neutron radiography

1. Introduction

In the last decade neutron imaging at pulsed neutron sources has been developed as an essential tool for materials science and engineering studies [1–4]. Time-of-flight (TOF) energy-dispersive neutron imaging at a pulsed source enables mapping of compositional and structural (phase, strain and texture) variations in metals [5–7] and imaging of phase transformations [8] with submillimeter spatial resolution. Moreover, spatial mapping of element compositions and remote temperatures via neutron resonance transmission analysis [9–12], and TOF imaging of magnetic fields [13] have been performed. Recently, 3D diffraction imaging via a TOF transmission technique has been verified [14], and the concept of mapping small angle scattering signals via wavelength-dispersive dark-field imaging has been demonstrated [15].

Most energy-dispersive imaging applications on TOF instruments are concerned with mapping structural parameters via Bragg edge analysis. Bragg diffraction removes neutrons from the incident beam, thus producing Bragg edges in the transmitted intensity as a function of wavelength. A Bragg edge transmission analysis can provide phase, strain and texture parameters of a material [16,17], and neutron radiography and tomography techniques can be employed to obtain 2D and 3D maps of those parameters. Bragg edge analysis works well with metals e.g., [18,19] but it has been applied for mapping mineral phases as well e.g., [20]. 3D reconstruction of elastic strains is being considered for systems under certain boundary conditions [21] whilst the ill-posed problem for strain tomography has been pointed out [22]. It should be noted that parallel to developments of Bragg edge analysis at pulsed sources, energy-resolved analysis at steady state sources is achieved by tuning the neutron energy using a double-crystal monochromator [23], allowing 2D and 3D mapping of structure parameters and phase transformations [24].

The fast development of TOF imaging is driven by the need for advanced materials research. In the past decade there have been significant developments in the design and installation of new imaging instruments on the one hand [2,25–29], and advances with detection systems on the other hand [30–33]. Accordingly, the available instruments and methods have made substantial progress since the early feasibility studies using a gated CCD camera [1]. Notably, two dedicated neutron imaging user facilities have been constructed at pulsed sources, namely RADEN [2] at J-PARC and IMAT [25,26,29] at ISIS. IMAT was installed on the 10 Hz pulsed source of the ISIS second target station at the Rutherford Appleton Laboratory, with substantial in-kind contributions from the Italian CNR. The beamline has recently seen cold and hot commissioning and is now being prepared for a user program. The instrument parameters have been determined [29], and the imaging cameras have been characterized [31,34,35].

Here we provide a first review of the instrument components used for TOF imaging on the new beamline, and we outline the set-up of the instrument as a user facility. The data collection and image analysis on IMAT is demonstrated using the same shrink-fitted Cu–Fe test object that was used in the earlier pilot study [1]. A detailed step-by-step guide includes the important aspects when performing a Bragg edge imaging experiment on IMAT. This paper complements the earlier description and characterization of the instrument for white-beam imaging [29].

2. TOF Imaging and Instrument Description

2.1. TOF Imaging

On a pulsed source energy-resolved imaging is enabled by a TOF analysis of the neutrons transmitted or scattered by the sample. This mode requires synchronization of the beamline

components with the pulse generation, i.e., for choppers, monitors and cameras, using an external trigger signal which is provided by the source and marks the generation of neutrons in the target. For each pixel of a neutron camera the time of the neutron arrival relative to this trigger is measured. The wavelengths of the detected neutrons are calculated from their time of flight by

$$\lambda = \frac{h(T + \Delta T_0)}{mL} = 3957 \times \frac{(T + \Delta T_0)}{L} \quad (1)$$

where λ is the neutron wavelength (in Angstrom), h is Planck's constant, T is the neutron time of flight (in seconds), ΔT_0 is the time offset of the source trigger received by the data processing electronics (in seconds), m is the neutron mass, and L is the flight path from source to camera (in meters).

An overview of the TOF imaging set-up and the signal processing for an energy-dispersive measurement on IMAT is shown in Figure 1. At the heart of this figure are the sample and the pixel detector, here for the example of the GP2 detector [30,31]. The detector is placed at a known distance from the source. On IMAT, a neutron pulse is generated and moderated every 100 ms, and the flight path to the camera is about 56 m. The wavelength dispersion of the incoming pulses is illustrated by the different colors of the neutrons, with the higher energy (red) neutrons arriving earlier in the camera than the low energy (blue) neutrons. The energy dependence of the beam attenuation of the incoming neutron pulses is reflected by the 'color-dependent' reduction of neutrons as they transverse the sample. In the camera, each neutron is individually and uniquely tagged in position and time within each neutron pulse.

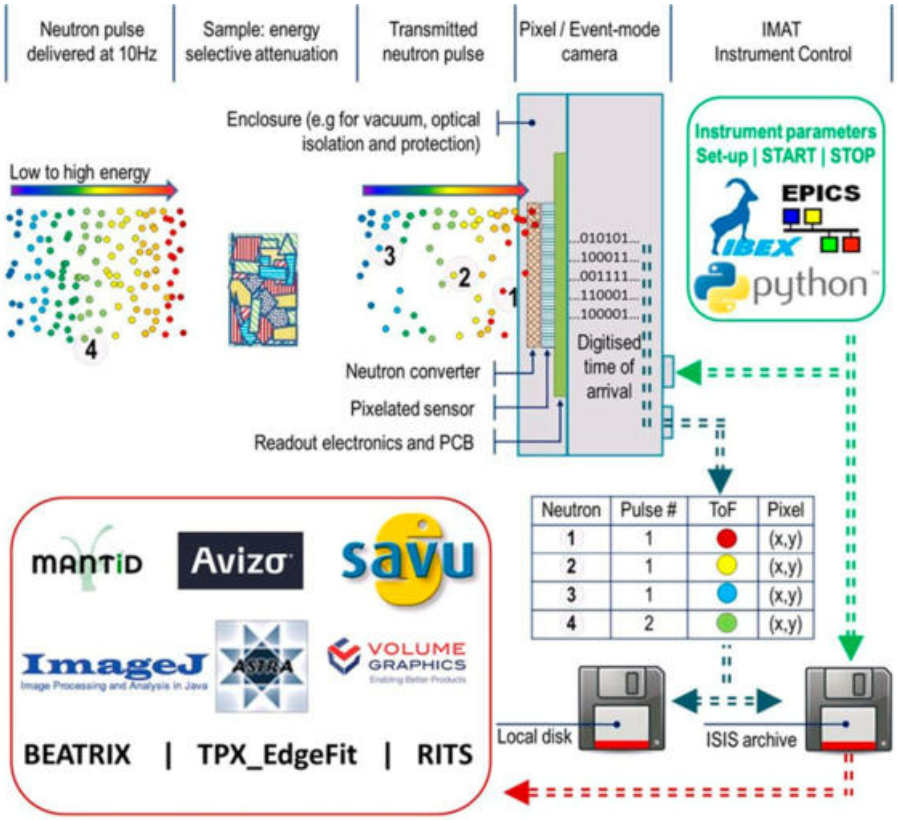

Figure 1. Time-of-flight (TOF) imaging schematic. The sketch illustrates the energy-dependent beam attenuation, as measured in a TOF imaging experiment. The TOF pixel detector records every neutron's arrival time, with its (x,y) position. Four neutrons, labeled 1–4, from two separate neutron pulses are labelled to illustrate and emphasize this point. The camera is controlled via the IBEX GUI used on IMAT. For the image analysis a range of tools is available.

The imaging camera (or pixel detector) is operated via the IBEX [36] instrument control program which is based on the EPICS [37,38] software tools and libraries. The registered neutrons are stored as images or event lists, and treated with a toolbox of image analysis packages. A typical raw data size for a white-beam radiography and an energy-dispersive radiography is 8 Mbyte and 1.5 GByte, respectively. An event-mode generated energy-dispersive data set for 10 k pixels and 4000 k time bins is of the order of 5 GByte per hour. For the size of a tomography data set these numbers are to be multiplied by the number of projections.

There are two important parameters to be considered when defining the performance of a time-of-flight imaging instrument: (i) The maximum value of the wavelength band; (ii) the wavelength resolution. The maximum wavelength band is defined by the need to avoid frame overlap, i.e., the superposition of neutrons coming from different neutron pulses into the same time frame. The wavelength band width is given by:

$$\Delta\lambda = \frac{3957}{L \times f} \tag{2}$$

where f is the repetition rate, and L is the flight path from source to pixel detector. The repetition rate is usually the pulse frequency of neutron source, but can be set to values lower than the source frequency using neutron choppers by suppressing pulses from the source. For a flight path of 56 m and a frequency of 10 Hz the wavelength band width is about 7 Å. With the suppression of every other pulse by a chopper system the effective pulse frequency is 5 Hz, and the band width is about 14 Å. The accessible maximum wavelength range defines which energy-dependent features, e.g., Bragg edges, are observed in one acquisition.

The wavelength resolution of the instrument is determined by the uncertainty $\delta\lambda$ to which a given wavelength can be determined. The actual width and shape of the neutron pulse for a particular wavelength, and its dependence on wavelength, are complex functions dictated by the type, geometry and physical processes occurring within the moderator. For a given wavelength, the relative uncertainty $\delta\lambda/\lambda$ determines the broadening of a feature, e.g., a Bragg edge, in a TOF spectrum. The resolution function for IMAT has been determined recently [29].

In summary, on a TOF instrument energy-resolving or wavelength-discriminating measurements are performed in a straightforward way, allowing for monochromatic, energy-selective and energy-dispersive neutron imaging, in addition to 'white-beam' and 'pink-beam' (narrow wavelength range) imaging applications. The hardware and electronic time resolutions of TOF cameras and detectors are often much better than the intrinsic instrument resolution. With this in mind, we use the term 'energy-selective neutron imaging' if neutron radiographies are collected for one or more, wide or narrow, wavelength bands. Selecting certain wavelength bands is useful, for example, for enhancing contrasts by exploiting the variation of the attenuation with energy, be it for different materials or for different phases of the same material. 'Monochromatic neutron imaging' is a special case of energy-selective imaging if one narrow energy channel is selected. Furthermore, energy-selection is a prerequisite for 'energy-dispersive neutron imaging' where histogramming or scanning within a wavelength range is performed with a sufficiently fine bin-width, for example across a Bragg edge of a material.

2.2. IMAT Instrument

2.2.1. Source and Choppers

IMAT [25,26] is a cold-neutron imaging facility installed on the ISIS second target station TS2, a low-power 10 Hz pulsed source of about 50 kW. The length of the beamline from source to sample position is 56 m. Figure 2 shows design drawings of the full length of the instrument and a detailed depiction of the sample area. Further illustrations of the instrument set-up are provided in Figure 3. Neutrons at ISIS are produced by spallation reactions induced by high-energy protons impinging

on a tungsten target. IMAT is installed on the coupled 18 K hydrogen moderator on beamport W5. The neutrons exiting the moderator are transported by a straight, $m = 3$, evacuated supermirror guide to the sample area. A 20 Hz T_0 chopper at 12.75 m from the moderator serves as fast neutron and gamma filter. Two 10 Hz double-disk choppers (at 12.2 m and 20.4 m) are used to define wider (e.g., 6 Å) or narrower (e.g., 1 Å) wavelength bands but also to prevent frame-overlap of neutrons between successive time frames.

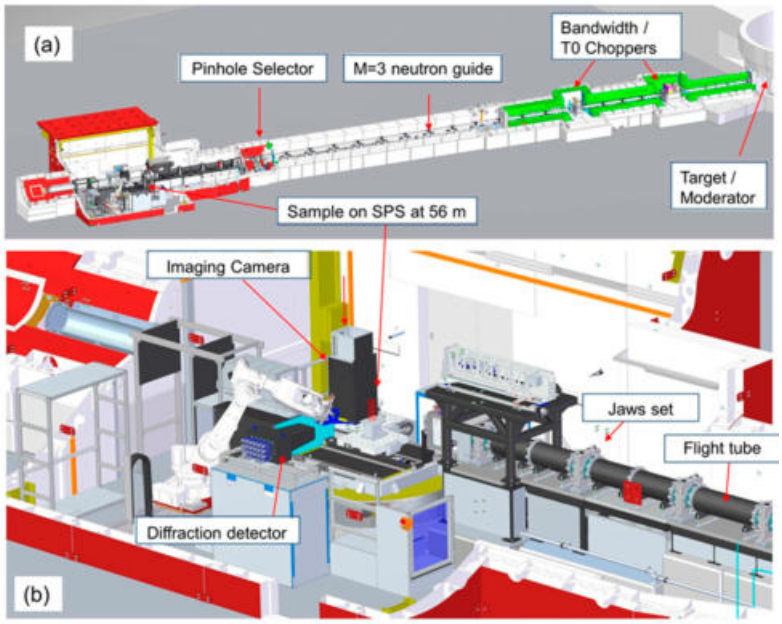

Figure 2. IMAT instrument layout. (**a**) The length of the instrument from source to sample position is 56 m. (**b**) The main components in the sample area are: evacuated flight tubes; beam limiting jaws; sample positioning system (SPS); imaging camera; diffraction prototype detector.

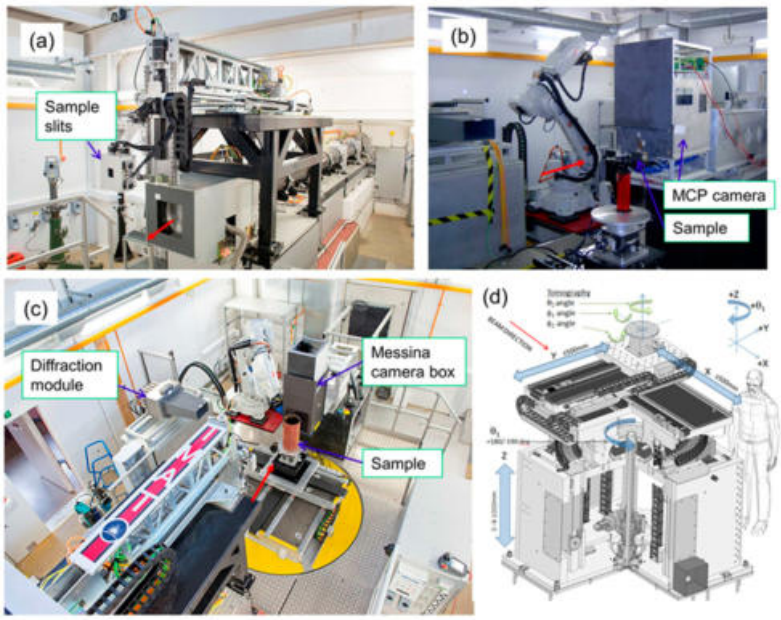

Figure 3. Installation of IMAT on TS2. (**a**) upstream view from the sample point showing flight tubes and sample slits (out of beam) inside the blockhouse; (**b**) MCP detector setup; (**c**) sample area view through the open roof into the IMAT blockhouse, with the Messina camera box carried by a robotic arm; (**d**) concept drawing of the sample positioning system (SPS).

2.2.2. Beamline Components

The neutron guide ends just upstream of a pinhole selector at 46 m. The pinhole produces a quasi-parallel neutron beam adopting a specific divergence (or L/D) value, where D is the diameter of the aperture and L is the distance to the neutron camera. However, it should be noted that the L/D value is affected by both the divergence characteristic of the guide and the pinhole geometry [29]. The remote-controllable pinhole selector wheel offers a choice of five circular apertures, to define different L/D ratios between 125 and 2000, and one large square aperture of 100 × 100 mm^2. The selector uses a system of changeable cartridges into which neutron-absorbing sheets (typically consisting of boron based materials) with circular or rectangular apertures are inserted. Between the end of the supermirror guide at 45.7 m and the pinhole selector a filter or diffuser can be inserted into the beam if required. The purpose of a beam diffuser is to wash out spatial inhomogeneities in the neutron beam which are present mostly due to the finite moderator size and gaps in the neutron guide for choppers, monitors and vacuum valves. A non-hydrogenous, small angle scattering material is considered as diffuser. A graphite diffuser is currently being evaluated for IMAT; so far, the filter cartridge was kept empty.

From the pinhole the neutrons travel through approximately 9 m of evacuated flight tubes of 320 mm diameter (Figure 3a), before reaching the nominal sample position at 10 m from the pinhole selector. An pneumatically-driven attenuator ('fast shutter') made of an ^{10}B-coated Al-sheet is installed upstream from the sample position as neutron absorbing blade that is driven into the beam to reduce flux on the sample, thereby minimizing sample and camera activation when data is not being taken.

Four diagnostic TOF 40μ-vanadium-foil beam monitors are installed along the beamline, at 11.7 m (M1), 19.8 (M2), 20.9 m (M3), and 46.2 m (M4) from the moderator, to inform about the status of the incident beam. M1 to M3 are positioned before and after the choppers; M4 is positioned directly after the pinhole. A fifth, retractable monitor (M5) with a thickness of 100 μm of the vanadium foil installed at 49.0 m will be used for normalization of diffraction data. This monitor is usually driven out of the beam for imaging experiments. An additional, portable TOF neutron beam monitor is available for characterization of the beam spectrum at the sample position. The latter monitor uses a ^{6}Li-based GS1 glass scintillator (^{7}Li-2.4%wt^{6}Li) with an active volume of 0.95 × 0.96 × 0.95 mm^3. The monitor is calibrated against measured and Monte Carlo simulated scattering data.

The IMAT beam size can be varied between 1 × 1 mm^2 and 200 × 200 mm^2 using five sets of 'jaws' each made of four blades of 10 mm thick sintered boron-carbide. A set of retractable sample slits (using four 3 mm thick ^{10}B blades and with adjustment options along the beam direction) can be used to define a small aperture between 1 × 1 mm^2 and 50 × 50 mm^2. As such, the slit set produces a well-defined beam size just in front of the sample. The sample slit system and its support frame can be seen in Figure 3a.

The IMAT sample positioning system (SPS) with its reference at 56 m from the source is used for sample alignment, and for sample rotation for tomography experiments. The SPS has seven axes for sample movements: a large rotation (Θ_1; range: 360 degrees), three linear stages ('X', 'Y', 'Z'; ranges: 1 m), two orthogonal tilts (φ_1, φ_2; range 10 degrees), a tomography rotation stage (Θ_2, range: 360 degrees). The x, y, and z directions of the SPS in their home positions are in beam direction, transverse direction and vertical direction, respectively, consistent with the coordinate system of IMAT. A concept design drawing of the SPS is given in Figure 3d. The SPS is designed to lift and accurately position 1.5 t loads. The tomography rotation stage can carry smaller samples <50 kg; the stage can be dismounted if required. For sample alignment a laser beam along the incident neutron beam and two theodolites are available.

A detailed description of the instrument and its measured performance has been given recently [25,26,29]. It should be noted that IMAT is about to be equipped with additional diffraction detectors, for strain and texture analysis via neutron diffraction. A prototype diffraction module is shown in Figures 2b and 3c.

2.2.3. IMAT Cameras

Three camera systems are available on IMAT, including two TOF pixel detectors. TOF pixel detectors with high spatial and high timing resolution are essential for performing energy-dispersive measurements on a pulsed-source instrument like IMAT. The currently available cameras and detectors are listed in Table 1 with their main parameters.

Table 1. Current IMAT camera options.

Camera/Detector Type	Camera/Detector Parameters	Energy-Selection Options and Special Features
Berkeley MCP (Timepix 2)		
Field of View (mm^2)	28 × 28	
Pixel Size (μm)	55	- TOF: Triggered by source
Number of Pixels	512 × 512	- Energy-dispersive
Number of Time Bins	3100	- High neutron detection efficiency
Smallest Time Bin (ns)	~10	
Registers per pixel	1	
Detection efficiency	up to 40% for cold neutrons	
Oxford-ISIS GP2		
Field of View (mm^2)	22.7 × 22.7	
Pixel Size (μm)	70	- TOF: Triggered by source
Number of Pixels	324 × 324	- Energy-dispersive
Number of Time Bins	4096	- Compact design: 15 cm × 15 cm × 11 cm
Smallest Time Bin (ns)	12.5	
Registers per pixel	4	
Detection efficiency	7.5% at 2.5 Å	
Messina Tomography Camera Box		- Flexible design; autofocus
Field of View (mm^2)	60 × 60–210 × 210	(i) White beam camera; coarse energy selection via choppers
Effective Pixel Size (2048) (μm)	29–103	
ANDOR Ikon-L 936 CCD	2048 × 2048; cooled (i)	(ii) White beam camera; coarse energy selection via choppers
ANDOR Zyla sCMOS 4.2 Plus	2048 × 2048 (ii)	
ANDOR iStar DH712 CCD	512 × 512; gatable (iii)	(iii) Source triggered gate: one energy channel

A microchannel plate detector (MCP) developed by the University of California at Berkeley [32] utilizes neutron absorption by boron and gadolinium atoms impregnated into the MCP glass followed by the generation of secondary electrons and signal amplification within the pores of the MCP localized to a ~10 μm area. The field of view of the detector is 28 × 28 mm^2 and the detector is capable of providing a TOF spectrum for each pixel of the 2 × 2 array of Timepix readout chips (512 × 512 pixels, each 55 × 55 μm^2). The fast electronics with 320 μs readout time enables acquisition of multiple 'shutters' (maximum 1200) for each neutron pulse with individually controlled time resolution within each shutter. It can be noted that a 'shutter' is synonymous with a 'TOF range' within the time frame between two source pulses. The distance between the neutron-sensitive MCP and the front of the aluminium window of the detector box is 12 mm.

An active pixel sensor (GP2) uses the PImMS-2 CMOS [30,31]. A gadolinium sheet is used for converting neutrons to electrons which are then counted by a CMOS sensor with a pixel size of 70 μm. A number of up to 4096 times slices can be used; the timing resolution is better than 12 ns. The GP2 has four 12-bit registers per pixel which reduces the effect of saturation (or event overlap). Due to its compact design the camera can be placed close to a sample or sample environment where a small sample-detector distance is required.

The Messina optical camera box of IMAT uses a scintillator screen for neutron-to-light conversion, a 45 degree mirror, a lens to focus the light on a digital CCD or CMOS camera chip. The field-of-view ranges between 60 × 60 and 211 × 211 mm^2. The system is used for white-beam radiography and tomography measurements as well as for energy-selective applications for contrast enhancement and contrast variation, and potentially for large-field-of-view Bragg edge mapping. A range of scintillators, either ZnS/^{6}Li or Gd_2O_2S (Gadox), of different thicknesses are available. The field of view and the

spatial resolution can be adapted by changing the lens. With a 2 k × 2 k pixel camera the best spatial resolution is achieved for a field of view of 60 × 60 mm^2. It is worth mentioning that the camera has a built-in optical autofocus system [34]. Different CCD/CMOS camera modules can be mounted on the box.

The IMAT cameras can be interchanged during a user experiment, and calibrated in less than two hours. A camera support frame, with the position adjustable along the beam direction, and a 7 axis robotic manipulator arm are available to support a camera when in use. The robotic arm solution was selected based on the requirement to place and remove multiple detectors in the sample area above the SPS; it allows for maximum flexibility to accommodate future detector designs.

There will be continuous upgrades and developments of imaging cameras on IMAT, especially with regards to the active sensitive areas and the neutron detection efficiencies. Limiting factors for energy-selective measurements for the CCD and CMOS systems are the minimum field of view (limits spatial resolution) and the thickness of the scintillation screen (related to a blurring of the event determination; limits spatial resolution) and the afterglow and activation of the screens (limiting the time-of-flight determination from tens of microseconds to seconds). For IMAT a timing resolution of at least 20 microseconds is required for TOF applications. Both IMAT pixel detectors MCP and the GP2 have a potential for the active areas to be increased by tiling, i.e., by placing readout chips side by side. For instance, the current generation of the Timepix chip is three-side buttable allowing 28 × N mm configurations. Future chips will be four-side buttable by implementation of through-silicon vias. Envisaged development lines for neutron imaging cameras and detectors on IMAT are listed in Table 2.

Table 2. Envisaged future IMAT camera systems.

Camera/Detector Type	Camera/Detector Parameters		Energy-Selection
Berkeley MCP (Timepix 3)	See MCP above; sparsified readout; 10,000 time bins;	-	TOF: Triggered by source
Tiled MCP	enlarged field of view, e.g., 28 × 110 mm^2	-	Energy-dispersive
Tiled Oxford-ISIS GP2	See GP2 above; enlarged field of view, e.g., 22 × 194 mm^2	-	TOF: Triggered by source
		-	Energy-dispersive
nGEM gas electron multiplier (e.g., [[39]])			
Field of View (mm^2)	100 × 100	-	TOF: Triggered by source
Number of pixels	125 × 125	-	Energy-dispersive
Effective Pixel Size (µm)	~800		
Additional options for *Messina Optical Tomography Box*			
Gated CCD or CMOS		-	Source triggered gate: one energy channel per neutron pulse
Field of View (mm^2)	60 × 60–210 × 210		
Number of pixels	2048 × 2048		
Effective Pixel Size (µm)	29–103		
High Frame Rate Camera	10^5 frames per second; field of view e.g., ~30 × 30 mm^2	-	Source triggered: multiple energy channels per pulse
High-Resolution Camera			
Field of View (mm^2)	30 × 30	-	White beam camera; energy selection via choppers
Number of Pixels	4096 × 4096; cooled		
Effective Pixel Size (µm)	7.3		

2.3. IMAT Spectrum and Energy-Selection

The 'natural' (non-overlapping) neutron bandwidth of IMAT is 7 Å, according to Equation (2), for a source frequency of 10 Hz and a flight path of 56 m. Due to the finite opening and closing times of the 10 Hz choppers of about 3 ms, the effective bandwidth is smaller, and close to 6 Å. Figure 4 displays a single-frame IMAT spectrum (blue curve) for 10 Hz operation of the choppers, and with the choppers opening with the pulse generation. The data were collected with the monitor M5 at 49 m from the source. The wavelength band can be shifted upwards the wavelength scale at will, by dephasing

the chopper openings. For the standard IMAT experiment a range from 1 to 7 Å is usually adequate. The choppers can be run at half frequency to access the second frame, thereby doubling the effective neutron wavelength bandwidth to 12 Å (black curve in Figure 4). In this case, every other neutron pulse is removed by the choppers, hence the intensity drops by a factor of about 2. The pink curve in Figure 4 demonstrates selection of a narrow bandwidth of about 0.63 Å (FWHM) near the maximum of the flux distribution at 2.6 Å. A bandwidth selection is of interest, for example, for producing neutron images beyond the Bragg cut-off wavelength where attenuation is dominated by absorption and where crystal structure and crystal grain effects on the images are minimized. A narrow band is also used to minimize the errors being made by averaging measured attenuation coefficients in the presence of spectral beam inhomogeneities across the field of view and/or beam hardening effects for highly absorbing materials.

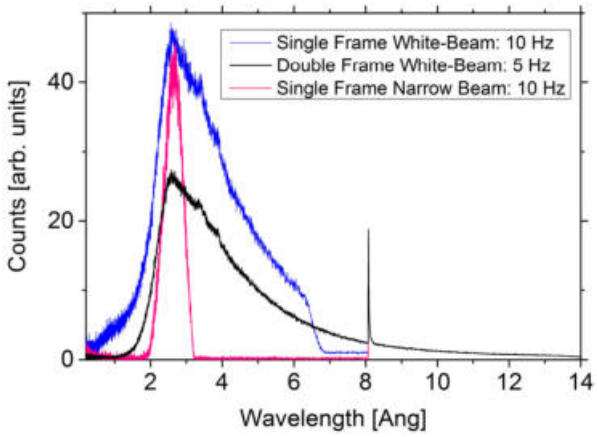

Figure 4. Beam spectra for different chopper settings, not corrected for efficiency: single-frame white-beam; narrow-bandwidth (pink) beam; double frame white-beam. The spike at 8.1 Å is the gamma pulse originating when the protons hit the target, in the absence of the T_0 chopper. Data were collected in histogram mode for neutron counts as a function of the neutron time-of-flight with a logarithmic time bin of $\Delta T/T$ = 0.001 in a range between 5 μs to 100 ms and 5 μs to 200 ms for single-frame and double frame acquisitions, respectively.

2.4. Instrument Parameters

Table 3 reviews some of the IMAT instrument and performance parameters, which were in part determined during a recent scientific commissioning period [29]. Estimated values of spatial resolutions and collections times on IMAT are given in the lower part of the table, for an L/D of 250. For Bragg edge imaging, the spatial resolution is not limited by the pixel size (e.g., 55 μm corresponding to a spatial resolution of 110 μm) but rather by the available neutrons per space-time pixel, and by the beam divergence and associated image blurring. Therefore, for IMAT experiments pixel events are almost always combined in a macro-pixel. Moreover, Bragg edge imaging requires sample thicknesses of several millimeters for obtaining significantly pronounced Bragg edge features. For example, for a 25 mm thick sample and for L/D = 250 the image blurring is 25/250 = 0.1 mm. It is obvious that collection times depend on the type of material studied, i.e., on neutron scattering lengths and structure factors.

Table 3. IMAT instrument parameters for TOF imaging. Performance parameters are taken from [29]. Estimated resolution and counting times refer to radiography (2D) and tomography (3D) experiments.

Neutron Source	10 Hz Pulsed Source		
Neutron spectrum	Cold spectrum, with a maximum at 2.6 Å; 100 × 100 mm^2 view onto the LH2-moderator @ 18 K		
Neutron transport	44 m, m = 3, straight supermirror guide with square (95 × 95 mm^2) cross section		
Single/double frame bandwidth	6 Å/12 Å		
Flight path to pinhole	46 m		
Flight path to sample	56 m (centre of sample positioning system)		
L/D	L/D: 2000, 1000, 500, 250, 125 (nominal) L/D: . . . , 1150, 510, 245, . . . (measured)		
Maximum neutron flux	3.8 10^7 n/cm^2/s (measured, for 100 × 100 mm^2 pinhole)		
Maximum field of view @ 56 m	185 × 185 mm^2		
Wavelength resolution	$\Delta\lambda/\lambda$ < 0.4% (<2 Å) (measured) $\Delta\lambda/\lambda$ < 0.8% (>2 Å) (measured)		
Spatial resolution and data collection time (ballpark numbers, for L/D ~250)			
	White-beam	Pink-beam	TOF (Bragg edge)
		$\delta\lambda/\lambda$ ~25%	$\delta\lambda/\lambda$ < 0.8%
Collection time (hours)	4–8	8–16	2–6
Spatial resolution (μm)	50 (3D)	100 (3D)	200 (2D)
Field of view (μm)	200 × 200	200 × 200	20 × 20

2.5. Infrastructure and Software

IMAT was designed and built in a way that an inexperienced user is able to operate most components safely and efficiently. Like all ISIS instruments IMAT include safety features such as a personal protection system for safe access of the experimental area, as well as an advanced motion control safety system. Most operations on IMAT can be performed remotely via a central control station (called NDXIMAT) in the IMAT cabin. A plan view of the IMAT extension building in Figure 5 indicates some of the main IMAT infrastructure points around the shielded experimental area ('IMAT blockhouse'):

- IMAT cabin: With work stations for instrument control and image analysis, and links to the ISIS data archive;
- a small chemistry/sample preparation laboratory;
- a large safe in lockable room for storing large samples, and valuable samples and objects. The room can be used for sample storage before and after irradiation, i.e., for radio-activated samples and equipment;
- an offline-testing area for sample environment, in particular for mechanical loading rigs;
- a hydraulic system to deliver 210 bar hydraulic pressure at 90 lpm flow rate to two manifold stations - one positioned at the sample area and another station at the offline-testing area.
- a services shed outside the IMAT extension for hydraulic pumps, He gas compressors for cold heads, vacuum pumps;
- an offline laser scanning area

Figure 5. Plan-view sketch of the IMAT extension building, showing the infrastructure around the IMAT blockhouse.

A 2-ton crane is available to load samples and equipment into the sample area through a power-operated roof.

Figure 6 gives an overview of the data management structure. The IBEX instrument control graphical user interface [36] runs on the NDXIMAT machine from which all instrument components, choppers, pinhole rotator, beam monitors, fast attenuator, jaws, slits, imaging cameras and sample environment are controlled. IBEX has also control of the ISIS DAE-2 data acquisition system which manages the ISIS trigger signals, records the monitor counts as a function of time of flight, and in future will readout the IMAT diffraction detectors. Figure 7 shows a screenshot of the IBEX GUI. The control of components are achieved via EPICS operator interfaces [38] but, most importantly, via command line and python scripts which enables scripting of most instrument control options.

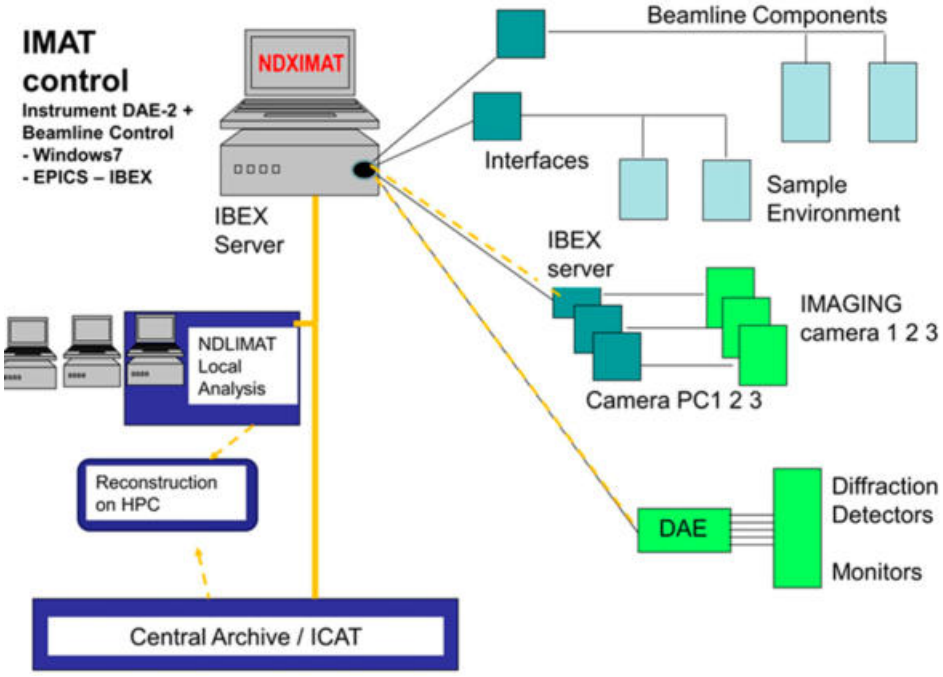

Figure 6. IMAT data management structure.

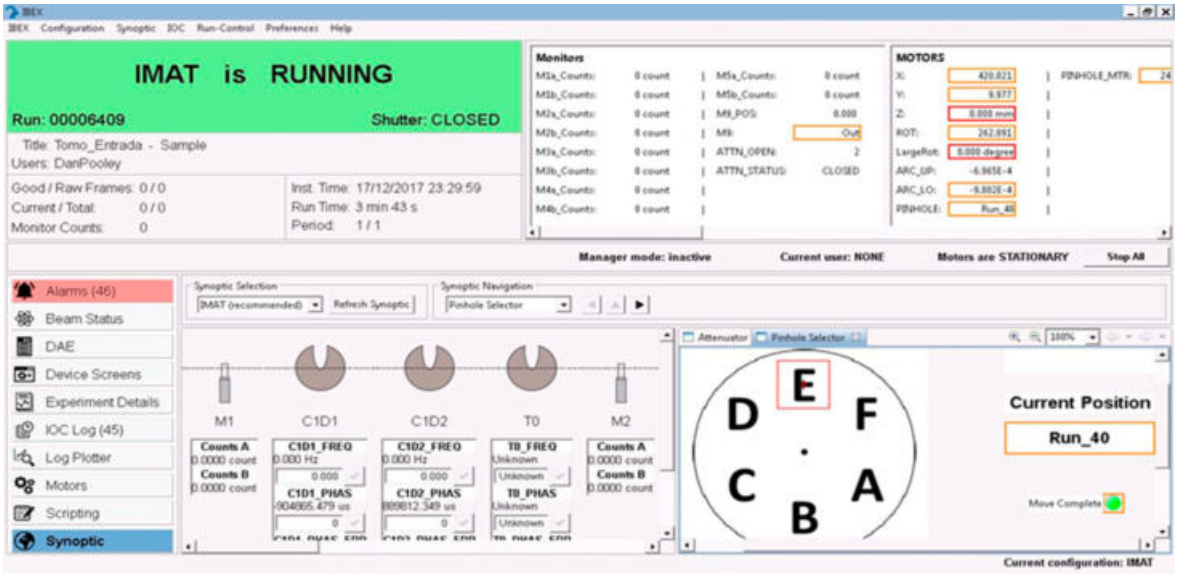

Figure 7. IBEX Graphical User Interface: IMAT instrument and camera control.

A camera/pixel detector is set-up on a dedicated camera PC, usually with its own camera GUI for stand-alone operations, for example PIXELMAN [40] in the case of the MCP, and the Messina GUI in case of the optical camera box. Remote and scripted control of the camera interface is achieved via EPICS. The image formats currently implemented are: TIF or FITS for single images; stacks of FITS for the MCP; event lists for the GP2. The filename of a single image, or the name of an image stack (for a number of rotations for tomography; a number of time bins for the MCP/GP2) has a unique run number prefix. It is envisaged that in the medium term the IMAT data will be saved and archived in NeXus [41,42] format.

Software tools for image analysis and Bragg edge mapping include BEATRIX [43], TPX_EdgeFit [44] and RITS [45]. A number of pilot projects have highlighted that IMAT needs flexible and adaptable software for the analysis of energy-dispersive data, as the analysis requirements for experiments vary. Packages for 3D reconstruction (Octopus [46]; Tomopy [47]; AstraToolbox [48]) and segmentation and volume rendering (VgStudioMax [49], Avizo [50]) of white-beam data are available for users on IMAT. Remote access to software for users will be implemented in the near future. A python-based interface for pre-processing raw images and for preparing images for various reconstruction packages is being developed within the MANTID [51] software framework. The analysis is performed either on local desktop workstations or multi-core CPU/GPU high performance clusters (HPC). In addition, efforts are made to process IMAT data with the SAVU [52,53] reconstruction pipeline. Currently, IMAT data are processed / reconstructed locally, partially using licensed packages. In the medium term, complete processing and reconstruction will be performed with freeware tools, so that users can analyze data at their home institutions. It is envisaged that HPC clusters will be required for particularly computational intensive iterative codes.

3. Demonstration of Bragg Edge Analysis on IMAT

Here we present a step-by-step description of an energy-dispersive imaging experiment on IMAT. Data collected with the MCP detector on a shrink-fitted Fe–Cu test object are used to demonstrate the data collection and image analysis procedures. The aim of the measurement on the test sample is to determine the crystalline phase and axial strain distributions of the iron and copper phases with a resolution of 200 μm.

3.1. Sample Description

The test object consisted of a solid copper cylinder of 10 mm diameter and 25 mm height shrink-fitted into a hollow ferritic iron steel cylinder of the same height but of 25 mm outer diameter with a small interference fit at the inner diameter. The shrink-fitting was achieved by cooling the copper cylinder in liquid nitrogen whilst heating the hollow iron cylinder on a hot-plate [54]. The temperature difference and extent of misfit were sufficient to allow an easy shrink-fitting of the copper cylinder into the bore. A photo and schematic of the sample is shown in Figure 10a.

3.2. Flight Path Calibration

The camera is installed in the beam path using a robotic arm, with a reproducibility of better than a millimeter. For accurate lattice spacing measurements, i.e., for strain mapping, and for studying phase transitions of crystalline samples, it is recommended that a standard sample is measured and the flight path calibrated, especially if the camera was reinstalled or moved between measurements. This will also ensure that the camera is working as expected. The flight path is determined from several Bragg edge positions using the neutron time of flight relation of Equation (1). A beryllium sample was selected for calibration because it yields a spectrum of well separated and well-defined Bragg edges in a relatively short time. Other samples for calibration used on IMAT are iron and ceria (CeO_2) powders. Figure 8a shows the Bragg edge spectrum of the beryllium sample, contained in an aluminium box, measured for about 30 min and averaged over the whole sensitive area of the MCP detector. The thickness of the Be-sample along the beam direction was 80 mm. For the flight path calibration the fitted TOF Bragg edge positions for different lattice planes (hkl) are plotted against tabulated beryllium d-spacings (and hence wavelengths) (Figure 8b). Linear regression of calibration points yields the flight path L and ΔT as fitting parameters: L = 56.35 $\pm$ 0.05 m and ΔT_0 = 1.35 $\pm$ 35 us.

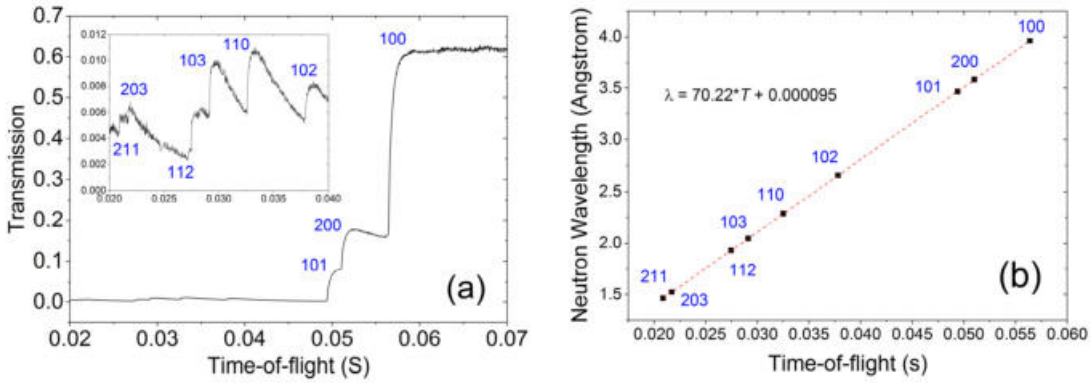

(**a**) (**b**)

Figure 8. TOF flight path calibration using a beryllium sample. (**a**) Indexed TOF spectrum for a large region of interest of the sample; (**b**) plot of the nominal Be Bragg edge positions versus measured Bragg edge positions. The slope yields the flight path; the intercept yields the TOF offset, according to Equation (1).

3.3. Data Collection

3.3.1. Sample Alignment and Camera Preparation

The sample was installed in front of the Al window of the MCP detector, with the neutron beam along the cylinder axis of the sample. In this way the Bragg edge shifts correspond to the axial strain components of the Fe and Cu sample components. The sample was mounted on a boron carbide pedestal to reduce scattering of neutrons, considering that the neutron beam is larger than the sample. The distance between the downstream end of the sample and the active sensor is 20 mm, including a 12 mm distance between the front of the Al window, a 5 mm thick boron carbide B_4C neutron shielding

plate on the front face of the MCP, and a distance of 3 mm of the sample to the B_4C shielding face. The following settings were made, in preparation of the measurements:

- The IMAT disk choppers were set to 10 Hz, and dephased by 20 ms to define a TOF range of 32–115 ms, corresponding to a wavelength band of about 2.2–8 Å. The same delay of 20 ms was set for the MCP detector (to be added to the TOFmin and TOFmax values in Table 4). The MCP system used a 10 Hz trigger signal from the choppers.
- The beam size was set to 35 × 35 mm^2 to fully illuminate the MCP active sensor.
- The pinhole was set to 40 mm diameter; i.e., the L/D was 245 [29]; the part of the sample furthest away (45 mm) from the sensor determines the best resolution of 45/245 = 180 µm.
- The expected positions of Bragg edges can be found in crystallographic databases. There are tools available to calculate Bragg edge spectra taking the structure information, and neutron absorption and neutron scattering cross sections into account e.g., [55].
- The TOF ranges and the time bins were set in the MCP detector interface (by editing ShutterValues.txt). Three MCP readouts were chosen between 32 and 115 ms, to reduce event overlap (see below) whilst avoiding having Fe and Cu Bragg edges coinciding with readout gaps. Table 4 contains calculated edge positions of copper and ferritic steel, and a list of shutters used for the experiment: three TOF ranges (shutters) with time bins of 40.96, 20.48, 40.96 µs were defined.
- M5 and the sample slits were moved out of the beam.

Table 4. Expected Bragg edge positions of Cu and Fe; lower and higher TOF boundaries of MCP shutters (in seconds) indicating the readout gaps, and spanning a total range 12–95 ms. In addition, the trigger signals and acquisition frame are delayed by 20 ms; MCP clock frequency 100 MHz/2^n with clock divider (n); time channel width (in µs); number of time bins (sum: 2612).

Calculated Bragg Edge Positions:					
(hkl) (Cu)	λ (A)	T (µs)	(hkl)(Fe)	λ (A)	T (µs)
(1 1 1)	4.174	59,465	(1 1 0)	4.051	57,710
(2 0 0)	3.615	51,500	(2 0 0)	2.865	40,815
(2 2 0)	2.556	36,410	(2 1 1)	2.339	33,320
(3 1 1)	2.180	31,060	(2 2 0)	2.026	28,860
TOFmin (s)	TOFmax (s)	n		Time bin (µs)	number of time slices
12×10^{-3}	32.68×10^{-3}	8		40.96	504
33×10^{-3}	57.68×10^{-3}	9		20.48	1205
58×10^{-3}	95×10^{-3}	8		40.96	903

The sample was visually aligned using the alignment laser and a theodolite. The sample position (x,y,z) was then fine-tuned in-situ in the neutron beam using the PIXELMAN [40] GUI of the MCP as a live display. Additionally, SPS coordinates for a sample-out measurement were visually verified.

3.3.2. Open-Beam Data and Dark Current Images

An open-beam measurement was performed for flat field normalization. The MCP settings have to be the same for the sample and open-beam runs. The open-beam collection time should be at least as long as the sample measurement. Dark current images are not required for the MCP as there is no detector dark noise for it.

3.3.3. Sample Scan

The counting time for the energy-dispersive radiography was three hours, corresponding to an accumulated proton current of 120 µA. The data acquisition for the DAE-2 and MCP was controlled by

a python script which includes the sample coordinates, exposure time (in proton current), and data folder and data filename definitions. Running the acquisition with a target proton current ensures an effective exposure time in case the neutron source trips and/or neutron pulses are vetoed by, for example, the chopper system or sample environment. With the TOF ranges and time channel widths as defined in Table 4 a stack of 2612 radiographies was collected, with each radiography belonging to a given wavelength.

For strain measurements a dataset on an unstrained ('d_0') reference sample is usually required. For the test object studied here we have used lattice parameters from the literature as reference values for the strain calculation.

3.3.4. Inspecting the Data

The MCP GUI provides a live display of the 2D radiography. An ImageJ plugin [56] is available to inspect the TOF spectra during or after the measurement. Figure 9 shows an example of a screenshot of the plugin GUI. The plugin is a useful tool for surveying a TOF stack of images; it performs, among other things, the scaling and overlap corrections, and produces and displays a transmission spectrum for a region of interest.

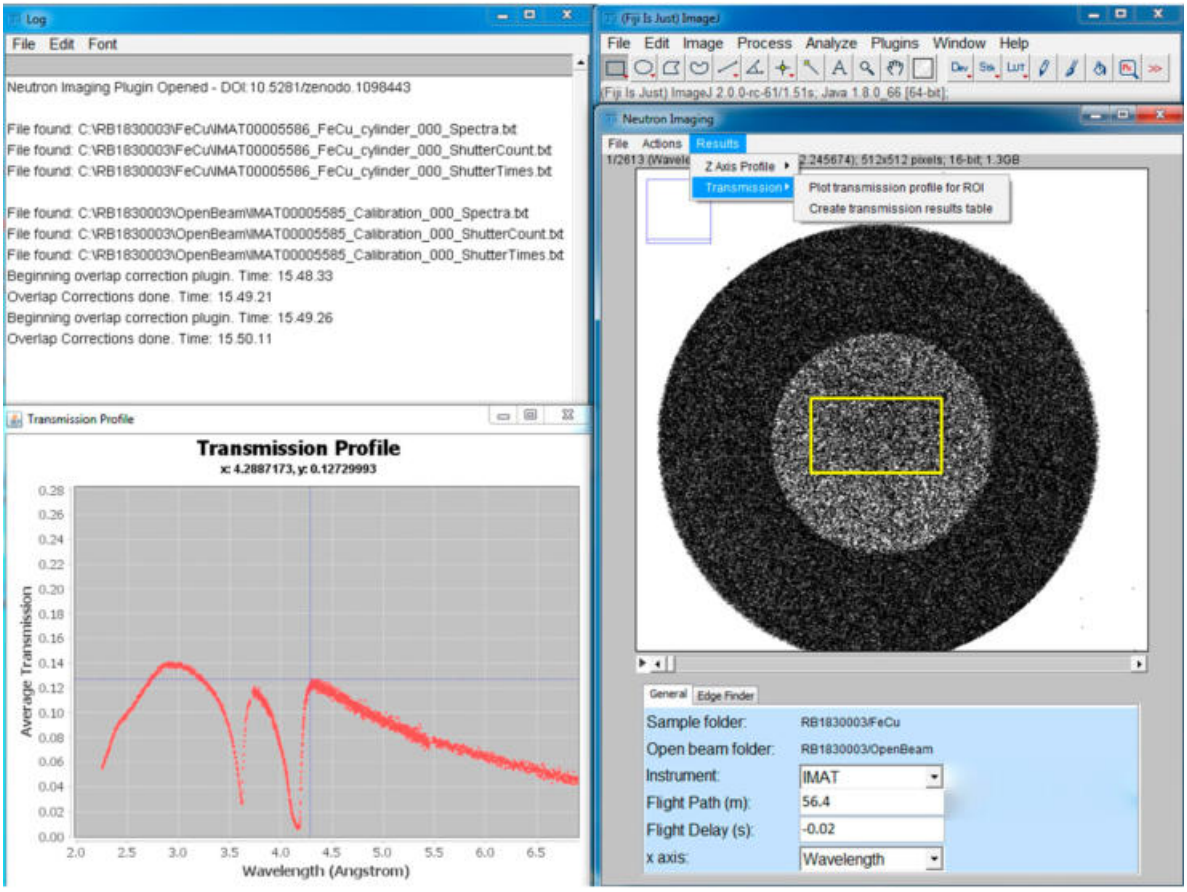

Figure 9. IMAT ImageJ plugin. The radiography on the right corresponds to a 40 µs time slice at 12 + 20 = 32 ms. On the left, a copper Bragg edge spectrum, averaged for the yellow-box selection, is displayed.

3.4. Correction Procedures

The following operations need to be considered, performed on the stacks of sample and open-beam images (consisting of 2612 individual time slices).

3.4.1. Flat Fielding

The sample data and open-beam stacks are scaled to the same number of incident neutrons, using one of the following: number of neutron pulses; beam monitor integral; an open beam area in the sample image stack; proton current. Both stacks are subjected to artifact cleaning, including a white spot filter. The sample stack is normalized, i.e., by dividing (macro space-time-) pixel by (macro space-time-) pixel, by the open-beam data to yield a stack of transmission images. Note that there is no detector dark noise for the MCP.

3.4.2. MCP Related Corrections

An event overlap correction [57] is performed to take account of the fact that the MCP can register only one neutron per pulse per TOF range (shutter). Hence, a neutron arriving late in the TOF range has a higher probability that a particular pixel is already occupied.

Furthermore, for a quantitative analysis the change of the detection efficiency of the MCP during a measurement may need to be corrected. The efficiency changes under relatively high neutron fluxes due to the ageing effects of current MCPs. Since this efficiency change is position-dependent, it induces a memory image, which can be significantly reduced with correction procedures described in [35].

Misalignment of the quad (2 × 2) Timepix readout chips causes distortions of the real shape of the sample image. The geometry of the gaps can be determined using precision phantoms, and the image distortions can be ameliorated by post-experiment image corrections [58].

3.5. Basic Image Analysis

Figure 10 illustrates a simple image analysis as performed with ImageJ. The test object, and its orientation in the neutron beam, is shown in Figure 10a. Figure 10b represents the 'white-beam' transmission image, generated by dividing the respective sums of 2612 slices from the MCP stack for the sample and open-beam data. The white beam radiography shows hardly any contrast between Fe and Cu components. Figure 10c shows a transmission image of averaged time slices 570–580, corresponding to a narrow wavelength band around 3.8 Å, which emphasizes the Cu phase. Similarly, Figure 10d shows a transmission image of averaged time slices 795–805, corresponding to a narrow wavelength band around 4.16 Å, which emphasizes the Fe phase. The selection of wavelengths to highlight one or the other phase is made based on the transmission spectra (Figure 11a) which exhibit, for instance, that the Cu cylinder becomes opaque for a wavelength of 4.16 Å. Figure 10e shows the ratio of two images: the numerator image was obtained by summing wavelength slices between 4.6 and 5.5 Å; the denominator image was obtained by summing wavelength slices between 3.15 and 3.90 Å. The resulting image in Figure 10e enhances the Fe phase. Moreover, it indicated a variation of transmission across the Fe-cylinder by about a factor 2, indicative of texture variations in the outer Fe ring. Similarly, to enhance the Cu phase a ratio-image from regions 4.3–4.4 Å and 4.15–4.17 Å was generated (Figure 10f). The wavelength ranges for generating the ratios for the Fe and Cu enhancements are indicated in Figure 11a. It should be noted that the details about which neutron energies are best to enhance a given material do not need to be known at the time of the data collection. However, care should be taken that there are no (readout) gaps in the relevant ranges of the spectra. An image analysis as shown in Figure 10 emphasizes the advantage of collecting energy-dispersive data, as it leaves a significant amount of flexibility for post-experiment data treatment, e.g., for time binning, event mode analysis and material enhancement.

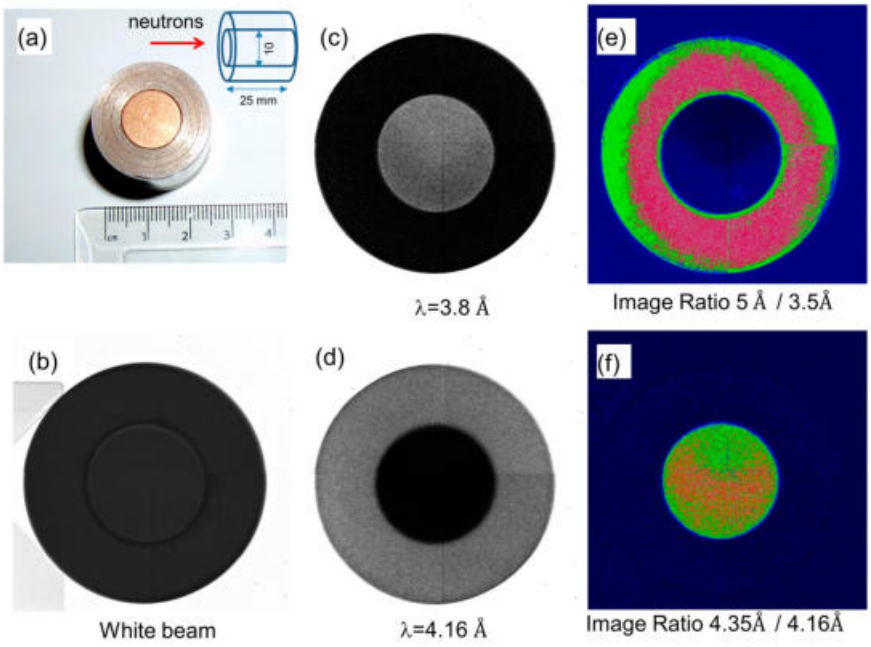

Figure 10. (**a**) Photo and sketch of the FeCu test object; (**b**) normalized white-beam radiography; (**c**,**d**) Fe and Cu enhancement by selecting suitable wavelengths; (**e**,**f**) Fe and Cu enhancement by producing image ratios from suitable wavelength ranges.

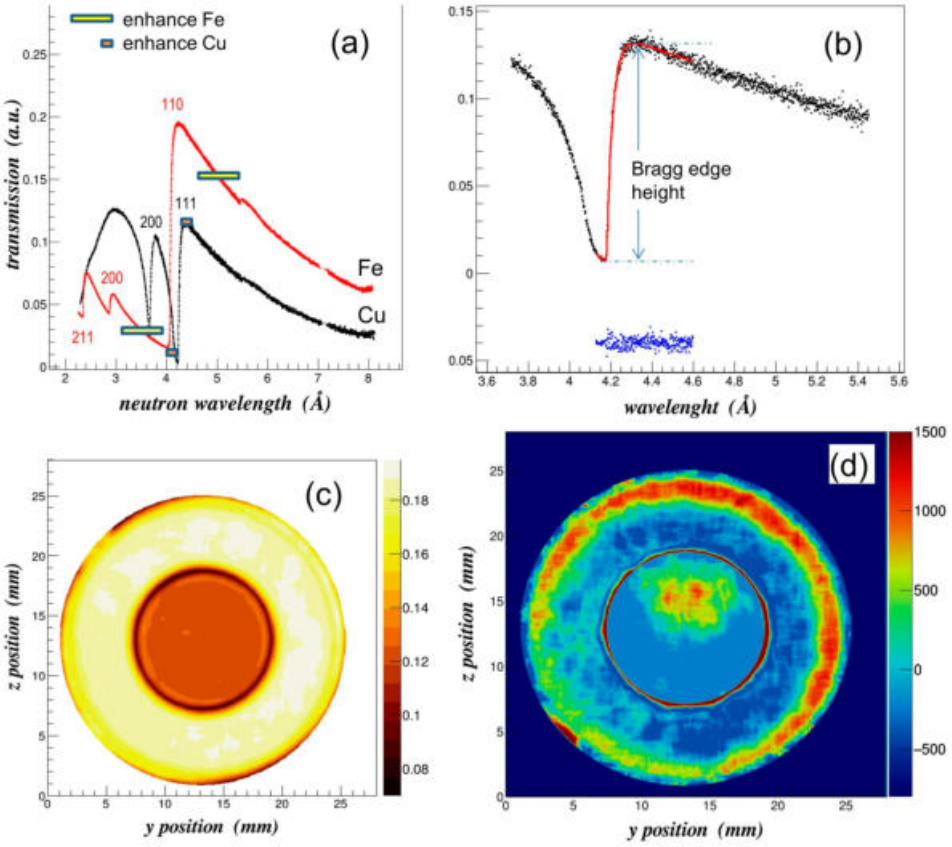

Figure 11. (**a**) Bragg edge spectra of Cu and Fe; (**b**) fit of single Bragg edge; (**c**) phase fraction map based on Bragg edge heights; (**d**) relative Bragg edge positions of Fe and Cu.

3.6. Bragg Edge Mapping

The normalized data stack was used to fit Fe and Cu Bragg edges. Spectra from 20 × 20 neighboring pixels were combined to improve the neutron statistics whilst performing a running average with a step size of 55 µm. Inspection of individual spectra of a single pixel and of regions of interest indicated that a binning of 20 × 2055 µm-pixel was adequate, corresponding to a macro-pixel size of 1.1 × 1.1 mm^2. The image analysis illustrated in Figure 11 was performed with the BEATRIX [43] neutron transmission analysis tool. Fe(110) and Cu(111) edges were fitted with the analytical function given by Santisteban [17] yielding Bragg edge positions, amplitudes and widths. The wavelength position is used to determine the residual strain

$$\varepsilon = 10^6 \frac{\lambda - \lambda_0}{\lambda_0} \quad (3)$$

with a reference value λ_0 for each hkl-Bragg edge. For strain analysis λ_0 corresponds to the Bragg edge position of the unstrained material. With the experiment geometry as indicated in Figure 10a, Equation (3) provides the thickness-averaged axial strain component in microstrain. Here we have not performed d_0 measurements for the Fe and Cu parts of the test sample, and hence we do not quantify the axial strain. Rather, values for $\lambda_0 = 2 \times d_0$ used were: 4.0538 for Fe(110) and 4.1742 for Cu(111), respectively, calculated from corresponding lattice parameters of 2.8664 Å and 3.6150 Å for Fe and Cu. Figure 11a displays the transmission spectra for the Fe and Cu phases for large regions of interest of 150 × 80 pixels. Figure 11b shows an example of the fit quality for the Cu(111) Bragg edge for a macropixel, superposed on the experimental transmission spectrum (solid black dots), with the blue dots representing the difference, observed minus calculated. Figure 11c exhibits the combined maps of the Bragg edge amplitudes of Fe(110) and Cu(111), thus representing the distribution of the two crystallographic phases. Figure 11c illustrates that by Bragg edge fitting a phase separation can be achieved. Compared to the image manipulation shown in Figure 10, a Bragg edge analysis is capable of providing quantitative results in terms of phase fractions. Figure 11d shows the deviations of the Bragg edge positions from reference values. A prominent 'tensile', axisymmetric feature in the outer part of the Fe-ring is observed, as well a non-uniform, asymmetric distribution of Bragg edge shifts for the inner Cu-plug. An interpretation of the maps in terms of axial strains and texture variation (as indicated in Figure 10e,f) will be presented elsewhere, together with neutron diffraction data. It should be noted that composition and strain maps for Fe and Cu were produced in separate analysis steps and combined afterwards for display in Figure 11c,d.

3.7. Tomographic Reconstruction

Where multiple projections are available a 3D volume data of a scalar parameter can be reconstructed using filtered-backprojection or iterative tools. From projections of, for instance, Bragg edge heights (Figure 11c) a 3D volume data can be reconstructed. A study of tomographic reconstruction algorithms of IMAT data is given in [59].

3.8. Discussion

The data collection and analysis work flow for the test object is given as example of an energy-resolving experiment on IMAT. A more thorough analysis and interpretation of the test object data for different strain components, and a comparison with diffraction data will be given elsewhere. Generally, the scan parameters, analysis procedures and software treatment need to be considered and adapted for each case, depending on the experiment's objectives and experiment conditions (e.g., at non-ambient environments) to achieve, for instance, a certain signal to noise ratio, low contrast feature discrimination or given spatial resolution.

4. Conclusions

The new IMAT instrument is currently being prepared for user operation. Neutron imaging studies on IMAT will be concerned with attenuation-based transmission measurements such as neutron radiography, neutron tomography, and energy-resolved neutron imaging. Other techniques, such as dark field imaging, will be explored in due course. The tomography and energy-resolving options will be used in a diverse range of disciplines including engineering material sciences, hydrogen-related technologies, battery research, earth science and cultural heritage.

Energy-resolved neutron imaging provides a tool for quantitative analysis of phase volume fractions and for mapping texture variations. Currently Bragg edge parameters are mapped with a spatial resolution of a few hundred microns. Analysis of the wavelength dependencies of Bragg edge parameters allows studying microstructure feature such as particle size and microstrain. TOF image analysis is in its infancy and advanced analysis algorithms and tools for reduction and analysis of energy-dispersive imaging data are developed for particular science projects. Further gains in terms of collection times and spatial resolution are to be expected with structure-constrained multi-edge and Rietveld-type analyses approaches. For scalar parameters such as phase fractions the extension from 2D to 3D imaging is straightforward as has been demonstrated by Woracek et al. [24]. Strain gradients can be mapped, while a full strain analysis via Bragg edge transmission is hampered due to the ill-posed problem for strain tomography [22]. The transmission analysis of structure-related properties including residual strains and texture will, however, benefit from the additional information from the diffraction detectors which are in the process of being installed on IMAT.

Acknowledgments: We acknowledge support throughout the IMAT project via the collaboration for scientific research at the ISIS spallation neutron source under CNR-STFC Agreement 2014–2020 (No. 3420 2014-2020). AST and JBM would like to acknowledge the collaboration between UC Berkeley and Nova Scientific, partially funded by the US Department of Energy under STTR grant Nos. DE-FG02-07ER86322, DE-FG02-08ER86353 and DE-SC0009657, and the Medipix collaboration for development of the MCP detector and Timepix readout, respectively. KW acknowledges support by the JSPS Programme, Japan, for Advancing Strategic International Networks to Accelerate the Circulation of Talented Researchers.

Author Contributions: The work performed in the IMAT instrumentation and commissioning project was performed in collaboration between all authors. W.K., T.M., D.E.P., G.B., R.R. collected and analysed the data. T.M. and A.S.T. developed the TOF data analysis codes. F.A.A., G.D.H., C.M., D.P.K. developed the instrument control user interfaces; J.K., S.K., T.-L.L., R.Z., A.R., G.V., D.M. tested the interfaces and software tools; D.E.P., J.W.L.L., A.S.T., J.B.M. developed the TOF cameras; F.A., R.P., S.T., G.S., C.V. G.G. developed the optical camera box. G.V., D.M.; R.G.A., V.F. developed correction tools and tested reconstruction algorithms; K.W. developed MCP correction procedures; F.G. helped developing the pinhole selector; D.N., ND. developed the MANTID imaging tools; W.H., J.N. produced the engineering design drawings. All authors discussed the results and commented on the manuscript at all stages.

Conflicts of Interest: The authors declare no conflict of interest.

References

1. Kockelmann, W.; Frei, G.; Lehmann, E.H.; Vontobel, P.; Santisteban, J.R. Energy-selective neutron transmission imaging at a pulsed source. *Nucl. Instrum. Meth.* **2007**, *A57*, 421–434. [CrossRef]
2. Shinohara, T.; Kai, T.; Oikawa, K.; Segawa, M.; Harada, M.; Nakatani, T.; Ooi, M.; Aizawa, K.; Sato, H.; Kamiyama, T.; et al. Final design of the energy-resolved neutron imaging system RADEN at J-PARC. *J. Phys. Conf. Ser.* **2016**, *746*, 012007. [CrossRef]
3. Strobl, M. Future prospects of imaging at spallation neutron sources. *Nucl. Instrum. Meth.* **2009**, *A604*, 646–652. [CrossRef]
4. Strobl, M.; Kardjilov, N.; Hilger, A.; Penumadu, D.; Manke, I. Advanced neutron imaging methods with a potential to benefit from pulsed sources. *Nucl. Instrum. Meth.* **2011**, *A651*, 57–61. [CrossRef]
5. Kabra, S.; Kelleher, J.; Kockelmann, W.; Gutmann, M.; Tremsin, A.S. Energy-dispersive neutron imaging and diffraction of magnetically driven twins in a Ni2MnGa single crystal magnetic shape memory alloy. *J. Phys. Conf. Ser.* **2016**, *746*, 012056. [CrossRef]

6. Tremsin, A.S.; Yau, T.Y.; Kockelmann, W. Non-destructive examination of loads in regular and self-locking Spiralock® threads through energy-resolved neutron imaging. *Strain* **2016**, *52*, 548–558. [CrossRef]
7. Sato, H.; Shiota, Y.; Morooka, S.; Todaka, Y.; Adachi, N.; Sadamatsu, S.; Oikawa, K.; Harada, M.; Zang, S.; Su, Y.; et al. Inverse pole figure mapping of bulk crystalline grains in a polycrystalline steel plate by pulsed neutron Bragg-dip transmission imaging. *J. Appl. Cryst.* **2017**, *50*, 1601–1610. [CrossRef]
8. Makowska, M.G.; Strobl, M.; Lauridsen, E.M.; Kabra, S.; Kockelmann, W.; Tremsin, A.; Frandsen, H.L.; Theil Kuhn, L. In situ time-of-flight neutron imaging of NiO–YSZ anode support reduction under influence of stress. *J. Appl. Cryst.* **2016**, *49*, 1674–1681. [CrossRef]
9. Festa, G.; Perelli Cippo, E.; Di Martino, D.; Cattaneo, R.; Senesi, R.; Andreani, C.; Schooneveld, E.; Kockelmann, W.; Rhodes, N.; Scherillo, A.; et al. Neutron resonance transmission imaging for 3D elemental mapping at the ISIS spallation neutron source. *J. Anal. At. Spectrom.* **2015**, *30*, 745–750. [CrossRef]
10. Tremsin, A.S.; Vogel, S.C.; Mocko, M.; Bourke, M.A.M.; Yuan, V.; Nelson, R.O.; Brown, D.W.; Feller, W.B. Non-destructive studies of fuel rodlets by neutron resonance absorption radiography and thermal neutron radiography. *J. Nucl. Mater.* **2013**, *440*, 633–646. [CrossRef]
11. Kai, T.; Maekawa, F.; Oshita, H.; Sato, H.; Shinohara, T.; Ooi, M.; Harada, M.; Uno, S.; Otomo, T.; Kamiyama, T.; et al. Visibility estimation for neutron resonance absorption radiography using a pulsed neutron source. *Phys. Procedia* **2013**, *43*, 111–120. [CrossRef]
12. Tremsin, A.S.; Kockelmann, W.; Pooley, D.E.; Feller, W.B. Spatially resolved remote measurement of temperature by neutron resonance absorption. *Nucl. Instrum. Meth. A* **2015**, *803*, 15–23. [CrossRef]
13. Shinohara, T.; Hiroi, K.; Su, Y.; Kai, T.; Nakatani, T.; Oikawa, K.; Segawa, M.; Hayashida, H.; Parker, J.D.; Matsumoto, Y.; et al. Polarization analysis for magnetic field imaging at RADEN in J-PARC/MLF. *J. Phys. Conf. Ser.* **2017**, *862*, 012025. [CrossRef]
14. Cereser, A.; Strobl, M.; Hall, S.A.; Steuwer, A.; Kiyanagi, Y.; Tremsin, A.S.; Knudsen, E.B.; Shinohara, T.; Willendrup, P.K.; Bastos da Silva Fanta, A.; et al. Time-of-Flight Three Dimensional Neutron Diffraction in Transmission Mode for Mapping Crystal Grain Structures. *Sci. Rep.* **2017**, *7*, 9561. [CrossRef] [PubMed]
15. Strobl, M.; Betz, B.; Harti, R.P.; Hilger, A.; Kardjilov, N.; Manke, I.; Gruenzweig, C. Wavelength-dispersive dark-field contrast: Micrometre structure resolution in neutron imaging with gratings. *J. Appl. Cryst.* **2016**, *49*, 569–573. [CrossRef]
16. Vogel, S. A Rietveld-Approach for the Analysis of Neutron Time-of-Flight Transmission Data. Ph.D. Thesis, Christian Albrechts Universität, Kiel, Germany, 2000.
17. Santisteban, J.R.; Edwards, L.; Steuwer, A.; Withers, P.J. Time-of-flight neutron transmission diffraction. *J. Appl. Crystallogr.* **2001**, *34*, 289–297. [CrossRef]
18. Santisteban, J.R.; Vicente-Alvarez, M.A.; Vizcaino, P.; Banchik, A.D.; Vogel, S.C.; Tremsin, A.S.; Vallerga, J.V.; McPhate, J.B.; Lehmann, E.; Kockelmann, W. Texture imaging of zirconium based components by total neutron cross-section experiments. *J. Nucl. Mater.* **2012**, *425*, 218–227. [CrossRef]
19. Tremsin, A.S.; Ganguly, S.; Meco, S.M.; Pardal, G.R.; Shinohara, T.; Feller, W.B. Investigation of dissimilar metal welds by energy resolved neutron imaging. *J. Appl. Cryst.* **2016**, *49*, 1130–1140. [CrossRef] [PubMed]
20. Vitucci, G.; Minniti, T.; Di Martino, D.; Musa, M.; Gori, L.; Micieli, D.; Kockelmann, W.; Watanabe, K.; Tremsin, A.S.; Gorini, G. Energy-resolved neutron tomography of an unconventional cultured pearl at a pulsed spallation source using a microchannel plate camera. *Microchem. J.* **2018**, *137*, 473–479. [CrossRef]
21. Hendriks, J.N.; Gregg, A.W.T.; Wensrich, C.M.; Tremsin, A.S.; Shinohara, T.; Meylan, M.; Kisi, E.H.; Luzin, V.; Kirsten, O. Bragg-edge elastic strain tomography for in situ systems from energy-resolved neutron transmission imaging. *Phys. Rev. Mater.* **2017**, *1*, 053802. [CrossRef]
22. Lionheart, W.R.B.; Withers, P.J. Diffraction tomography of strain. *Inverse Probl.* **2015**, *31*, 045005. [CrossRef]
23. Kardjilov, N.; Manke, I.; Hilger, A.; Williams, S.; Strobl, M.; Woracek, R.; Boin, M.; Lehmann, E.; Penumadu, D.; Banhart, J. Neutron Bragg edge mapping of weld seams. *Int. J. Mater. Res.* **2012**, *103*, 151–154. [CrossRef]
24. Woracek, R.; Penumadu, D.; Kardjilov, N.; Hilger, A.; Boin, M.; Banhart, J.; Manke, I. 3D Mapping of Crystallographic Phase Distribution using Energy-Selective Neutron Tomography. *Adv. Mater.* **2014**, *26*, 4069–4073. [CrossRef] [PubMed]
25. Minniti, T.; Kockelmann, W.; Burca, G.; Kelleher, J.F.; Kabra, S.; Zhang, S.Y.; Pooley, D.E.; Schooneveld, E.M.; Mutamba, Q.; Sykora, J.; et al. Materials analysis opportunities on the new neutron imaging facility IMAT@ISIS. *J. Instrum.* **2016**, *11*, C03014. [CrossRef]

26. Kockelmann, W.; Burca, G.; Kelleher, J.F.; Kabra, S.; Zhang, S.Y.; Rhodes, N.J.; Schooneveld, E.M.; Sykora, J.; Pooley, D.E.; Nightingale, J.B.; et al. Status of the neutron imaging and diffraction instrument IMAT. *Phys. Procedia* **2015**, *69*, 71–78. [CrossRef]
27. Strobl, M. The Scope of the Imaging Instrument Project ODIN at ESS. *Phys. Procedia* **2015**, *69*, 18–26. [CrossRef]
28. Bilheux, H.; Herwig, K.; Keener, S.; Davis, L. Overview of the conceptual design of the future VENUS neutron imaging beam line at the Spallation Neutron Source. *Phys. Procedia* **2015**, *69*, 55–59. [CrossRef]
29. Minniti, T.; Watanabe, K.; Burca, G.; Pooley, D.E.; Kockelmann, W. Characterization of the new neutron imaging and materials science facility IMAT. *Nucl. Instrum. Meth. A* **2018**, *A888*, 184–195. [CrossRef]
30. Vallance, C.; Brouard, M.; Lauer, A.; Slater, C.S.; Halford, E.; Winter, B.; King, S.J.; Lee, J.W.L.; Pooley, D.E.; Sedgwick, I.; et al. Fast sensor for time-of-flight imaging applications. *Phys. Chem. Chem. Phys.* **2014**, *16*, 383–395. [CrossRef] [PubMed]
31. Pooley, D.E.; Lee, J.W.L.; Brouard, M.; John, J.J.; Kockelmann, W.; Rhodes, N.J.; Schooneveld, E.M.; Sedgwick, I.; Turchetta, R.; Vallance, C. Development of the GP2 Detector: Modification of the PImMS CMOS Sensor for Energy-Resolved Neutron Radiography. *IEEE Trans. Nucl. Sci.* **2017**, *64*, 2970–2981. [CrossRef]
32. Tremsin, A.S.; Vallerga, J.V.; McPhate, J.B.; Siegmund, O.H.W.; Raffanti, R. High Resolution Photon Counting with MCP-Timepix Quad Parallel Readout Operating at > 1 KHz Frame Rates. *IEEE Trans. Nucl. Sci.* **2013**, *60*, 578–585. [CrossRef]
33. Parker, J.D.; Harada, M.; Hattori, K.; Iwaki, S.; Kabuki, S.; Kishimoto, Y.; Kubo, H.; Kurosawa, S.; Matsuoka, Y.; Miuchi, K.; et al. Spatial resolution of a μPIC−based neutron imaging detector. *Nucl. Instrum. Meth.* **2013**, *A726*, 155–161. [CrossRef]
34. Finocchiaro, V.; Aliotta, F.; Tresoldi, D.; Ponterio, R.C.; Vasi, C.S.; Salvato, G. The autofocusing system of the IMAT neutron camera. *Rev. Sci. Instrum.* **2013**, *84*, 093701. [CrossRef] [PubMed]
35. Watanabe, K.; Minniti, T.; Kockelmann, W.; Dalgliesh, R.; Burca, G.; Tremsin, A.S. Characterization of a neutron sensitive MCP/Timepix detector for quantitative image analysis at a pulsed neutron source. *Nucl. Instrum. Meth.* **2017**, *A861*, 55–63. [CrossRef]
36. Akeroyd, F.A.; Baker, K.V.L.; Clarke, M.J.; Holt, J.R.; Howells, G.D.; Keymer, D.P.; Löhnert, T.; Moreton-Smith, C.M.; Oram, D.E.; Potter, A.; et al. IBEX—An EPICS based control system for the ISIS pulsed neutron and muon source. In Proceedings of the International Conference on Advanced Neutron Sources (ICANS-XII), Oxford, UK, 27–31 March 2018. in press.
37. EPICS: Experimental Physics and Industrial Control System URL. Available online: http://www.aps.anl.gov/epics/ (accessed on 2 January 2018).
38. EPICS OPI. Available online: http://controlsystemstudio.org/ (accessed on 2 January 2018).
39. Uno, S.; Uchida, T.; Sekimoto, M.; Murakami, T.; Miyama, K.; Shoji, M.; Nakano, E.; Koike, T.; Morita, K.; Sato, H.; et al. Two-dimensional Neutron Detector with GEM and its Applications. *Phys. Procedia* **2012**, *26*, 142–152. [CrossRef]
40. Turecek, D.; Holy, T.; Jakubek, J.; Pospisil, S.; Vykydal, Z. Pixelman: A multi-platform data acquisition and processing software package for Medipix2, Timepix and Medipix3 detectors. *J. Instrum.* **2011**, *6*, C01046. [CrossRef]
41. Koennecke, M.; Akeroyd, F.A.; Bernstein, H.J.; Brewster, A.S.; Campbell, S.I.; Clausen, B.; Cottrell, S.; Hoffmann, J.U.; Jemian, P.R.; Maennicke, D.; et al. The NeXus data format. *J. Appl. Cryst.* **2015**, *48*, 301–305. [CrossRef] [PubMed]
42. NeXus Application De_nition NXtomo URL. Available online: http://download.nexusformat.org/sphinx/classes/applications/NXtomo.html (accessed on 2 January 2018).
43. Minniti, T. BEATRIX TOF Analysis Code. Private communication 2017.
44. Tremsin, A.S. TOF Analysis Code. Private communication 2017.
45. Sato, H.; Watanabe, K.; Kiyokawa, K.; Kiyanagi, R.; Hara, K.Y.; Kamiyama, T.; Furusaka, M.; Shinohara, T.; Kiyanagi, Y. Further improvement of the RITS code for pulsed neutron Bragg-edge transmission imaging. *Phys. Procedia* **2017**, *88*, 322–330. [CrossRef]
46. Available online: https://octopusimaging.eu/ (accessed on 2 January 2018).
47. Guersoy, D.; Carlo, F.D.; Xiao, X.; Jacobsen, C. Tomopy: A framework for the analysis of synchrotron tomographic data. *J. Synchrotron Radiat.* **2014**, *21*, 1188–1193. [CrossRef] [PubMed]

48. AstraToolbox URL. Available online: https://github.com/astra-toolbox/astra-toolbox/ (accessed on 2 January 2018).
49. Available online: https://www.volumegraphics.com/en/products/vgstudio-max.html (accessed on 2 January 2018).
50. Available online: https://www.fei.com/software/amira-avizo/ (accessed on 2 January 2018).
51. Mantid 2015 Manipulation and Analysis Toolkit for Instrument Data. Mantid Project. Available online: http://dx.doi.org/10.5286/SOFTWARE/MANTID3.5 (accessed on 2 January 2018).
52. Savu: Tomography Reconstructon Pipeline. Available online: https://github.com/DiamondLightSource/Savu (accessed on 2 January 2018).
53. Atwood, R.C.; Bodey, A.J.; Price, S.W.T.; Basham, M.; Drakopoulos, M. A high-throughput system for high-quality tomographic reconstruction of large datasets at Diamond Light Source. *Philos. Trans. R. Soc. A* **2015**, *373*, 20140398. [CrossRef] [PubMed]
54. Steuwer, A.; Withers, P.J.; Santisteban, J.R.; Edwards, L. Using pulsed neutron transmission for crystalline phase imaging and analysis. *J. Appl. Phys.* **2005**, *97*, 074903. [CrossRef]
55. Boin, M. NXS: A program library for neutron cross section calculations. *J. Appl. Crystallogr.* **2012**, *45*, 603–607. [CrossRef]
56. Burca, G.; Kelleher, J.; Peacock, A.; Hayes, M.; Deliry, P. An integrated tool for Bragg Edge analysis at ISIS. In Proceedings of the NEUWAVE-8 Workshop, Abingdon UK, 12–15 June 2016.
57. Tremsin, A.S.; Vallerga, J.V.; McPhate, J.B.; Siegmund, O.H.W. Optimization of Timepix count rate capabilities for the applications with a periodic input signal. *J. Instrum.* **2014**, *9*, C05026. [CrossRef]
58. Vitucci, G.; Minniti, T.; Tremsin, A.S.; Kockelmann, W.; Gorini, G. Investigation of image distortion due to MCP electronic readout misalignment and correction via customized GUI application. *J. Instrum.* **2018**. under review.
59. Micieli, D.; Minniti, T.; Formoso, V.; Kockelmann, W.; Gorini, G. A comparative study of reconstruction methods applied to neutron tomography. *J. Instrum.* **2017**. under review.

Paper II

Microchemical Journal 137 (2018) 473–479

Contents lists available at ScienceDirect

Microchemical Journal

journal homepage: www.elsevier.com/locate/microc

Energy-resolved neutron tomography of an unconventional cultured pearl at a pulsed spallation source using a microchannel plate camera

G. Vitucci [a,*], T. Minniti [b], D. Di Martino [a], M. Musa [c], L. Gori [c], D. Micieli [d], W. Kockelmann [b], K. Watanabe [e], A.S. Tremsin [f], G. Gorini [a]

[a] University of Milano Bicocca, Dept. Phys., 20126 Milan, Italy
[b] STFC-Rutherford Appleton Laboratory, ISIS Facility, Harwell OX11 0QX, UK
[c] GECI – Gemological Education Certification Institute, Milan, Italy
[d] Dip. di Fisica, Università della Calabria, via Pietro Bucci, 87036 Arcavacata di Rende, (Cosenza), Italy
[e] Nuclear Measurement Engineering Group, Nagoya University, Nagoya, 464-8603, Japan
[f] University of California at Berkeley, Space Science Laboratory, CA 94720 Berkeley, USA

ARTICLE INFO

Article history:
Received 31 August 2017
Received in revised form 29 November 2017
Accepted 5 December 2017
Available online 06 December 2017

Keywords:
Microchannel plate
Neutron imaging detector
Energy resolved imaging
Neutron phase mapping
Cultured pearl

ABSTRACT

A non-destructive neutron analysis technique performed at the IMAT beamline of the STFC (Science and Technology Facility Council), UK, is presented. In this experiment, neutrons of different energy have been exploited to obtain a tomographic reconstruction of a biomineralic sample, more specifically a cultured pearl, by using a time-resolving pixel camera, the MicroChannel Plate (MCP) detector, utilizing an array of 2 × 2 Timepix readout chips. The MCP camera is capable of energy-resolved two-dimensional mapping of neutron transmission with a spatial resolution of ~55 μm. By using a Simultaneous Iterative Reconstruction Technique (SIRT), virtual sections of the internal part of the sample have been created, thus revealing several features inside its bulk. The crystallographic phase map via Bragg edge analysis, showing a phase fraction distribution on the entire specimen, has been generated as well. Finally, 3D volume rendering of the pearl is presented.

1. Introduction

Neutron-based tomography is a non-destructive analysis technique with several advantages, such as the ability to distinguish isotopes of the same element, the high sensitivity to hydrogen and the penetration capability towards bulky materials.

The experiment described in this paper has been performed at the Imaging and Materials Science & Engineering (IMAT) beamline operating at the ISIS spallation neutron source (UK). This instrument is able to operate energy-selective neutron imaging, exploiting the time-of-flight (TOF) analysis technique enabled by the accelerator-based pulsed neutron source located in the research center [1]. The device used for the energy-dispersive neutron imaging setup was a MicroChannel Plate (MCP) neutron counting detector.

The MCP detector developed at the University of California at Berkeley in collaboration with Nova Scientific [2] is a novel neutron camera capable to perform energy-dispersive neutron radiographies and tomographies. The neutron conversion into electrons in the detector is performed by an MCP doped with ^{10}B atoms (8 μm pores on 11 μm centers). The charged particles produced in the MCP induce an electronic avalanche resulting in 10^4–10^5 electrons which are collected by the Timepix array, a pixel readout chip developed at CERN [3]. The crucial feature of this chip is the possibility to operate in "event timing" mode, enabling time-tagging each detected neutron and thus determining its energy by the time of flight technique at a pulsed neutron source. At present, the detector has a 28 × 28 mm^2 active area, with 55 μm pixel size [4].

Several experiments have been carried out in the past years on inorganic samples [5–6], demonstrating the advantages of the TOF transmission imaging technique. In this paper we show how the field of cultural heritage can take a huge advantage from this kind of non-destructive (ND) analysis, because of the rarity and non-repeatability of the specimens studied, as well as their complex bulk microstructure.

This paper focuses on the analysis of an organic sample, more specifically on a cultured pearl, by means of time-resolved neutron tomography.

* Corresponding author at: Dipartimento di Fisica "G. Occhialini", Piazza della Scienza 3, - 20126 Milano, – Italy.
E-mail address: g.vitucci@campus.unimib.it (G. Vitucci).

https://doi.org/10.1016/j.microc.2017.12.002
0026-265X/

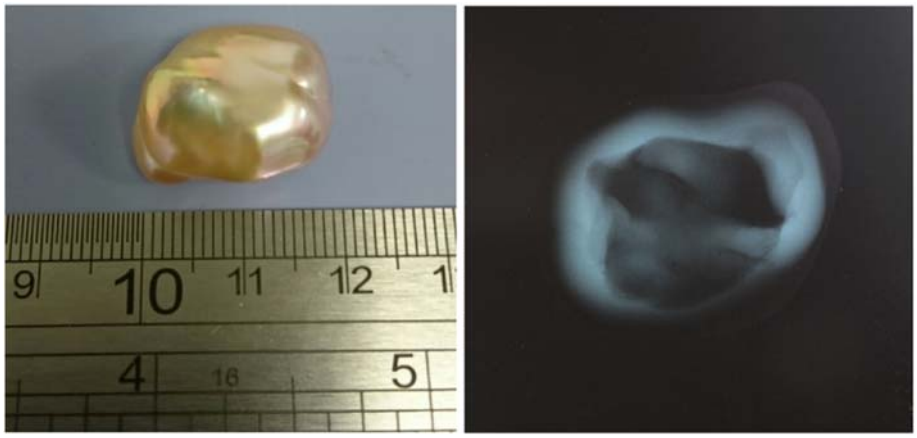

Fig. 1. Left: image of the study-case pearl. Right: X-ray radiography of the pearl.

2. Material and methods

2.1. Pearl description

During their evolution, molluscs have developed an external calcified structure, the *shell*, to support and protect their soft bodies. In the natural environment pearls are generated by accidental events, involving the activation of the same biogenic mechanisms responsible for the shell creation, but inside the living molluscs tissues. For this reason, natural pearls are rare objects, characterized by very complex biogenic structures in which the inorganic component, calcium carbonate, accounts for about 95%–99% of weight and the remaining 1% to 5% represent an organic matrix [7].

The beauty of pearls is correlated to surface features, for example the color, the luster, or the overtone; all these properties are due to the biomineralic structure of pearls. In natural pearl the calcium carbonate, constituting the inorganic component, presents two different polymorphs: a calcite phase with prismatic habitus in the inner part of the pearl, while the external area, called *nacre*, is made by an aragonite phase crystallized in flat tablets arranged in a "brick-wall" structures [8], able to interact with the light and determine the iridescent aspect of the pearl surface. It must be highlighted that all the mineral characteristics of inorganic component, like the phase, the shape, the dimension and the orientation of crystals, are self-assembled and strongly controlled by the proteins constituting the biological matrix. The nacreous aragonite tablets in fact are all iso-orientated and isometric crystals, with parallel c-axis [9].

Pearls are very important for the jewelry industry and, whereas the natural ones are rare, since the beginnings of 1900s the pearls availability started to grow by means of a culturing process which allowed the marketing of large quantities of pearls at a lower cost.

Today the culturing techniques are very sophisticated, therefore it has become difficult to distinguish between cultured and natural pearls, even though it is an essential requirement for the market [10]. In this frame, we proposed the study and characterization of pearls of different size and shapes with a novel approach, that is a non-destructive neutron analysis technique. Among the set of samples studied, in this paper we present the results obtained with an atypical-bead cultured pearl (Fig. 1). The main gemological properties of the pearl are reported in Table 1. This particular type of pearl, commercially named "soufflé", represents one of the strange types of culturing experiments, consequently of the innovative material used as nucleus. In recent years in fact, there have been many attempts to use alternative pearls and shell materials as nuclei. This includes different types of shells, bironite, laminated/powdered shell, freshwater cultured pearls and even natural pearls [11–13].

The peculiar method used to produce soufflé pearls, was intended as an intermediary step to growing large round bead cultured pearls, but the outcome resulted in very large baroque cultured pearls. The innovation consists in the use of a hydrophilic and expansible material as nucleus, from cheaper dried mud ball to more complex organic nuclei which have similar properties to super absorbent polymer spheres [13].

In this process, after a smaller cultured pearl is harvested, the hydrophilic bead is inserted into the now vacant pearl sac. Placed back in the water the bead begins to grow. As the nucleus absorbs water it expands the pearl sac in the process, determining the size and the shape of pearl [12].

At the end of pearl generation process the nucleus could be degraded or not. In the first case the pearl drilling allows the water and organic residue to come out. In the case of more complex bead, the observation of some residue inside the pearl could be possible by means of X-ray imaging, also after drilling [12]. Normally a part of the decomposed bead sediments in layers on the first nacre structure. The pearl for this study-case is not drilled.

In order to have a basis for comparison, we first acquired an X-ray 2D image of the pearl (Fig. 1, right), with a classical gemological instrument. The analysis revealed a large vacuum core and highly irregular morphology, while further details were not easily recognizable. We then proceeded with the neutron tomography.

2.2. Neutron imaging setup

The MCP detector is capable to detect the transmitted neutron intensity behind the specimen as a function of neutron time-of-flight (TOF) or energy, since the flight path is a known parameter. The resulting pattern, normalized for the incident neutron intensity, maps the wavelength dependence of the material attenuation coefficient, which can be used to recover important information about the constituents of the sample.

Table 1
Gemological properties of the pearl.

Species and variety	Souffle-bead cultured pearl
Environmental	Freshwater
Shape	Baroque
Measurements	16.20 × 20.45 × 11.05 mm
Weight	22.58 ct
Drilling	None
Body color	Orange
Overtone	Rosee

The electronic readout of the Timepix, is constituted by a matrix of pixels, each of which has a 14 bit register able to store time of event arrival relative to the external trigger (timing of the neutron pulse in our experiments), when operating in "event timing" mode. The data acquisition time, or shutter period, can be arbitrarily set inside the time frame of a single neutron pulse generated by the source operating at 10 Hz frequency. At the end of each shutter period, data must be transferred from the Timepix to the data processing unit, based on a field-programmable gate array (FPGA). This process requires 320 μs to be completed and during this dead time, no further data can be acquired. Only one event per pixel per shutter is allowed for that generation of electronics. Therefore, these shutter periods must be carefully arranged in case of relatively high neutron flux to avoid event overlaps. That is the case for the IMAT instrument, where neutron flux is higher than 10^7 neutrons/cm^2/s. In the case of a high number of incoming neutron events, the events arriving later in the acquisition shutter period have lower probability to be detected as some pixels are already occupied by previous events. This phenomenon has been defined as "overlap effect" and described by Tremsin et al. in [14]. Such effect can be mitigated by decreasing the acquisition time, in other words the occupation probability per pixel per period. In this case, a greater number of shutter periods must be set in order to cover the whole pulse time frame, thus introducing remarkable gaps into the spectrum. A compromise must be taken between the number and the duration of the shutter periods.

Since the principal element of the sample was known to be aragonite, as shown in [7], the start and the end times of each shutter period were chosen in order to avoid the main Bragg edges of aragonite coinciding with the readout gaps. The information about the Bragg edges of aragonite was taken from the **ICSD** (the Inorganic Crystal Structure Database [15]), in which the crystallographic d-spacings of aragonite are reported. Taking into account the wavelength of the incoming radiation and the total flight path at IMAT, the most intense Bragg edges were expected to be generated by neutrons with TOF in between 55 ms and 80 ms. More details about the chosen shutter periods are shown in Table 2.

In [14], a procedure has been demonstrated to correct for the "overlap effect", with an important constraint. In fact, such a method can only be used when transmission data has been generated by neutron pulses with periodical and constant shape. Being this the case of IMAT beamline, the procedure has been successfully applied during post-processing operation via software to all the collected data sets.

2.3. Experimental setup

The sample was wrapped in an aluminum foil of 11 μm thickness to permit an easy manipulation of the specimen and allowing at the same time the radiography with neutrons, as aluminum is nearly transparent for neutrons (>99.9% transmission for such thin foil).

After that, the pearl was placed on a rotation stage (Fig. 2). The specimen to camera distance was 15 mm. With a beam collimation ratio L/D of 250 the geometric unsharpness was 60 μm with an effective neutron flux of about 5.9×10^6 n/cm^2/s. A set of 450 projections in the angular range 0°–180°, to fulfill the Nyquist-Shannon sampling theorem, were acquired within 315 s as exposition time. Moreover, a stack of six flat field images (three before and three after the tomography scan) with the same acquisition time were collected for normalization purposes.

Table 2
Shutter periods of the TIMEPIX. Start and end points are intended with respect to the external trigger of the neutron source. The IMAT beamline is located at ISIS Target Station 2 (TS2), where pulse repetition rate is 10 Hz.

Shutter period #	Start [ms]	End [ms]
1	10.00	24.68
2	25.00	47.68
3	48.00	95.00

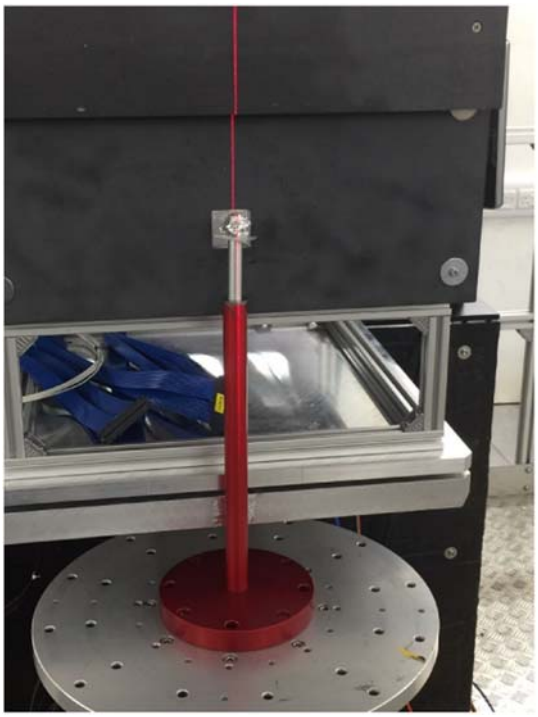

Fig. 2. Experiment setup. The pearl is placed on the rotating platform, in front of the MCP detector window.

With these settings, a total amount of about 36 h was required for the collection of an energy-dispersive tomography.

2.4. Tomographic reconstruction

The 450 projections have been corrected after the acquisition for the overlap effect.

We took into account the projections given by the complete spectrum of the transmitted neutrons in order to increase the statistics and obtain the neatest image reconstruction possible. To do this, we summed the projections with different energies for each angle-view. The flat-field correction was performed on the resulting dataset by simply dividing each projection by the average of the open beam images. Dead-pixels and gamma spots were removed from the normalized projections by using a median filter. The misalignment of the rotation axis with respect to the vertical detector axis and the defective pixels in the detector lead to reconstruction artifacts that appear in the reconstructed images as concentric rings and small circles, respectively. In order to avoid the artifacts, we applied to the dataset a ring removal filter based on combined wavelet and Fourier analysis [16], and determined the center of rotation. Both steps were performed in the MATLAB [17] framework. The tomographic reconstruction was finally performed by means of the Simultaneous Iterative Reconstruction Technique (SIRT) [18] implemented in the ASTRA TOOLBOX [19], an open source MATLAB and Python toolbox for 2D and 3D tomographic reconstruction.

3. Results and discussions

3.1. Virtual sections

In Fig. 3, we report a selection of six different virtual sections out of about 200 images obtained by the tomographic reconstruction. In these virtual sections the brightest regions represent the ones with higher neutron absorption and the darkest regions relate to voids or zones with lower neutron absorption. In our case, due to the biological nature of the sample, the brightest parts could be reliably associated

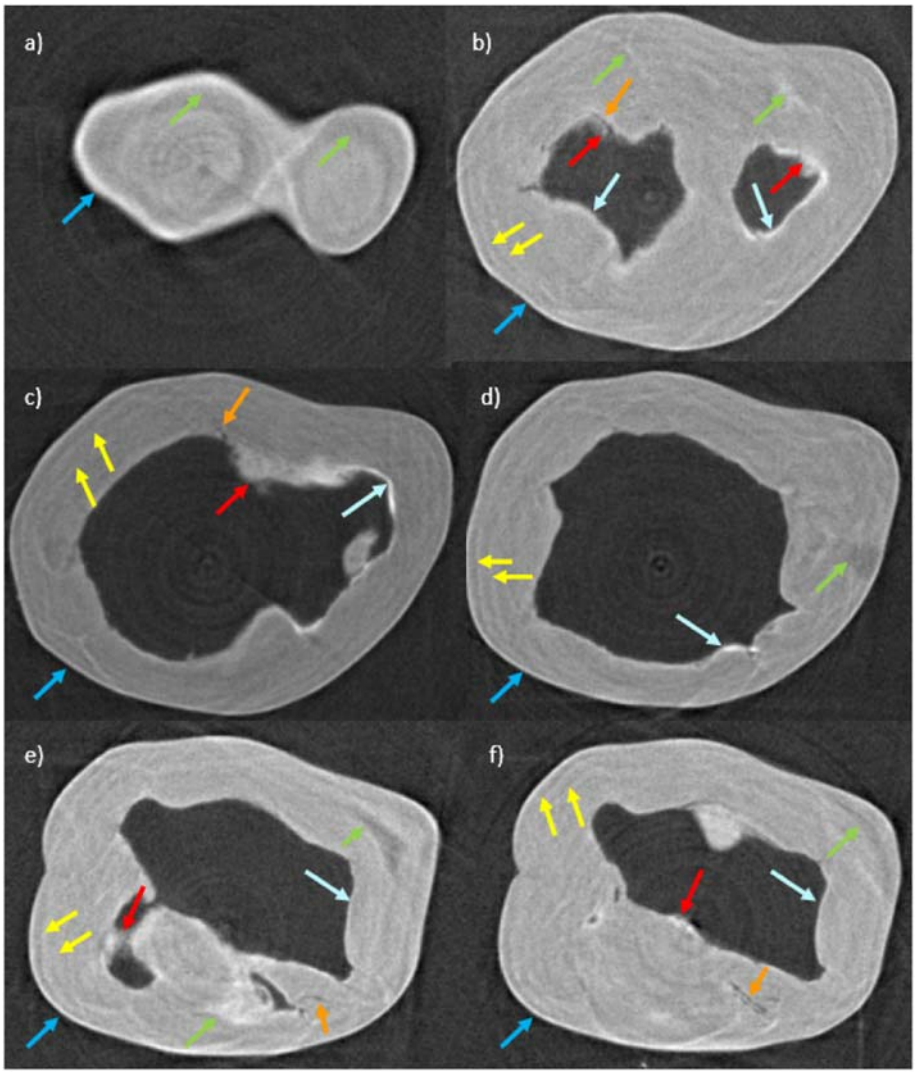

Fig. 3. a)–f) COLOR. Selection of six different virtual sections within the tomographic reconstruction. Many details of the pearl structures are evident. A full description is provided in the text.

with organic components of the pearl (maybe conchiolin fibres, a protein belonging to the group of keratins, tissue residues or other hydrogen containing compounds). As a general note, we noticed a recurrent artifact in our images, a pattern of concentric rings, that was supposed to be totally removed after the application of the ring removal filter during the tomographic reconstruction process. These structures were obviously not related to any real feature and have not been considered. The virtual sections, like any tomographic reconstruction, are taken at different positions or "height" of the sample. Our sequence from a) to f) follows a side of the pearl starting from the external part, towards the inner part.

In Fig. 3a) a section with a smaller area is visible, due to the external region investigated. Since our pearl has a very irregular morphology, in fact it has baroque shape, this virtual section reflects a sort of intersection of a bilobated structure. The area seems to be surrounded by a brighter part, probably an organic layer, which is visible in all the images a)–f) (marked by blue arrows). The area is not homogeneous, as evident in some parts highlighted by green arrows.

Fig. 3b) displays a virtual section towards the inner part of the pearl. Two voids are evident, again related to the bilobated nature of the sample. The voids contour is not regular nor clear. With light blue arrows we pointed out a sort of bright organic-rich rim, probably related to organic layers (either the ones from which the biogenetic mechanism of pearl production starts and/or the tissues deriving from the host mollusc). Moreover, some blurred parts (see red arrows) are organic-rich regions and may be related to remnants of a "soufflè" bead after degradation, or to the inhomogeneity in the first organic layer followed by aragonite platelets in a brick-like arrangement. Interestingly, we marked by yellow arrows some organic layers related to the pearl-formation process (concentric but not regular), mainly in the external part. The same is true also for the following virtual sections (again highlighted by yellow arrows). Finally, a fissure like structure is identified by an orange arrow.

Fig. 3c) exhibits a large central void, since we are approaching the central part of the pearl. Yet, a tomographic reconstruction provides a real size of the structure: we thus could derive a minimum nacre thickness of about 1.43 mm. Again, a red arrow indicates a very irregular contour zone, while an orange arrow identifies a fissure like structure.

Fig. 3d) has the most regular inner central void, with a rim (see light blue arrow). However, some irregular structures appear in the nacre (see green arrow) and organic-rich layers due to the pearl-formation process are still visible (see yellow lines).

Fig. 3e) displays a very inhomogeneous inner part: the central void is again displaying features of the very complex structure of this pearl, and of the bilobated nature (one central void, and other smaller voids too, or fissures – see orange arrow). Ring-like structures (yellow arrows), internal rim (light blue arrow), organic rich parts and bumps (red and green arrows) are evident.

Finally, Fig. 3f) exhibits again organic layering (see yellow arrows), an inner rim (light blue arrow), some bumps (see green arrow) and a fissure-like structure (see orange arrow). No rigid and regular bead was visible in any of the virtual sections, the core presenting mainly voids. Yet, we cannot exclude the presence of any compound in the inner regions, since it is reported that liquid/gaseous compounds can exit a soufflé pearl when drilled [12]. The neutron tomography has thus revealed a considerable amount of details of this baroque shaped pearl, very useful for the gemologists in the study of this kind of pearls. One third of the virtual slices obtained after the tomographic reconstruction was used to produce a movie, in order to clearly return the images of the whole pearl, section by section (see supplementary materials).

3.2. Energy-selective analysis

The characterization of the neutron transmission pattern versus the neutron wavelength has been performed on a separate set of radiographies collected for 4 h of radiation exposure on the specimen, in order to obtain good neutron statistics. Further, 4 h have been spent for the flat field radiography, for normalization purposes, which removes the features related to the beam spectrum and detector non-uniformities.

In Fig. 4 the Region Of Interest (ROI) related to both the center of the pearl and its external part is shown. When the central part is considered, the neutron beam is mostly perpendicular to the pearl organic layers.

The transmission pattern of the pearl core shows that the Bragg edges of aragonite, the most predominant phase of the nacre (over 95% by volume as told in (7)), related to the (201) plane (wavelength $\lambda = 5.40$ Å) is clearly visible, together with the one related to the (210) ($\lambda = 4.96$ Å).

By contrast, when the external ROI is considered, an increment of the intensity of a Bragg edge at different wavelengths is noticeable. A clear example is the increase of the mean transmittance at $\lambda = 3.95$ Å (122) and $\lambda = 2.34$ Å (0 2 6) with respect to the previous curve.

In the outer shell, the strong Bragg edge is smeared out. Instead of well-defined Bragg edges there is a broad hump in the transmission spectrum between 4.50 Å and 6.50 Å. This may be explained by the

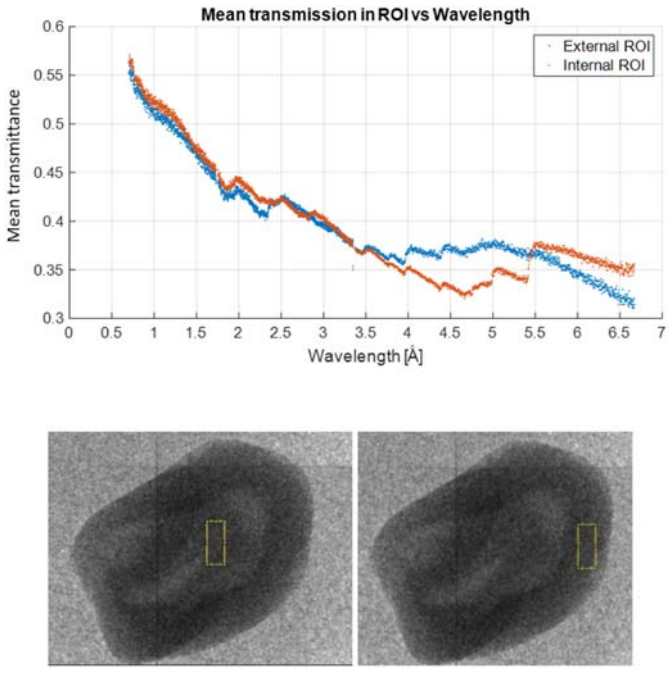

Fig. 4. COLOR. TOP: Neutron transmission spectra containing Bragg edges for both internal and external ROI of the pearl. BOTTOM: Internal and external ROI, corresponding to the core and the shell of the pearl.

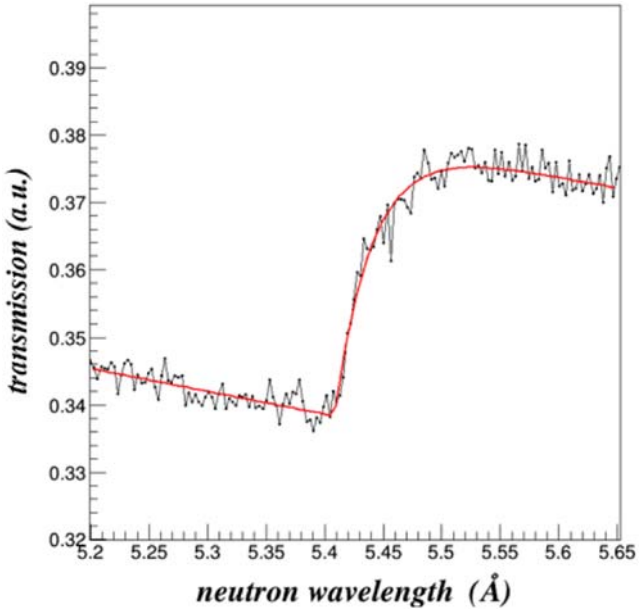

Fig. 5. Example of a Bragg edge fit for the main aragonite Bragg edge at 5.40 Å.

fact that scattering is redistributed, which indicates the presence of a preferred isoorientation of the crystallites. This is determined by the nacre platelets, confirming the aragonitic "brick-wall" structure of the nacres textures, as presented by Chateigner et al. [8].

The interpretation is related only to the ROI selected in the lower part of Fig. 4. On the other hand, the transmission patterns shown in the upper part of the same figure are detected in each pixel of the neutron counting detector. This enables the evaluation of the main Bragg edge intensity at 5.40 Å across the entire specimen with a spatial resolution of about the pixel size, i.e. 55 μm. Furthermore, such BE intensity is proportional to the aragonite phase amount across the sample.

A dedicated C++ program was developed in the data analysis framework ROOT [20], to take account of the spectral analysis of a large number of 512 × 512 pixels. Such framework is designed for storing and analyzing petabytes of data in an efficient way and

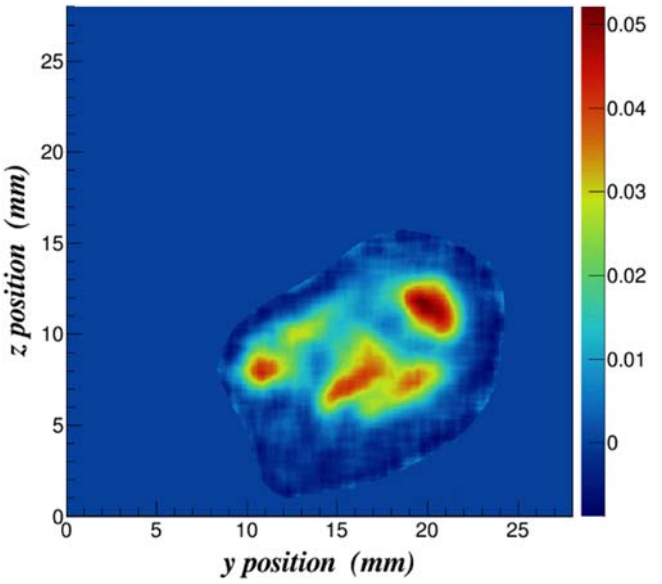

Fig. 6. COLOR. 2D map for the main aragonite Bragg edge intensities at 5.40 Å. Such map is proportional to the aragonite phase amount across the specimen.

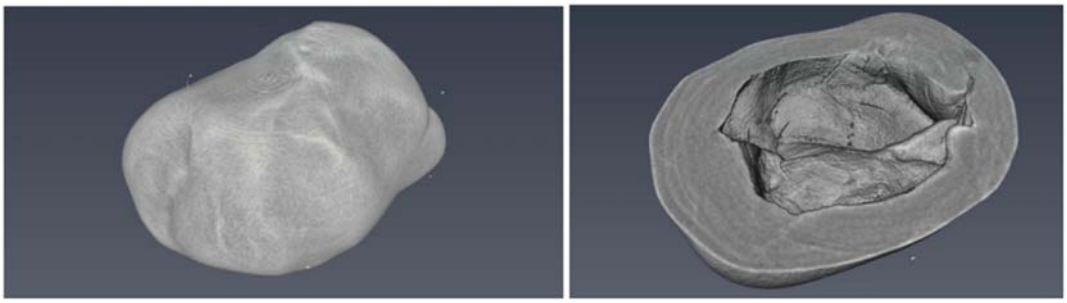

Fig. 7. Volume rendering of the pearl. Left: global view. Right: cut view. Here the empty core is clearly visible.

therefore suitable for such type of data analysis. For each pixel, a Bragg edge was fitted using the three-step procedure reported in [21]. An example of the fitting quality for a pixel within the specimen is reported in Fig. 5.

The intensity of the Bragg edge was extracted by the difference in the transmission values after and before the edge. The recursive application of the same fitting procedure, for all pixels, enables the generation of a 2D map of the Bragg edge amplitude reported in Fig. 6 and therefore provides further information about the aragonite phase distribution within the specimen [22]. In this figure, we followed for x and y axis the conventional direction used for the sample positioner system (SPS) available on the IMAT instrument. In fact, the beam direction, according to this convention, is along the x-axis. The color scale of the figure reflects the amplitude of the analyzed Bragg edge, showing that the family of planes related to the Bragg Edge at 5.40 Å of the aragonite phase is more concentrated in the central ROI, while it is less present in the outer ROI. This confirms the observations obtained with the 1D data analysis of Fig. 4.

3.3. 3D volume reconstruction

For visualization and analysis purposes, the reconstructed slices were loaded into the Amira-Avizo 3D software [23]. The volume rendering of the pearl is shown in Fig. 7. The vertical cut shown in the right panel of the same figure clearly shows that the core is either empty or filled with a material different to the one constituting the pearl nacre. This volume rendering confirms the "soufflé" structure of the pearl.

4. Conclusions

In this work, we explored the inner morphology of a baroque-shaped soufflé pearl. This very complex sample was very suitable to demonstrate the potential of energy-selective neutron imaging on biological samples. The tomographic reconstruction of a pearl showed numerous features of the pearl inside its bulk and allowed the 3D volume rendering, exhibiting an empty core, characteristic of the "soufflé" pearls. Many other details could be used by gemologists to infer the pearl-growing process for this pearl, in a completely non-destructive way. Moreover, the phase mapping of aragonite permitted the visualization of its crystallographic orientation inside the specimen and the study of its microstructural properties. Yet, only an energy-selective technique could discriminate between the presence of different phases and localize them in the inner part of this kind of specimen. Further studies, including phase mapping related to other phases (such as calcite) constituting the pearl and the reconstruction at different energies will be conducted in the future to obtain a more complete and global description of such a biological specimen.

Supplementary data to this article can be found online at https://doi.org/10.1016/j.microc.2017.12.002.

Acknowledgments

The CNR-STFC agreement 2014–2020 (No. 3420 2014–2020) concerning collaboration in scientific research at the ISIS Spallation Neutron Source is gratefully acknowledged.

References

[1] Materials analysis opportunities on the new neutron imaging facility IMAT@ISIS, T. Minniti, W. Kockelmann, G. Burca, J.F. Kelleher, S. Kabra, S.Y. Zhang, D.E. Pooley, E.M. Schooneveld, Q. Mutamba, J. Sykora, N.J. Rhodes, F.M. Pouzols, J.B. Nightingale, F. Aliotta, L.M. Bonaccorsi, R. Ponterio, G. Salvato, S. Trusso, C. Vasi, A.S. Tremsin, G. Gorini, J. Instrum. 11 (March 2016)https://doi.org/10.1088/1748-0221/11/03/C03014.
[2] A.S. Tremsin, J.B. McPhate, J.V. Vallerga, O.H.W. Siegmund, J.S. Hull, W.B. Feller, E. Lehmann, Detection efficiency, spatial and timing resolution of thermal and cold neutron counting MCP detectors, Nucl. Instrum. Methods Phys. Res., Sect. A 604 (2009) 140–143, https://doi.org/10.1016/j.nima.2009.01.041.
[3] X. Llopart, R. Ballabriga, M. Campbell, L. Tlustos, W. Wong, Timepix, a 65k programmable pixel readout chip for arrival time, energy and/or photon counting measurements, Nuclear Instruments and Methods in Physics Research, Section A: Accelerators, Spectrometers, Detectors and Associated Equipment 581 (1–2 SPEC. ISS.) (2007) 485–494, https://doi.org/10.1016/j.nima.2007.08.079.
[4] A.S. Tremsin, J.V. Vallerga, J.B. McPhate, O.H.W. Siegmund, R. Raffanti, High resolution photon counting with MCP-timepix quad parallel readout operating at >1 KHz frame rates, IEEE Trans. Nucl. Sci. 60 (April 2013)https://doi.org/10.1109/TNS.2012.2223714.
[5] A.S. Tremsin, J.B. McPhate, J.V. Vallerga, O.H.W. Siegmund, W.B. Feller, H.Z. Bilheux, J.J. Molaison, C.A. Tulk, L. Crow, R.G. Cooper, D. Penumadu, Transmission Bragg edge spectroscopy measurements at ORNL spallation neutron source, J. Phys. Conf. Ser. 251 (2010)https://doi.org/10.1088/1742-6596/251/1/012069.
[6] J.R. Santisteban, L. Edwards, V. Stelmukh, Characterization of textured materials by TOF transmission, Phys. B Condens. Matter 385–386 (2006) 636–638, https://doi.org/10.1016/j.physb.2006.06.090.
[7] H. Kakisawa, T. Sumitomo, IOP Publishing, The toughening mechanism of nacre and structural materials inspired by nacre, Sci. Technol. Adv. Mater. 12 (January 26, 2011)https://doi.org/10.1088/1468-6996/12/6/064710.
[8] D. Chateigner, C. Hedegaard, H.R. Wenk, Mollusc shell microstructures and crystallographic textures, J. Struct. Geol. 22 (2000) 1723–1735.
[9] E. Strack, Pearls, Ruhle-diebener-Verlag, 2006 87.
[10] N. Sturman, The microradiographic structures of non-bead cultured pearlsa, Lab Notes, August 20, 2009.
[11] K. Scarratt, T.M. Moses, S. Akamatsu, Characteristics of nuclei in Chinese freshwater cultured pearls, Gems & Gemology 36 (2) (2000) 98–109.
[12] N. Sturman, E. Strack, "Soufflé" freshwater cultured pearls, Gems & Gemology 46 (2) (2010) 61–63.
[13] L.E. Cartier, M.S. Krzemnicki, New developments in cultured pearl production: use of organic and baroque shell nuclei, Aust. Gemmol. 25 (1) (2013).
[14] A.S. Tremsin, J.V. Vallerga, J.B. McPhate, O.H.W. Siegmund, Optimization of Timepix count rate capabilities for the applications with a periodic input signal, J. Instrum. (May 2014) 9.
[15] FIZ Karlsruhe, ICSD – the inorganic crystal structure database, https://www.fiz-karlsruhe.de/de/leistungen/kristallographie/icsd.html [Online].
[16] B. Münch, P. Trtik, F. Marone, M. Stampanoni, Stripe and ring artifact removal with combined wavelet-Fourier filtering, Opt. Express 17 (2009) 8567, https://doi.org/10.1364/OE.17.008567.
[17] MathWorks, *https://www.mathworks.com/products/matlab.html* [Online].
[18] P. Gilbert, Iterative methods for the three-dimensional reconstruction of an object from projections, J. Theor. Biol. 36 (1972) 105–117, https://doi.org/10.1016/0022-5193(72)90180-4.
[19] W. van Aarle, W.J. Palenstijn, J. Cant, E. Janssens, F. Bleichrodt, A. Dabravolski, J. De Beenhouwer, K.J. Batenburg, J. Sijbers, Fast and flexible X-ray tomography using the ASTRA toolbox, Opt. Express 24 (22) (2016) 25129–25147.

[20] ROOT, I. Antcheva, M. Ballintijn, B. Bellenot, M. Biskup, R. Brun, N. Buncic, Ph. Canal, D. Casadei, O. Couet, V. Fine, L. Franco, G. Ganis, A. Gheata, D.G. Maline, M. Goto, J. Iwaszkiewicz, A. Kreshuk, D. Marcos Segura, R. Maunder, L. Moneta, A. Nauman, E. Offerman, V. Onuchin, S. Panacek, F. Rademakers, P. Russo, M. Tadel, A C++ framework for petabyte data storage, statistical analysis and visualization, Comput. Phys. Commun. 180 (2009) 2499–2512.
[21] J.R. Santisteban, L. Edwards, A. Steuwer, P.J. Withers, Time-of-flight neutron transmission diffraction, J. Appl. Crystallogr. 34 (2001) 289–297.
[22] R. Woracek, D. Penumadu, N. Kardjilov, A. Hilger, M. Boin, J. Banhart, I. Manke, 3D mapping of crystallographic phase distribution using energy-selective neutron tomography, Adv. Mater. 26 (2014) 4069–4073, https://doi.org/10.1002/adma.201400192.
[23] FEI, https://www.fei.com/software/amira-avizo/ [Online].

Paper III

Measurement of the thickness of B_4C deposits over 3D grids via multi-angle neutron radiography

G. Vitucci[1], T. Minniti[2], G. Angella[3], G. Croci[1], A. Muraro[1], C. Höglund[4,5], C. C. Lai[5], E. Perelli Cippo[6], G. Albani[1], R. Hall-Wilton[5,7], Linda Robinson[5], G. Grosso[6], M. Tardocchi[6] and G. Gorini[1]

[1]*University of Milano Bicocca, Dept. Phys., 20125 Milan, Italy;*
[2]*STFC-Rutherford Appleton Laboratory, ISIS Facility, Harwell, OX11 0QX, UK;*
[3]*IENI-CNR, Via Cozzi 53, Milan, Italy;*
[4]*Dept. of Physics, Chemistry and Biology (IFM), Thin Film Physics Division, Linköping University, SE-581 83 Linköping, Sweden;*
[5]*European Spallation Source ERIC, P.O. Box 176, SE-221 00 Lund, Sweden*
[6]*Istituto di Fisica del Plasma "P. Caldirola", IFP-CNR, Via Cozzi 53, Milan, Italy;*
[7]*Mittuniversitetet, 851 70 Sundsvall, Sweden.;*

E-mail: g.vitucci@campus.unimib.it

Abstract. At the present time, different kinds of thermal neutron detectors are under development at the European Spallation Source research facility, in order to overcome the well-known problem of the ^{3}He shortage. One of these new systems relies on the use of a three-dimensional neutron converter cathode that consists of a stack of aluminum grids, covered by a 0.9 µm ^{10}B enriched boron carbide layer ($^{10}B_4C$). As the conversion efficiency is a function of the boron thickness and the mean free path of the charged particles produced in the neutron induced reaction, the characterization of the boron carbide layer uniformity over the grids becomes crucial. In this work, a non-destructive method to map the thickness distribution of the converter layer over the grids is shown. The measurements exploit the white-beam neutron radiography technique where the specimen is irradiated at different angles. This experiment has been performed at the IMAT beamline operating at the ISIS spallation neutron source (UK). The results confirm that this non-destructive, wide-ranging technique allows a reliable and fast sample characterization and that it may be exploited in similar analyses where equivalent requirements are requested.

1. Introduction

1.1 New generation detectors at ESS

The upcoming European Spallation Source research facility [1] has pushed the development of new types of detectors capable to sustain high neutron counting rates, brought by the bright neutron flux of ESS [2], [3],[4], and large area coverage at reasonable cost (< 500 k€/m^2). In fact the problem of the ^{3}He shortage [5] reduces the possibility to employ it as a converter in neutron detectors for research. One possibility of overcoming such issue is represented by the BAND-GEM (Boron Array Neutron Detector GEM) neutron detector [6]. It consists of a triple-Gas Electron Multiplier (GEM) coupled with a three-dimensional (3D) converter. The latter

consists of a stack of aluminum grid planes covered by a layer of boron carbide[7]–[9], where the incoming neutrons are converted predominantly in alpha and lithium particles [10] and ionize the surrounding Ar/CO_2 gas. The electron cloud is then drifted by an electric field towards a triple GEM and converted into an electrical signal. Such a detector is expected to provide an efficiency > 30% [6] in the wavelength range from 2 Å to 12 Å of interest for the future Small Angle Neutron Scattering (SANS) instrument at ESS, like the LoKI beamline currently under construction [11]. Being the stack of many grids (24 at the present stage), a fast and non-destructive way to map the thickness all over these components is needed. In this work, a novel method based on white-beam neutron radiography is presented. It allows the extrapolation of the effective boron thickness deposited on the samples by interpolating the different gray level values of the radiographies taken at different angles with respect to the incident neutron beam.

1.2 Design of the 3D converter system for the BAND-GEM detector for LOKI

The design and the production of the BAND-GEM full module is driven by the LoKI beamline requirements [11]. This detector has a trapezoidal design that optimizes the momentum resolution needed in a SANS experiment. Since the external dimension of the LoKI detector is 428 mm x 526 mm, a grid plane of the 3D converter system is composed of multiple grids with smaller dimensions, with lengths of the longest side and distance between the two parallel sides in between 6 × 11 cm ("Grid 5") and 11 × 23 cm ("Grid 3"). Figure 1 shows a grid plane assembly.

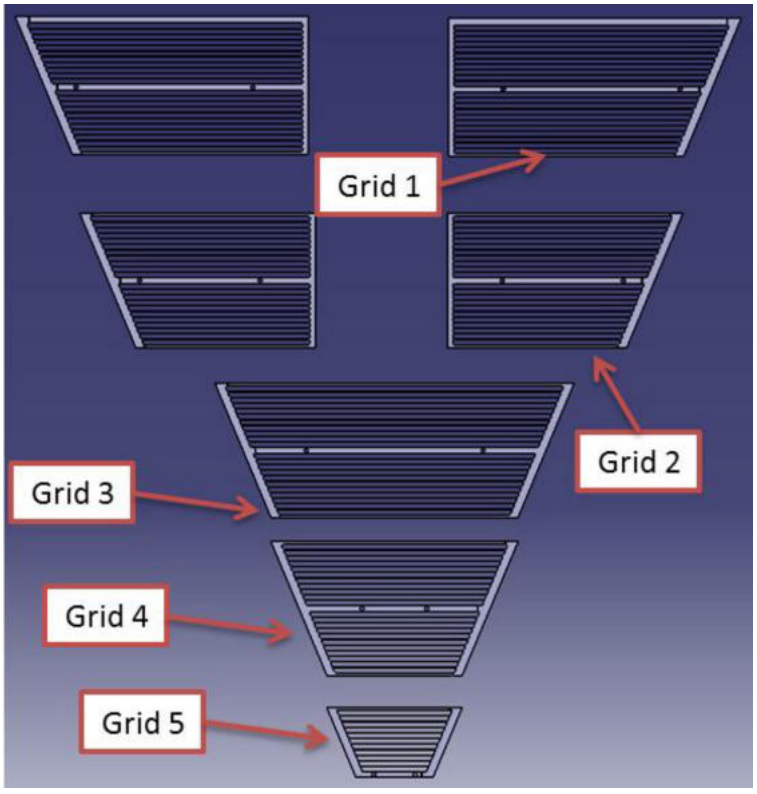

Figure 1: Assembly of the grid plane. Each grid is labeled from 1 to 5 for easy reference in the text.

Each grid is 3 mm thick and it is constituted by 20 lamellae each 200 µm thick. The distance between each lamella is equal to 4 mm. The design of the 3D converter system of the detector was limited by several technical constraints, the most demanding of which were the maximum dimensions of the grids and the thickness and uniformity of the deposited $^{10}B_4C$ along the lamellae. Several Monte-Carlo and FEM analysis of the entire BAND-GEM detector showed that the optimum in neutron detection efficiency is reached when the $^{10}B_4C$ layer as a thickness in the range of 0.6 – 1.0 µm (Figure 2a). The industrial coating unit (CC800/9, CemeCon AG, Germany) at the ESS detector coating facility in Linköping was used to deposit the neutron

active layer of the BAND-GEM grids. The thickness variation of $^{10}B_4C$ films is less than 10 % for samples shorter than 28 cm, as shown in Figure 2b, and therefore fulfills the thickness uniformity requirements.

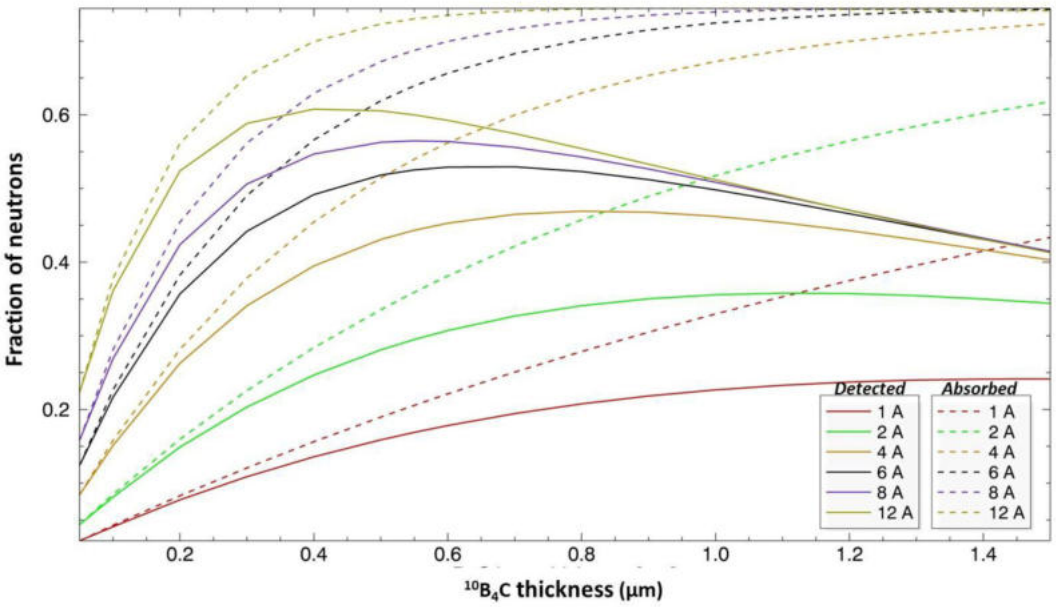

a)

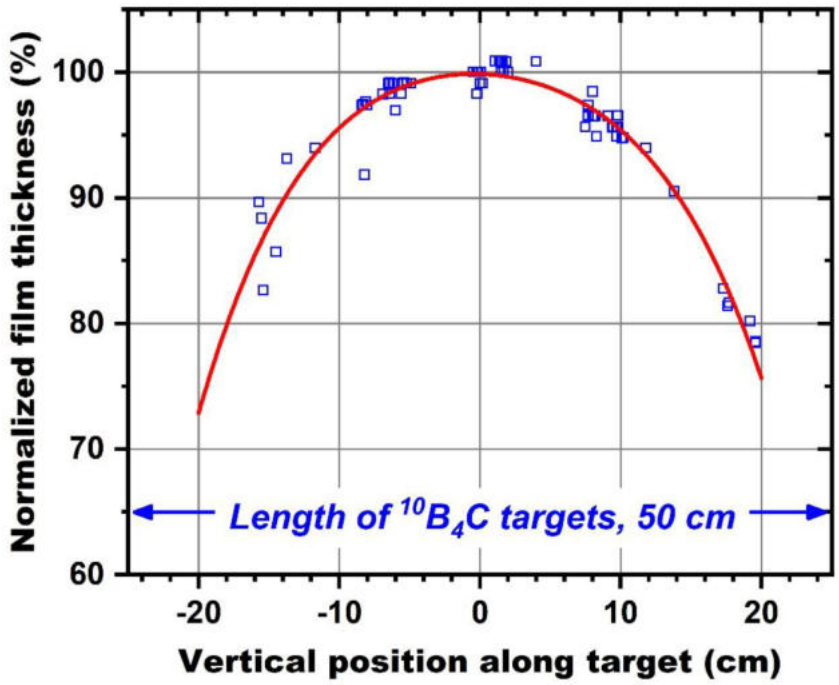

b)

Figure 2 : a) Plot of the neutron detection efficiency versus the thickness of the $^{10}B_4C$ layer deposited on the lamellae. The dotted line shows the expected efficiency as a function of the $^{10}B_4C$ neutron absorption probability and the geometrical parameters of the 3D converter of the BAND-GEM detector, while the continuous line includes also the escape probability of the ionizing particles from the $^{10}B_4C$ layer. b) Normalized thickness of $^{10}B_4C$ films plotted against the vertical distance from the center of the sputtering targets. The data was collected from many deposition runs in the industrial coating unit at ESS in Linköping, using 2-fold substrate rotation.

After the deposition process, a check of the actual $^{10}B_4C$ layer thickness present over the lamellae was needed, since this factor strongly affects the final detection efficiency of the BAND-GEM detector. Such a test must be non-destructive, since the samples have to be used for the assembly of the 3D converter, and must be effective in finding the $^{10}B_4C$ layer thickness with an accuracy of hundreds of nanometers. To do so, a novel procedure able to comply with these constraints was developed. It mainly consists of two parts: firstly, the acquisition of several neutron radiographies of the specimens exposed to the neutron beam at different angles; secondly, an accurate data analysis to extract the useful information and give an easy graphical representation of the results.

2. Methods

2.1 Theoretical description

The main idea behind this method relies on the Beer-Lambert equation describing the general principle that radiation is attenuated on passing through matter:

$$I(x,y,E) = I_0(x,y,E)e^{-\int_{path}\sigma(x,y,z,E)ds} \qquad (1)$$

where I_0 and I are the incident and attenuated radiation intensities, respectively, σ is the linear attenuation coefficient of the material (combining the interaction cross-section and nuclear) and s is the path length through the sample. For the depicted sample geometry of Figure 3, as in the case of the specimens analyzed in this work, the previous equation can be simplified as follows:

$$I_{trans} = I_0 \cdot e^{-\Sigma \cdot t_{eff}} \qquad (2)$$

where $\sum$ is the macroscopic cross section of the target material and t_{eff} is the effective thickness. The latter is equal to the real thickness of the sample multiplied by $\cos(\theta)^{-1}$, with θ being the angle between the incident radiation and the segment defining the real thickness of the target. In the specific case, the real thickness is the sum of the thickness bulk of the strip, made of aluminum, and two boron layers lying on both sides; thus, the macroscopic cross sections of both materials must be considered.

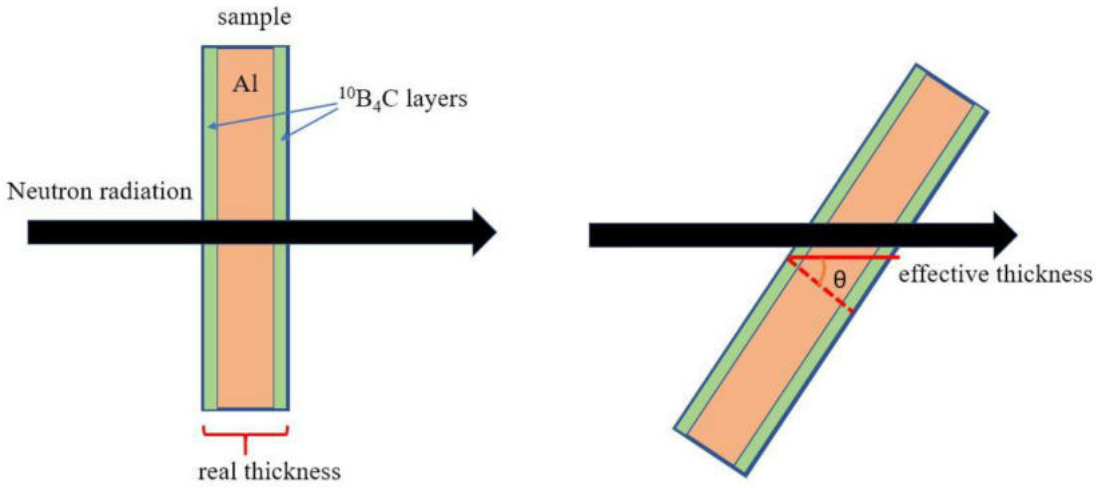

Figure 3: Effective thickness of the sample (lamella) when it is orthogonal (left) and inclined (right) with respect to the incident radiation. In the second case, the effective thickness as seen by the radiation is wider.

Equation (2) can be rearranged to have a direct dependence between the ratio of the transmitted and incoming radiation and the effective thickness. In facts:

$$\frac{-ln\frac{I}{I_0}}{\Sigma} = t_{eff} = t_{real}\frac{1}{cos\,\theta} \qquad (3)$$

Since I and I_0 can be extracted from the radiography, $\sum$ is known and θ is controlled during the measurement, t_{real} can be calculated by fitting the data given by each radiography collected at different angular steps.

2.2 Experimental setup

The experiment has been performed at the Imaging and Materials Science & Engineering (IMAT) beamline operating at the ISIS spallation neutron source (UK) [12], [13]. High resolution neutron radiography (NR) are performed at IMAT with a neutron beam size of about 200x200 mm^2 and parallel-beam geometry with a pinhole geometry of 4 cm in diameter and with a source-to-sample distance of 10 m that define a collimation ratio L/D of 250. The pixel size of the present measurements is 0.103 mm. The neutron flux as a function of the neutron wavelength available with these instrument settings is shown in Figure 4 [14].

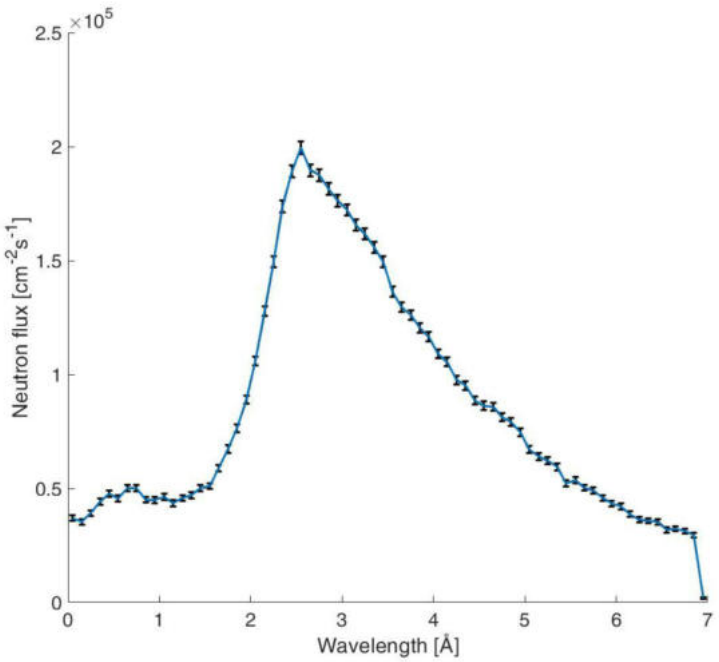

Figure 4: Neutron beam flux values as a function of neutron wavelength for the neutron beam divergence L/D of 250 used in the experiment at the IMAT beamline.

Radiographies were collected using a neutron tomography camera, i.e. a CMOS (2048 x 2048 pixels and field of view (FOV) of 211.5x211.5 mm^2) coupled to a neutron-sensitive scintillator screen (Figure 5). The latter consists of a 200 µm thick 6-LiF/ZnS:Cu screen used to convert neutrons into visible light; the CMOS device takes images of the emitted light through an objective lens system positioned at 90° respect to the neutron beam. For each NR measurement taken at a given angle between the sample surface and the incoming neutron beam, multiple radiographies were acquired along with periodic dark and flat field images with an integration time of 30 s each. The dark (I_{dark}) and flat field (I_0) images were used for normalization purpose to represent the attenuation of the beam instead of an intensity reading. For each data types (sample, flat and dark fields) an average of 3, 30 and 30 different NRs respectively was required to improve neutron statistic and noise reduction. The normalized image (I_{norm}) was computed using

$$I_{norm} = \frac{I - I_{dark}}{I_0 - I_{dark}} \quad (4)$$

where (I_{dark}) takes into account the electronic camera noise.

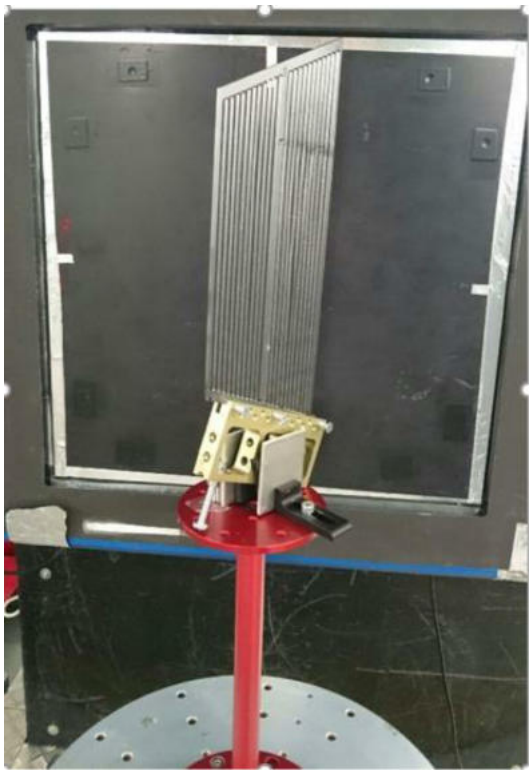

Figure 5: Setup of the neutron radiography with the aluminum grid installed on the rotation stage.

2.3 Data analysis

The data analysis was carried out with the MATLAB [15] programming language. The median of the different image types (sample, flat and dark fields) was extracted and the final normalized NR calculated. A line profile along the orthogonal direction of the specimen was performed considering the region of interest (ROI) depicted in Figure 6a. Each point in the profile is averaged with the values of five neighbor pixels in the direction parallel to the lamellae. This means that every point in the 2D plot (Figure 6b) corresponds to 0.103 × 5 mm on the lamellae (the width of the red rectangle of Figure 6a). A periodical behavior is noticeable, where the minima represent the pixels covered by the strips of the grid, while the maxima correspond to the fully irradiated pixels in the space between the strips. As a consequence, a Fast Fourier Transform algorithm was implemented in the code to determine the length of such period for each radiography at a selected angle (Figure 6b, 6c).

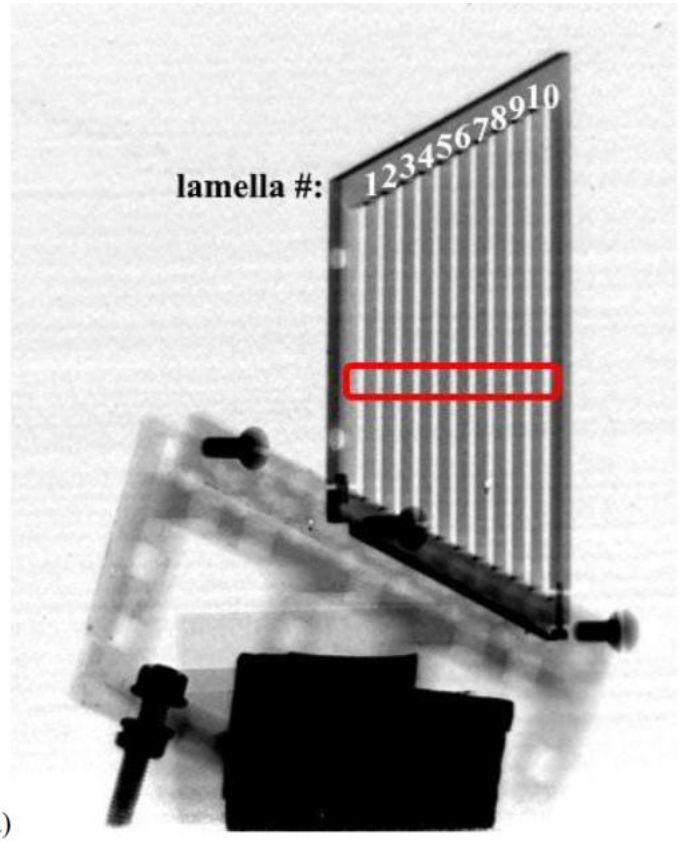
lamella #:
12345678910

a)

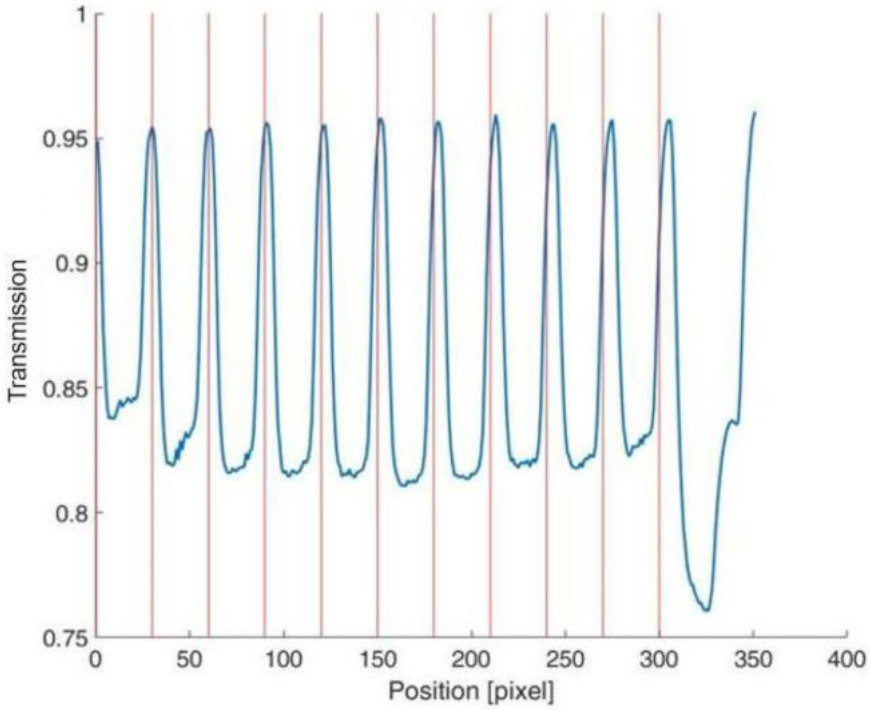
1
0.95
0.9
0.85
0.8
0.75
Transmission
0
50
100
150
200
250
300
350
400
Position [pixel]

b)

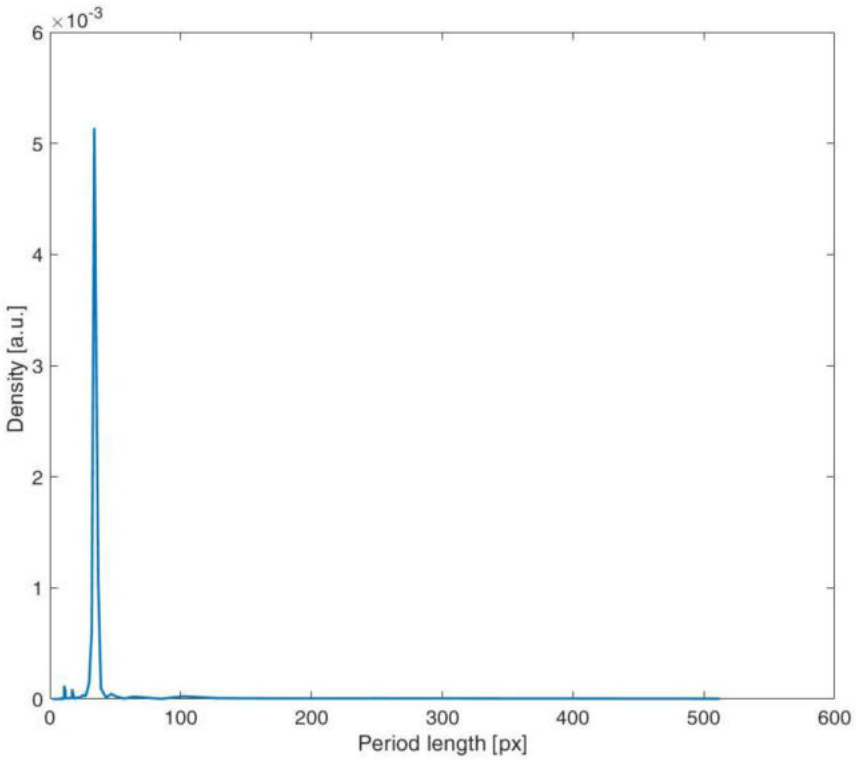

c)

Figure 6: a): Image of the aluminum grid at 22 degrees with respect to the beam and ROI considered in the analysis. Grids lamellae are labeled starting from the shortest to the longest one in ascending order. b): profile plot of the portion of the image marked on (6a). The period of the function was automatically found by use of Fourier transform. The minima represent the point where lamellae were located (absorption took place) while the maxima are the points were the full neutron beam was converted by the detector. c) Periodogram obtained by Fourier analysis. The maximum of such function reveals the distance (in pixels) between each lamella.

The apparent distance between the lamellae varied at every rotation step, because of the shift in perspective. Despite this, such a method was capable to automatically find the period length in each image. The periodogram returned by the algorithm was then used for the calculation of the transmission values over the grid, following the algorithm in Figure 7. The minimum average is calculated in every period in order to avoid that dark pixels or other artifacts may confuse the identification of the real transmission value. Furthermore, the value of the macroscopic cross section $\sum$ of the $^{10}B_4C$ plus the aluminum substrate was calculated by convoluting the total nuclear reaction cross sections of the relevant elements (nuclear database accessible through the NEA website [16]) with the incident neutron spectrum of IMAT (Figure 4). In this way, each lamella of the grid gets a value directly related to the boron layer thickness on its length, with an uncertainty on the position given by the discretization of the thickness map in small elementary regions (sectors) of 5×40 pixels. This algorithm is then iterated all over the grid and for all the considered angles, until the slope is obtained.

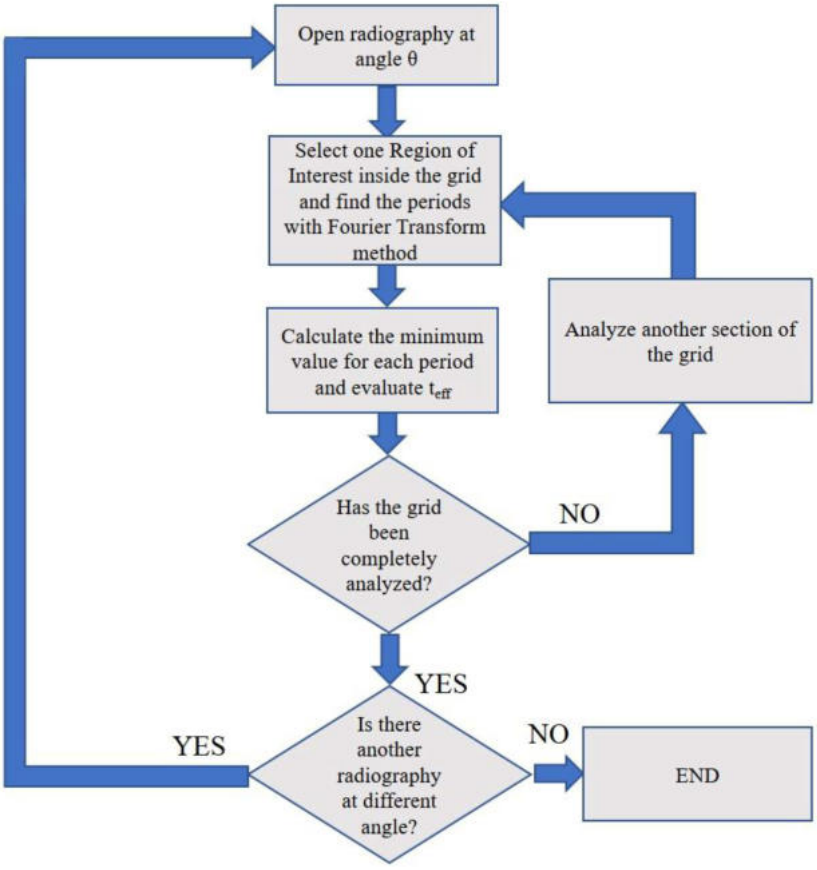

Figure 7: Flow chart of the algorithm coded in MATLAB. This routine is executed for all the sectors inside one single transmission image and for all the transmission images collected at different angles during the experiment.

3. Results and discussions

An example of the graphical output displayed by the program is shown in Figure 8a, where the "Grid 1" is considered. The thickness evaluation for every sector (colored rectangle) comes from the computation of the slope of the line visible in Figure 8b, divided by a factor of two, in order to take into account only one side of the covered lamellae. Such line represents the function described in Equation (3). In the x-axis, the inverse of the cosine of the angle at which the grid was exposed with respect to the radiation is indicated, while in the y-axis the effective thickness is calculated. The x error bars represent the uncertainties on the position of the sample with respect to the direction of the neutron beam, estimated to be of 0.25 degrees, while the y error bars were calculated with the standard error propagation operated on the equation (3), considering the 16 bit resolution of the acquired radiographies and the uncertainty on the neutron beam flux as shown in Figure 4 . Thus, the uncertainty of the boron layer thickness calculated for any sector of the grid is below 120 nm.

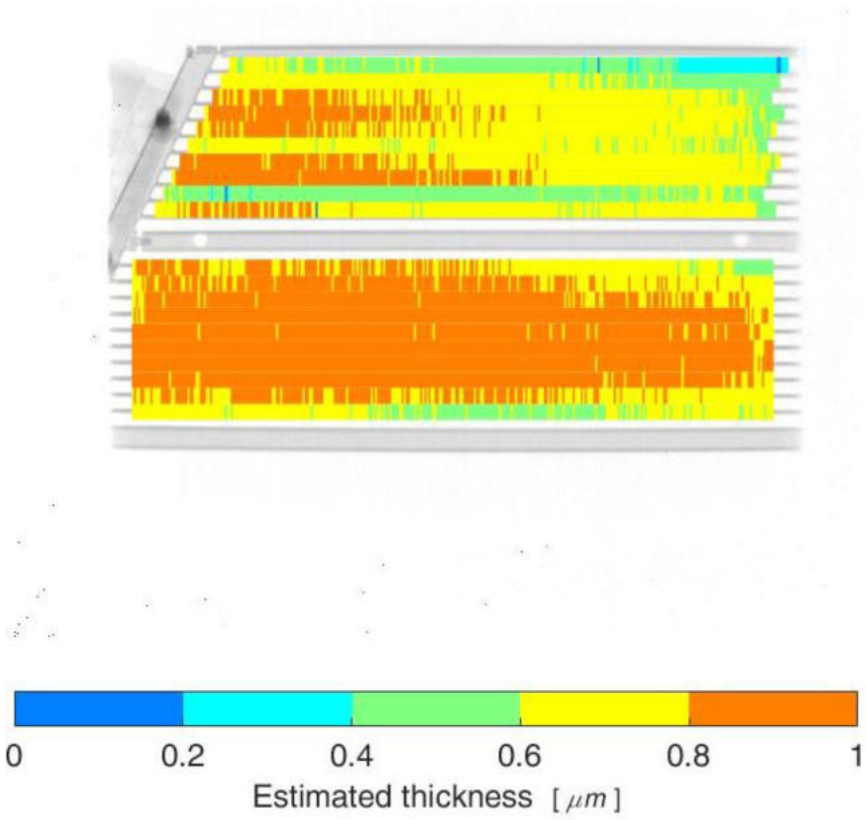

a)

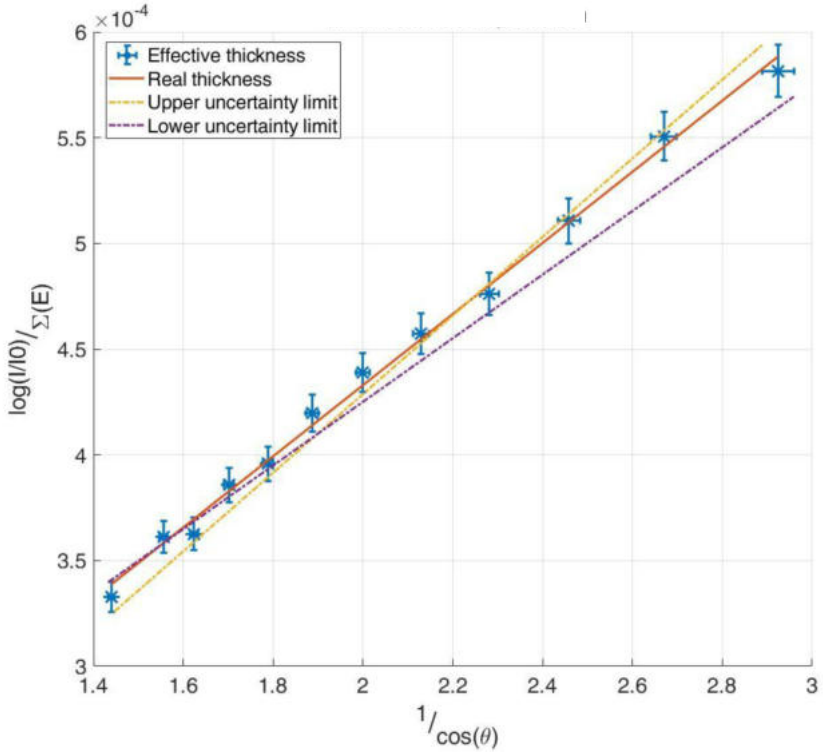

b)

Figure 8: Colored map (a) of the boron layer thickness over the grid. Each value is extrapolated by the slope of the interpolation line of the effective thicknesses of the lamellae at different angles (b).

The rest of the analyzed grids (grid #3 and #5) showed the same layer thickness distributions. Most of the sectors are included in the 0.6 -1.0 µm thickness range (Figure 9a), which is acceptable for this setup. Nonetheless, there are several lamellae where the estimated layer thickness decreases significantly, localized either close to the edges of the grid (lamella # 1, #20) or next to the middle support frame (lamella # 9) as seen in Figure 9b. During deposition, all grids had an extra frame mounted, which provided more rigidity of the setup but with the drawback of causing shadowing of the sputtered particle flux towards the nearest lamellae. The thinner boron coating next to the frame was further investigated and confirmed by scanning electron microscopy (SEM) as shown in Figure 10. In facts, pieces of aluminum lamellae from selected positions in the grid driven by this non-destructive neutron testing were cut out and incorporated in bakelite. After being grounded with silicon paper and mechanically polished with diamond, a SEM SU70 by Hitachi was used to study the cross sections of the lamellae pieces and to measure the boron layer thickness. Figure 10 shows that the boron is more present on the lamellae furthest away from the supporting frame (lamella #15), as shown in (a), compared to a lamella that was next to the frame (lamella #20), as shown in (b). Figure 9c shows the variation of the thickness along the short (#5), medium (#3) and long (#1) grids, with every data point obtained from the average of 10 lamellae and with a pixel width of 0.515 mm along each lamella. In the figure, each grid is positioned centred on sector #250, which approximately corresponds to the centre of the grid mounting in the deposition chamber during the coating phase. A uniform thickness distribution is found along the two short grids (#1 and #5) and over 2/3 of the longest grid (#3). The significant increase for parts of grid 3, the overall longest grid, is explained by the higher flux of sputtered particles outside the height where the other grids were mounted. This shows the accuracy and usefulness of the applied measurement technique, but also the importance of a controlled grid mounting during the deposition process. The lower converter deposit observed in some lamellae (for instance lamella #9 in Figure 8a) is caused by their twisting due to a mechanical failure at the junctions with the aluminium frame support. Therefore, only selected grids with well straightened lamellae will be employed for the final assembly of the 3D neutron converter.

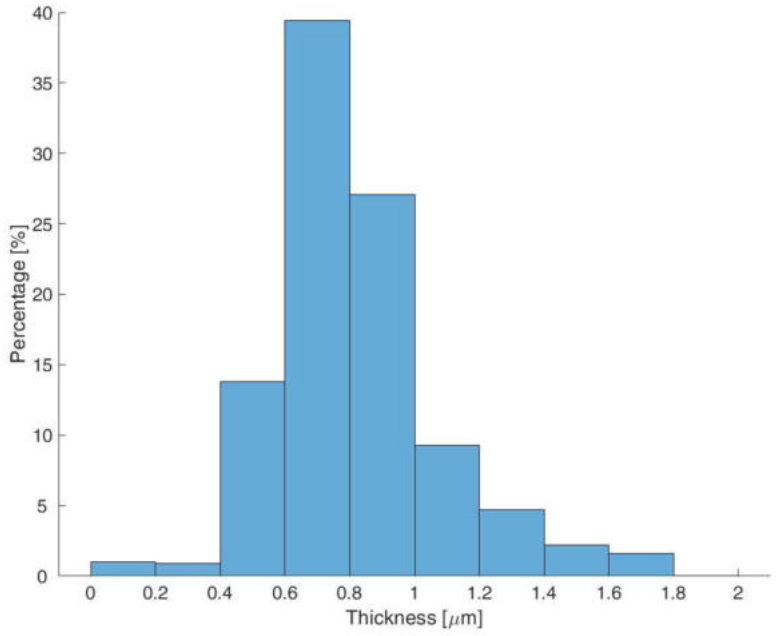

a)

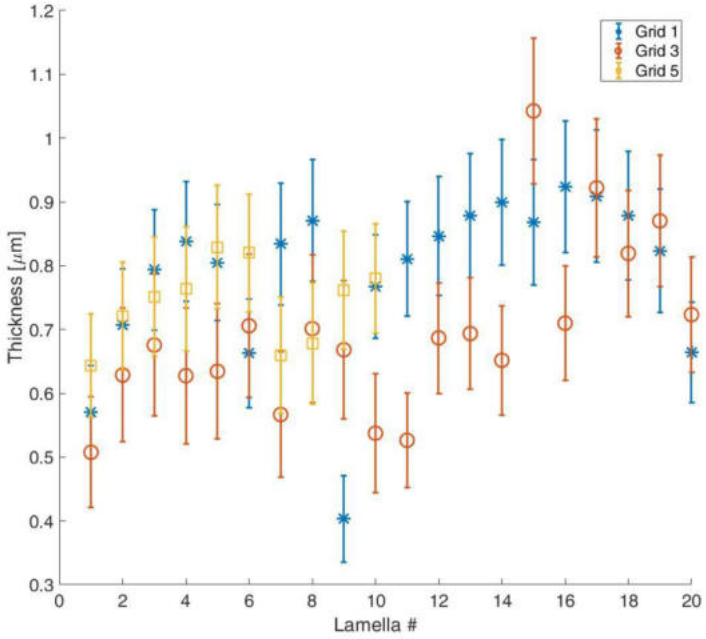

b)

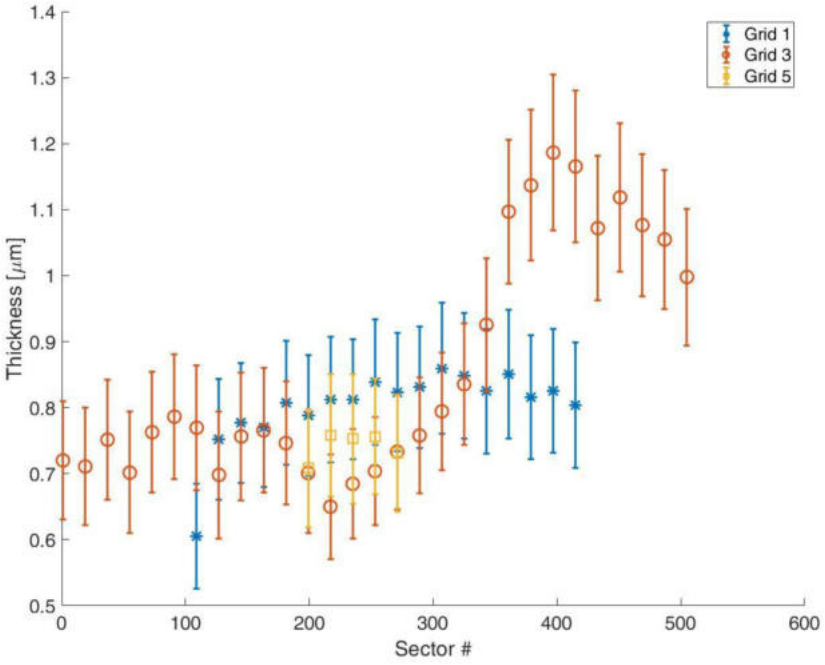

c)

Figure 9: a): Boron thickness distribution percentage on grid #1, #3 and #5. b): thickness profile across the grids. A smaller amount of boron was deposited at the extremities of the grids and in the middle part, where the supporting frames are located. c): thickness profile over lamellae placed in the central part of the grid. The peak of the sputtered boron cloud reached one extremity of the longest grid, while less amount was deposited on the other side and on the remaining grids.

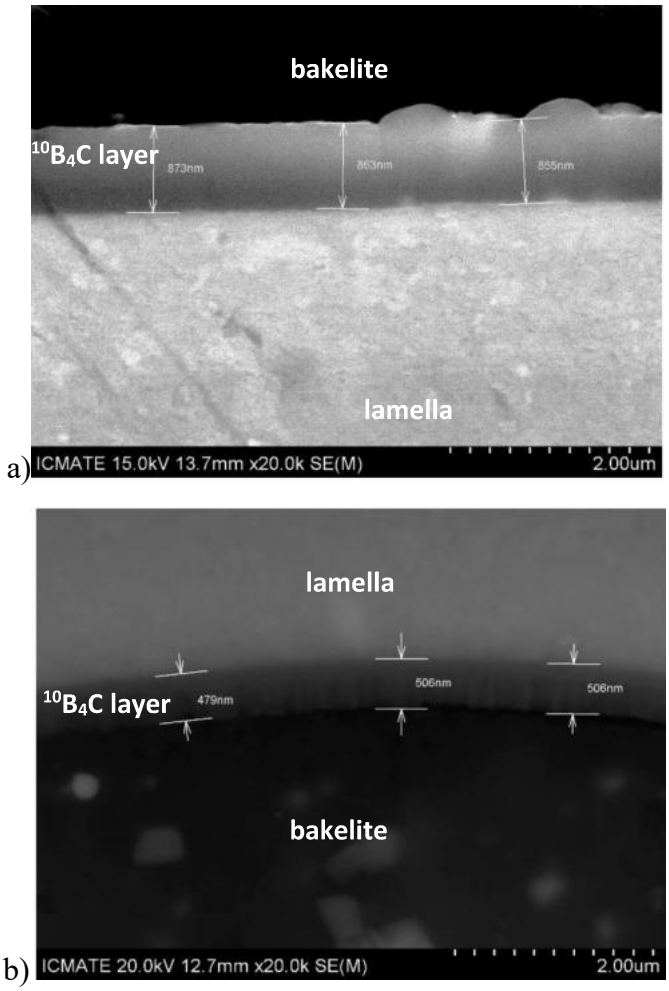

Figure 10: SEM photos of lamella # 15 (a) and # 20 (b) of grid #3. Case a) is the most frequent, while case b) may occur at the extremities of the grids, where the boron covering is obstructed by the presence of the supporting frame.

4. Conclusions

In this work a fast, non-destructive method to characterize the thickness of the boron layer deposited on the aluminum grids that will constitute the core of the BAND-GEM full module has been presented. The results showed a reliable measurement of the neutron converter $^{10}B_4C$ layer thickness with an uncertainty of 120 nm, which is sufficient for the diagnosis purposes of the detector presented. Nonetheless, this technique may be easily adapted and implemented in any experiment where the extrapolation of the layer thickness of a certain material has to be performed with a fast and non-destructive procedure.

5. Acknowledgments

The CNR-STFC agreement 2014–2020 (No. 3420 2014–2020) concerning collaboration in scientific research at the ISIS Spallation Neutron Source is gratefully acknowledged. C. Hoglund, CC Lai, L. Robinson and R. Hall-Wilton would like to acknowledge the support from the EU Horizon 2020 BrightnESS grant (676548). G. Vitucci would like to thank Giovanni Posadinu for his support.

References

[1] ESS, “European Spallation Source.” [Online]. Available: http://europeanspallationsource.se/.

[2] O. Kirstein *et al.*, “Neutron position sensitive detectors for the ESS,” in *Proceedings of Science*, 2014, vol. 15–19–Sept.

[3] R. Hall-Wilton and C. Theroine, “Status of the European Spallation Source ESS AB, the instrument selection process, and a fundamental physics beamline at the ESS,” in *Physics Procedia*, 2014, vol. 51, pp. 8–12.

[4] K. Kanaki *et al.*, “Detector rates for the Small Angle Neutron Scattering instruments at the European Spallation Source,” May 2018.

[5] R. T. Kouzes, “The 3He Supply Problem,” *Pacific Northwest Natl. Lab.*, vol. PNNL-18388, pp. 1–12, 2009.

[6] A. Muraro *et al.*, “Performance of the high-efficiency thermal neutron BAND-GEM detector,” *Prog. Theor. Exp. Phys.*, vol. 2018, no. 2, Feb. 2018.

[7] C. Höglund *et al.*, “B4C thin films for neutron detection,” in *Journal of Applied Physics*, 2012, vol. 111, no. 10.

[8] C. Höglund *et al.*, “Stability of 10B4C thin films under neutron radiation,” *Radiat. Phys. Chem.*, vol. 113, pp. 14–19, 2015.

[9] S. Schmidt, C. Höglund, J. Jensen, L. Hultman, J. Birch, and R. Hall-Wilton, “Low-temperature growth of boron carbide coatings by direct current magnetron sputtering and high-power impulse magnetron sputtering,” *J. Mater. Sci.*, vol. 51, no. 23, pp. 10418–10428, 2016.

[10] G. F. Knoll, “Radiation Detection and Measurement,” *Phoenix Usa*, vol. 3. p. 830, 2010.

[11] A. J. Jackson *et al.*, “LoKI - A Broad Band High Flux SANS Instrument for the ESS,” in *Proceedings ICANS XXI Conference*, 2015.

[12] W. Kockelmann *et al.*, “Status of the Neutron Imaging and Diffraction Instrument IMAT,” in *Physics Procedia*, 2015, vol. 69, pp. 71–78.

[13] T. Minniti *et al.*, “Materials analysis opportunities on the new neutron imaging facility IMAT@ISIS,” *J. Instrum.*, vol. 11, no. 03, pp. C03014–C03014, 2016.

[14] T. Minniti, K. Watanabe, G. Burca, D. E. Pooley, and W. Kockelmann, “Characterization of the new neutron imaging and materials science facility IMAT,” *Nucl. Instruments Methods Phys. Res. Sect. A Accel. Spectrometers, Detect. Assoc. Equip.*, vol. 888, pp. 184–195, 2018.

[15] Mathworks, “MATLAB.” [Online]. Available: https://it.mathworks.com/products/matlab.html.

[16] Nuclear Energy Agency, “NEA.” [Online]. Available: https://www.oecd-nea.org/janis/nea_database.html.

Paper IV

Jinst

Published by IOP Publishing for Sissa Medialab

Received: *December 18, 2017*
Accepted: *January 10, 2018*
Published: *January 25, 2018*

International workshop on Imaging II
4–8 September 2017
Varenna, Italy

Towards high-resolution neutron imaging on IMAT

T. Minniti,[a,1] **A.S. Tremsin,**[b] **G. Vitucci**[c] **and W. Kockelmann**[a]

[a] *STFC, Rutherford Appleton Laboratory, ISIS Facility, Harwell, OX11 0QX, U.K.*
[b] *University of California at Berkeley, Space Science Laboratory, CA 94720 Berkeley, U.S.A.*
[c] *University of Milano Bicocca, Department of Physics, 20125 Milan, Italy*

E-mail: triestino.minniti@stfc.ac.uk

Abstract: IMAT is a new cold-neutron imaging facility at the neutron spallation source ISIS at the Rutherford Appleton Laboratory, U.K.. The ISIS pulsed source enables energy-selective and energy-resolved neutron imaging via time-of-flight (TOF) techniques, which are available in addition to the white-beam neutron radiography and tomography options. A spatial resolution of about 50 μm for white-beam neutron radiography was achieved early in the IMAT commissioning phase. In this work we have made the first steps towards achieving higher spatial resolution. A white-beam radiography with 18 μm spatial resolution was achieved in this experiment. This result was possible by using the event counting neutron pixel detector based on micro-channel plates (MCP) coupled with a Timepix readout chip with 55 μm sized pixels, and by employing an event centroiding technique. The prospects for energy-selective neutron radiography for this centroiding mode are discussed.

Keywords: Inspection with neutrons; Instrumentation for neutron sources; Neutron detectors (cold, thermal, fast neutrons); Neutron radiography

[1]Corresponding author.

https://doi.org/10.1088/1748-0221/13/01/C01039

Contents

2018 JINST 13 C01039

1 Introduction

In the last two decades neutron imaging has proven itself as a fast growing materials analysis technique. Nowadays it has becomes an essential tool for materials science and engineering studies in any modern large-scale neutron facility [1–9]. The fast development of this research field was driven, on the one hand, by the need of modern industries for advanced materials research that has increased the demand of complex and new imaging techniques [10, 11] and, on the other hand, by the advances in detection systems [12–15].

A new cold-neutron imaging facility IMAT installed at the accelerator-based pulsed neutron source ISIS at the Rutherford Appleton Laboratory in U.K. enables new neutron imaging methods [10, 11], such as energy-selective and energy-dispersive neutron imaging via time-of-flight (TOF) techniques. These techniques are available in addition to the white-beam neutron radiography and tomography options where no energy or wavelength information of the neutron probe is required. In general, white-beam neutron imaging integrates the attenuation coefficients of the specimen materials over all energies in the neutron spectrum, and therefore it is mostly probing the energy-averaged neutron absorption and scattering terms of the total neutron cross section. As a consequence, the energy dependent features are mostly lost in the averaged data. Conversely, energy-dispersive neutron imaging is capable to map the parameters of the drastic steps in the total neutron cross section of crystalline materials related to Bragg edges, originating from elastic coherent scattering. It has been demonstrated that the spectral resolution of each pixel can be used for determinations of Bragg edge positions [16], lattice parameter and strains [16], for a quantitative phase analysis [17] as well as for texture analysis [18]. Recursive data analysis for all the detector pixels is producing bi-dimensional and high spatial resolution maps of the microstructure and texture properties for the analysed specimen. Therefore high event neutron counting pixel detectors, further discussed in section 2.1, with high spatial and high timing resolution, are essential equipment on a pulsed-source instrument like IMAT. Besides the energy-resolving properties, these camera systems may be setup to improve the white beam options with a resolution beyond the detector pixel

size limit by event centroiding data analysis algorithms, as discussed in section 2.2. In this work, a feasibility study was aimed at pushing the spatial resolution of neutron imaging on IMAT via event centroiding methods. Moreover, the tests were performed during IMAT commissioning in order to evaluate the stability of the IMAT environment for high resolution analysis.

2 Experimental setup

IMAT [1, 2] is a new cold-neutron imaging facility installed on the ISIS second target station TS2, a low-power 10 Hz pulsed source of about 50 kW. Neutrons at ISIS are produced by nuclear spallation reactions induced by a high-energy proton burst impinging on a tungsten target. IMAT is situated in direct line of sight of the cold, coupled 18K hydrogen moderator. From the shutter, a straight supermirror guide consisting of m=3 Ni/Ti multi-layers coated onto float glass of 95 × 95 mm^2 aperture transports the beam to a pinhole selector at 46 m from the source. Three larger breaks in the neutron guide are required for accommodating a 20 Hz T0 chopper as fast neutron and gamma filter and two 10 Hz double-disk choppers used to define wider (e.g. 6 Å) or narrower (e.g. 1 Å) wavelength bands but also to prevent frame-overlap of neutrons between successive time frames. The pinhole collimates the beam and defines its divergence (or L/D) value, where D is the diameter of the aperture and L is the distance to the neutron camera. The rotating capabilities for a pinhole selector device offer a choice of five circular apertures for the imaging mode, to define different L/D ratios, and also contains one large square aperture of 100 × 100 mm^2. Finally from the pinhole the neutrons travel through approximately 9 m of vacuum tubes before reaching the sample position at 10 m from the selector wheel. The IMAT sample position system with its reference at 56 m from the source is used for sample alignment and rotation. A detailed description of the instrument and its measured performance has been given recently [19].

2.1 Detector and readout electronics

The detector used in present experiments was built by the University of California in collaboration with Nova Scientific [20]. It uses a stack of neutron-sensitive MCPs to convert incoming neutrons into an electron cloud (∼ 10^4–10^5 electrons per each registered neutron). These electrons are subsequently registered by a pixelated readout consisting of a quad assembly of Timepix chips [21] developed by the Medipix collaboration. The Timepix chip has a matrix of 256 × 256 pixels (55 × 55 mm^2 each) capable of measuring the number of incoming electrons. Thus the active area of the detector is 28 × 28 mm^2 and multiple simultaneous events can be detected, providing their charge footprints on the readout do not overlap. The flexibility of the readout allows operation in either very high counting rate mode with 55 μm pixel resolution (exceeding 10^8 neutrons/s) or high spatial resolution mode of ∼12 μm with count rate limited to ∼ $5 \cdot 10^6$ neutrons/s. It is the latter mode, which is referred to as centroiding mode, which is the neutron event counting mode used in this work.

2.2 Localization of neutron event through event centroiding

To achieve the highest spatial resolution, where neutrons are registered with spatial accuracy better than a pixel size, we utilize event centroiding [22, 23]. In that mode the charge cloud produced by the MCP stack is spread over several pixels. The center of that charge cloud is preserved with an

2018 JINST 13 C01039

accuracy of pore-to-pore distance, currently ~ 11 μm, as event amplification happens within the singe pore of the first plate, followed by few adjacent pores on the second MCP. Thus the majority of detected neutrons have a cluster of pixels on the Timepix readout (there are still some events which strike only few pixels and those are excluded from the subsequent analysis). The center of each cluster is then calculated from the measured charge values in each pixel. It is that cluster analysis which allows high resolution neutron imaging with sub-pixel accuracy. One of the limitations of this mode is the need to avoid event overlaps with a single readout frame: encoding of two events which have overlapping footprints cannot be done correctly unless these events are detected with two separate frames. With an optimized event area of ~ 10 pixels there are ~ 2500 events which can be detected per single readout frame with 10% overlap probability. Our current generation of Timepix readout is capable of ~ 1200 frames/s, with ~ 320 μs readout time (deadtime of the detector). Depending on the flux of incoming neutrons, the width of acquisition shutter is optimized to reduce the probability of event overlaps and to minimize the deadtime of the detector. The event centroiding is currently performed in real time in the data processing computer, where multiple cores of the processor are used to keep up with the speed of incoming data.

2.3 Experimental details

For the experiment IMAT was operated in single-frame mode providing a wavelength band of (1–7 Å) corresponding to a neutron TOF selection between 10 ms and 100 ms, obtained by use of the double-disk choppers. The incident neutron spectrum is shown in figure 1. The MCP camera was setup for collection in centroiding mode.

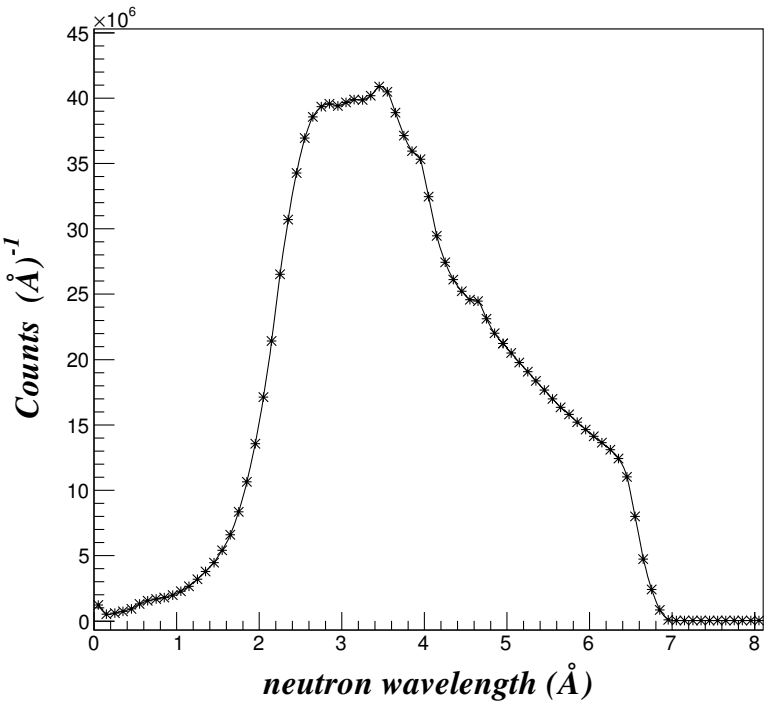

Figure 1. Incident neutron spectrum as a function of the neutron wavelength.

The beam size at the camera position was set to 35×35 mm^2 in order to irradiate the specimen and the entire detector active area but minimizing at the same time unnecessary air scattering. A neutron absorbing Gd-sputtered "Siemens Star" test pattern, shown in figure 2, was placed in close-contact to the neutron counting detector window. Constructively in the current detector the distance between the ^{10}B loaded neutron MCP converter and the detector window is around 12 mm. With a pinhole diameter selection D of 20 mm and a source (pinhole itself) to camera distance L of 10400 mm the resulting beam collimation ratio L/D was 520. From geometrical considerations the expected unsharpness in the radiography is of the order of $\sim$ 20 µm. The data from a plant leaf in front of the camera, as shown in figure 2, were not further analysed as it had shrunk during acquisition.

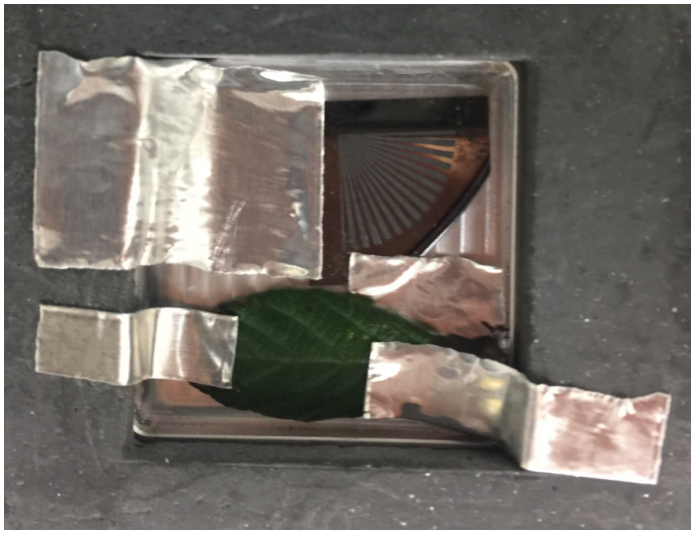

Figure 2. Neutron absorbing "Siemens Star" test pattern placed in close contact to the neutron counting detector window.

Such a configuration was selected as best compromise between spatial resolution and Signal-to-Noise Ratio (SNR). The MCP camera used a 10 Hz external trigger from the neutron source, and a number of 45 acquisition shutters for each ISIS pulse to minimize event overlap. The TOF and neutron wavelength ranges of these shutters used during the experiment are provided in table 1. This setup, in principal, allows energy-selection, although it was not used in this experiment.

For each interval registered neutron events are read-out, and used to determine the centroiding positions and to fill a 4k $\times$ 4k matrix. At this point the timing information is lost. The resulting white beam radiography is obtained by accumulating all detected neutron events within the provided ranges in table 1. The 4k $\times$ 4k radiography is thus generated with sub-pixel spatial resolution by means of event centroiding as described in section 2.2. We remark here that the overall process is currently performed in real time and only the final radiographies stored on the work station. Finally, the exposition time for the neutron radiography was of about 580 minutes.

2018 JINST 13 C01039

Table 1. Minimum and maximum TOF and neutron wavelength λ interval ranges used during the measurement.

$TOF_{min}(s)$	$TOF_{max}(s)$	λ_{min}(Å)	λ_{min}(Å)
0.0224	0.0240	1.5726	1.6849
0.0244	0.0260	1.7130	1.8253
0.0264	0.0280	1.8534	1.9657
0.0284	0.0288	1.9938	2.0219
0.0292	0.0296	2.0500	2.0780
0.0300	0.0304	2.1061	2.1342
0.0308	0.0312	2.1623	2.1904
0.0316	0.0320	2.2184	2.2465
0.0324	0.0328	2.2746	2.3027
0.0332	0.0336	2.3308	2.3589
0.0340	0.0344	2.3869	2.4150
0.0348	0.0352	2.4431	2.4712
0.0356	0.0360	2.4993	2.5273
0.0364	0.0368	2.5554	2.5835
0.0372	0.0376	2.6116	2.6397
0.0380	0.0384	2.6678	2.6958
0.0388	0.0392	2.7239	2.7520
0.0396	0.0400	2.7801	2.8082
0.0404	0.0408	2.8362	2.8643
0.0412	0.0416	2.8924	2.9205
0.0420	0.0424	2.9486	2.9767
0.0428	0.0432	3.0047	3.0328
0.0436	0.0440	3.0609	3.0890

$TOF_{min}(s)$	$TOF_{max}(s)$	λ_{min}(Å)	λ_{min}(Å)
0.0444	0.0448	3.1171	3.1451
0.0452	0.0456	3.1732	3.2013
0.0460	0.0466	3.2294	3.2715
0.0470	0.0476	3.2996	3.3417
0.0480	0.0486	3.3698	3.4119
0.0490	0.0496	3.4400	3.4821
0.0500	0.0506	3.5102	3.5523
0.0510	0.0516	3.5804	3.6225
0.0520	0.0526	3.6506	3.6927
0.0530	0.0536	3.7208	3.7629
0.0540	0.0546	3.7910	3.8331
0.0550	0.0556	3.8612	3.9033
0.0560	0.0566	3.9314	3.9736
0.0570	0.0581	4.0016	4.0789
0.0585	0.0596	4.1069	4.1842
0.0600	0.0611	4.2122	4.2895
0.0615	0.0626	4.3176	4.3948
0.0630	0.0641	4.4229	4.5001
0.0645	0.0656	4.5282	4.6054
0.0660	0.0676	4.6335	4.7458
0.0680	0.0696	4.7739	4.8862
0.0700	0.0716	4.9143	5.0266

3 Results

The neutron radiography of the Siemens star is shown in figure 3. It is a quite common process to investigate the edge spread behaviour of sharply contrasting materials like the Gd sputtered neutron absorbing "Siemens Star" test pattern displayed in the 4096×4096 sub-pixel neutron radiography. With eight times larger number of pixel compared with the 512×512 matrix of the Timepix chip, the expected pixel size is of the order of 6.875 µm. The edge-spread function (ESF) was determined using a selected edge in the test pattern specimen with high precision by averaging over approximately 250 pixels as shown in figure 4. Via the line-spread function (LSF), as the derivative of the ESF, the modulation transfer function (MTF) is derived by Fourier transformation. A 10% contrast cutoff was applied to the MTF shown in figure 5 to define the highest resolvable spatial frequency, and the inverse was calculated to determine the maximum achievable spatial resolution of the experimental setup. A value of 28 line-pairs per millimetres (lp/mm) was observed, corresponding to a spatial resolution of 18 µm. It is worth to notice that this value is very close to the expected blurring of $\sim$ 20 µm due to the beam divergence. Further improvements can be achieved by increasing the L/D ratio, for minimizing the impact of geometrical blurring.

2018 JINST 13 C01039

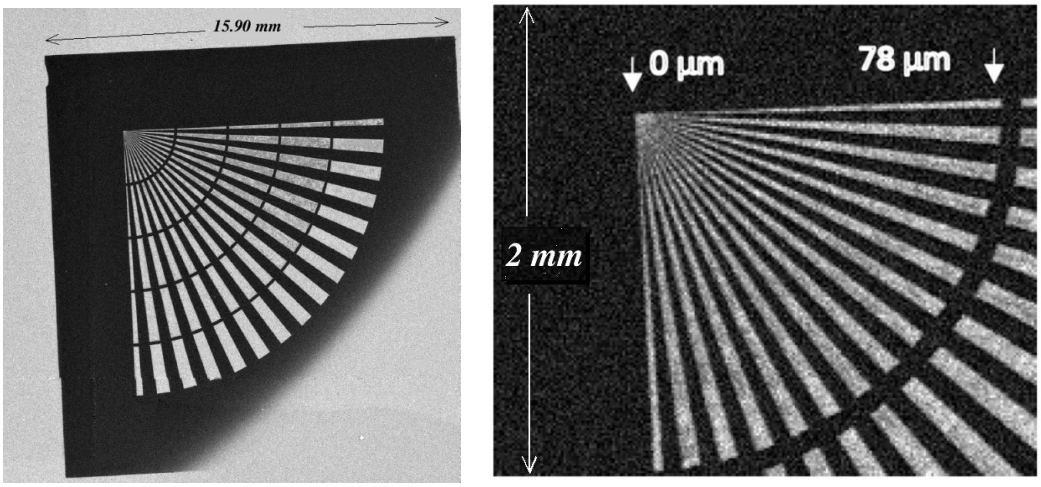

Figure 3. Siemens Star test pattern neutron radiography with sub-pixel spatial resolution (left panel) and zoom view of the inner pattern (right panel).

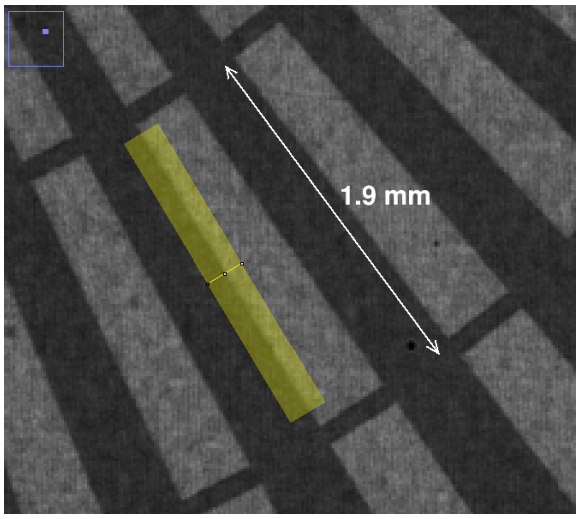

Figure 4. Area selected for the MTF evaluation.

4 Conclusions and outlook

High resolution neutron imaging has been flagged up as one of the key demands by the neutron imaging user community for the future development in the field. A further improvement of the IMAT spatial resolution towards and below 20 micron would benefit many IMAT projects, ranging from studies on electrochemical cells, batteries, materials for nuclear safety, soft matter, and soil physics. By employing the centroiding mode of the MCP camera a spatial resolution of 18 µm could be achieved. It is worth to notice that a comparable and even better spatial resolution neutron radiography and tomography with shorter acquisition times has recently been performed at other neutron imaging facilities [23–25]. The spatial resolution that IMAT can achieve eventually is limited by the available neutron flux on target station 2 and the efficiency of the beam transport. Consequently, the counting time of several hours for obtaining the radiography was particularly long

2018 JINST 13 C01039

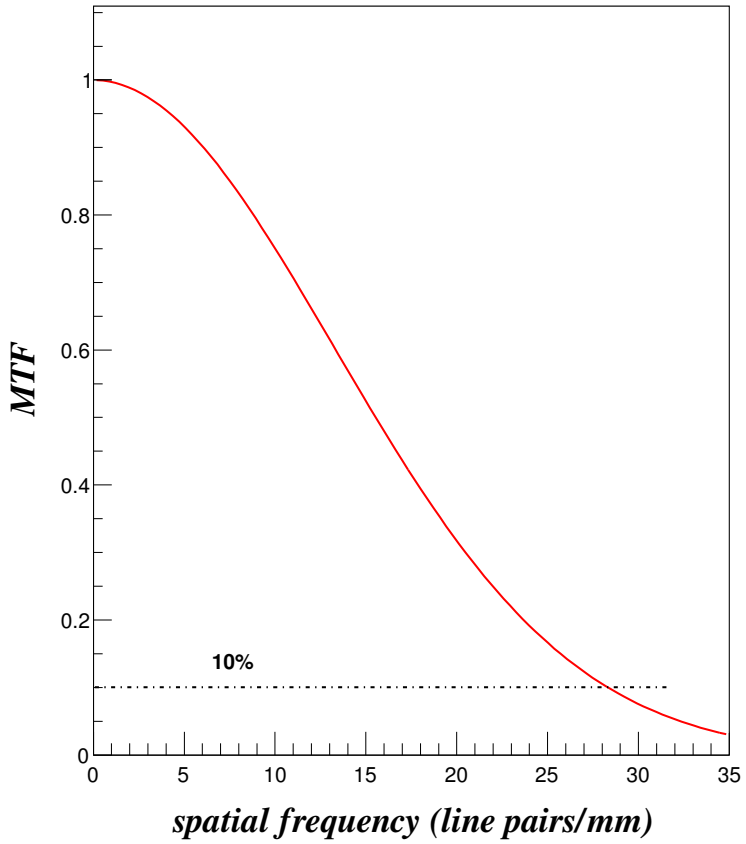

Figure 5. MTF derived from the selected region from figure 4. The curve crosses the 10% contrast cutoff at 28 line pairs per mm, which corresponds to a spatial resolution of 18 μm.

which precludes the mode for standard experiments of the IMAT user programme, certainly for tomography applications. The tests showed, however, that (1) the MCP cameras works as expected in centroiding mode on the beamline; (2) there are no beamline conditions that would make it impossible to achieve high spatial resolution on IMAT. This result is in particular important in view of a planned design and construction of a new optical camera system for spatial resolutions down to 20 μm. The tests performed on IMAT aimed at providing a white-beam image. In principle, the centroiding mode can be used for energy-selective imaging, by restricting the TOF range defined by the shutter ranges in table 1. This will, of course, extend the collection times even further. Hence this mode will be out of reach for IMAT but may be applicable at high intensity pulsed neutron sources, and on beamlines with an ever "colder" neutron spectrum than that of IMAT, to take advantage of higher neutron to electron conversion probabilities. In parallel, the detection efficiency could be further improved by (1) running the camera in event mode and by post-processing of the neutron data, in order to minimised the number of rejected neutrons; (2) by increasing the efficiency of present generation of neutron sensitive microchannel plates. The ongoing development of new MCP technology can increase the probability the neutrons are converted into charge especially for the thermal part of neutron spectrum. The distance to the detector active area can also be reduced allowing experiments with lower L/D values and thus higher neutron fluxes.

2018 JINST 13 C01039

Acknowledgments

G. Vitucci was supported by the CNR-STFC Agreement 2014-2020 (N. 3420 2014-2020) concerning collaboration in scientific research at the ISIS Spallation Neutron Source. The Siemens star test pattern was designed and provided by D.E. Pooley (ISIS Facility) which is gratefully acknowledged.

References

[1] T. Minniti et al., *Materials analysis opportunities on the new neutron imaging facility IMAT@ISIS*, 2012 *JINST* **11** C03014.

[2] W. Kockelmann et al., *Status of the neutron imaging and diffraction instrument IMAT*, *Phys. Proc.* **69** (2015) 71.

[3] *The Paul Scherrer Institute (PSI) — Neutron Imaging and Activation Group (NIAG) URL*, https://www.psi.ch/niag/.

[4] N. Kardjilov et al., *CONRAD-2: the new neutron imaging instrument at the Helmholtz-Zentrum Berlin*, *J. Appl. Cryst.* **49** (2016) 195.

[5] T. Reimann et al., *The new neutron grating interferometer at the ANTARES beamline: design, principles and applications*, *J. Appl. Cryst.* **49** (2016) 1488.

[6] D.S. Hussey et al., *A new cold neutron imaging instrument at NIST*, *Phys. Proc.* **69** (2015) 18.

[7] T. Shinohara et al., *Final design of the energy-resolved neutron imaging system RADEN at J-PARC*, *J. Phys. Conf. Ser.* **746** (2016) 012007.

[8] L. Santodonato et al., *The CG-1D neutron imaging beamline at the Oak Ridge National Laboratory High Flux Isotope Reactor*, *Phys. Proc.* **69** (2015) 104.

[9] M. Strobl, *The scope of the imaging instrument project ODIN at ESS*, *Phys. Proc.* **69** (2015) 18.

[10] W. Kockelmann et al., *Energy-selective neutron transmission imaging at a pulsed source*, *Nucl. Instrum. Meth.* **A 578** (2007) 421.

[11] M Strobl et al., *Advances in neutron radiography and tomography*, *J. Phys.* **D 42** (2009) 243001.

[12] C. Vallance et al., *Fast sensor for time-of-flight imaging applications*, *Phys. Chem. Chem. Phys.* **16** (2014) 383.

[13] A.S. Tremsin et al., *Detection efficiency, spatial and timing resolution of thermal and cold neutron counting MCP detectors*, *Nucl. Instrum. Meth.* **A 604** (2009) 140.

[14] A.S. Tremsin et al., *High resolution photon counting with MCP-Timepix quad parallel readout operating at* > 1 *KHz frame rates*, *IEEE Trans. Nucl. Sci.* **60** (2013) 578.

[15] D.E. Pooley et al., *Development of the "GP2" detector: modification of the PImMS CMOS sensor for energy-resolved neutron radiography*, *IEEE Trans. Nucl. Sci.* **64** (2017) 2970.

[16] A.S. Tremsin et al., *High-resolution strain mapping through time-of-flight neutron transmission diffraction with a microchannel plate neutron counting detector*, *Strain* **48** (2012) 296.

[17] J.R. Santisteban et al., *Phase analysis and imaging by TOF neutron transmission Proc. ICANS XV* **1** (2003) 239.

[18] J.R. Santisteban et al., *Characterization of textured materials by TOF transmission*, *Physica* **B 385** (2006) 636.

2018 JINST 13 C01039

[19] T. Minniti et al., *Characterization of the new neutron imaging and materials science facility IMAT*, to be published in *Nucl. Instrum. Meth.* A.

[20] A.S. Tremsin et al., *Optimization of a high count rate event counting detector with Microchannel Plates and quad Timepix readout*, *Nucl. Instrum. Meth.* **A 787** (2015) 20-25.

[21] X. Llopart et al., *Timepix, a 65 k programmable pixel readout chip for arrival time, energy and/or photon counting measurements*, *Nucl. Instrum. Meth.* **A 581** (2007) 485.

[22] A.S. Tremsin et al., *Neutron radiography with sub-15* μ*m resolution through event centroiding*, *Nucl. Instrum. Meth.* **A 688** (2006) 32.

[23] A.S. Tremsin et al., *High resolution neutron imaging capabilities with MCP/Timepix detector at BOA beamline at PSI*, *Nucl. Instrum. Meth.* **A 784** (2015) 486.

[24] S.H. Williams et al., *Detection system for microimaging with neutrons*, 2012 *JINST* **7** P02014.

[25] P. Trtik et al., *Improving the spatial resolution of neutron imaging at Paul Scherrer Institut — The neutron microscope project*, *Phys. Proc.* **69** (2015) 169.

2018 JINST 13 C01039

Paper V

Published by IOP Publishing for Sissa Medialab

Received: *November 17, 2017*
Accepted: *April 9, 2018*
Published: *April 27, 2018*

International workshop on Imaging II
4–8 September 2017
Varenna, Italy

Investigation of image distortion due to MCP electronic readout misalignment and correction via customized GUI application

G. Vitucci,[a,1] **T. Minniti,**[b] **A.S. Tremsin,**[c] **W. Kockelmann**[b] **and G. Gorini**[a]

[a] *University of Milano Bicocca, Department of Physics, Milan, 20125 Italy*
[b] *STFC-Rutherford Appleton Laboratory, ISIS Facility, Harwell, OX11 0QX U.K.*
[c] *University of California at Berkeley, Space Science Laboratory, Berkeley, CA, 94720 U.S.A.*

E-mail: g.vitucci@campus.unimib.it

Abstract: The MCP-based neutron counting detector is a novel device that allows high spatial resolution and time-resolved neutron radiography and tomography with epithermal, thermal and cold neutrons. Time resolution is possible by the high readout speeds of ~ 1200 frames/sec, allowing high resolution event counting with relatively high rates without spatial resolution degradation due to event overlaps. The electronic readout is based on a Timepix sensor, a CMOS pixel readout chip developed at CERN. Currently, a geometry of a quad Timepix detector is used with an active format of $28 \times 28\,\mathrm{mm}^2$ limited by the size of the Timepix quad (2×2 chips) readout. Measurements of a set of high-precision micrometers test samples have been performed at the Imaging and Materials Science & Engineering (IMAT) beamline operating at the ISIS spallation neutron source (U.K.). The aim of these experiments was the full characterization of the chip misalignment and of the gaps between each pad in the quad Timepix sensor. Such misalignment causes distortions of the recorded shape of the sample analyzed. We present in this work a post-processing image procedure that considers and corrects these effects. Results of the correction will be discussed and the efficacy of this method evaluated.

Keywords: Pattern recognition, cluster finding, calibration and fitting methods; Data processing methods; Analysis and statistical methods

[1]Corresponding author.

https://doi.org/10.1088/1748-0221/13/04/C04028

2018 JINST 13 C04028

Contents

2018 JINST 13 C04028

1 Introduction

The development of neutron imaging technology becomes more and more important driven by numerous advantages of neutron radiography and tomography, such as the possibility to penetrate and analyse specimens made of large-Z and dense materials or the high sensitivity to biological samples due to the exquisite sensitivity of neutrons to hydrogen.

There is a range of neutron imaging instruments available at large-scale facilities where such kind of analyses can be carried out. In this paper, we describe experiments performed at the Imaging and Materials Science & Engineering (IMAT) [1] beamline operating at the ISIS spallation neutron source (U.K.). On this instrument, different imaging cameras are available: a cooled CCD camera and a CMOS camera for white-beam neutron imaging, a gated CCD camera for energy-selective neutron imaging and two time-of-flight capable high-resolution pixel detectors based on MicroChannel Plate (MCP) [3] and CMOS sensors (GP2 detector [4]) for energy-dispersive neutron imaging. In this work, we will focus our attention on the MCP based neutron counting detector used on IMAT. The latter has useful peculiarities, among which one may list the high pixel resolution (55 µm) and the high readout speed of $\sim$ 1200 frames/sec that allows it to operate in event-timing mode. This mode permits to distinguish signals generated by neutrons of different time of arrival originated from the same neutron pulse.

The electronic readout of the MCP detector is based on a quad Timepix [5]. This is an ensemble of four Timepix chips (2×2) developed at CERN [6]. Such a configuration has the considerable advantage of providing a larger field of view with respect to the single chip arrangement. All the same, there are issues of the quad Timepix configuration for neutron tomography.

In this work, we will focus on the study of the image artifacts arising from the spatial gaps between Timepix chips and from the imperfect alignment of the four chips constituting the Quad Timepix readout.

2 Detector description

The IMAT MCP-based detector has been developed at the University of California at Berkeley in collaboration with Nova Scientific. The conversion of neutrons into electrons is made by a ^{10}B and gadolinium doped microchannel plate (8 µm pores on 11 µm centers, 100:1 L/D, 33 mm diameter) followed by a second, standard glass MCPs (10 mm pores on 12 µm center, 40:1 L/D, 33 mm diameter). With such configuration, the MCP detector is able to convert an incoming neutron into an electronic avalanche which is collected by the Timepix array.

The main advantage of this readout is the possibility to operate in "event timing" mode. In fact, every pixel of the chip has a 14 bit register able to store the time of a detected neutron with a $\sim$ 10 ns accuracy and a spatial resolution of 55 µm. This mode of Timepix operation allows energy-selective and energy-dispersive neutron imaging technique at the IMAT instrument [7].

The MCP neutron detector described in this paper is equipped with a quad Timepix that is an assembly of four Timepix, able to provide a net active area of 28×28 mm^2. The larger active area, compared to a single-chip detector, has the clear advantage of allowing the analysis of more voluminous samples. Nonetheless, there is a noticeable drawback with this configuration related to the misalignment and unavoidable gaps between chips which has important implications for imaging applications, figure 1.

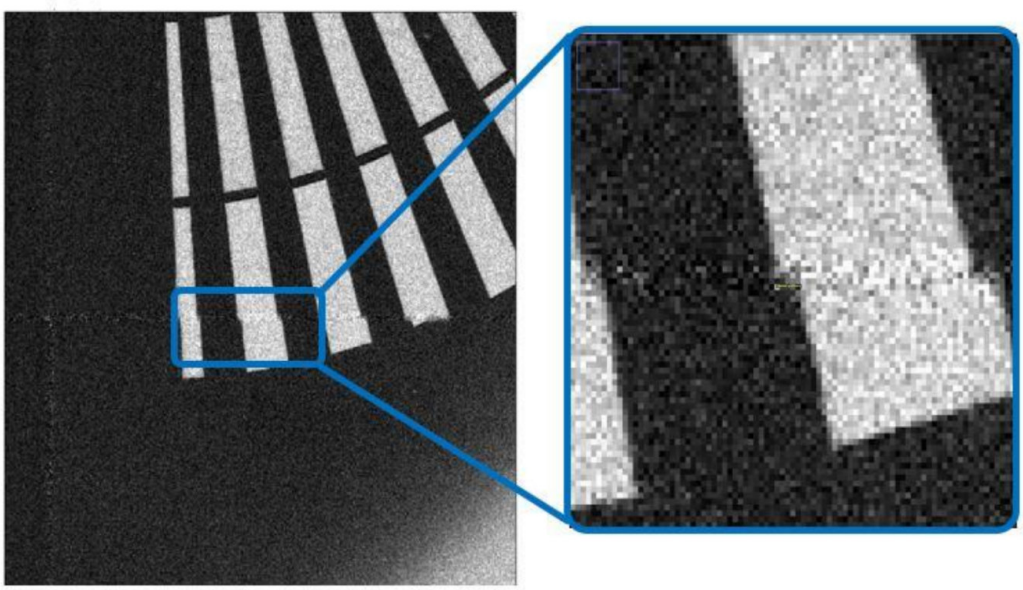

Figure 1. Radiography of the absorbing "Siemens star" test pattern showing the quad Timepix chip misalignment.

Such misalignment is intrinsic to the manufacture of the readout board made of four subsections, so it cannot be avoided in the hardware implementation. By contrast, the calculation of the gap geometry and corrections via post-processing operations on the acquired images are possible, by using calibration samples and an iterative algorithm, which has been developed in the MATLAB [8] software environment.

2018 JINST 13 C04028

3 Experimental setup

Spherical calibration samples were chosen to avoid errors of perspective, since different geometrical forms may result in incorrect specimen dimensions by the image analysis, if the neutron beam is not precisely orthogonal to the sample. The knowledge of the exact size of the sphere diameter is at the same time fundamental for developing the correction procedure. The teflon and chrome steel spheres used in this study have a diameter of 7.936 and 9.525 mm respectively. Both specimens have a tolerance close to 1 micrometer, as declared by the Bal-tec™ vendor [9] (see table 1) and thus largely below the size of one single readout pixel, i.e. 55 µm, to avoid the uncertainty of the digital discretization of the camera.

Table 1. Datasheet parameters of the precision spheres provided by the vendor.

Sphere material	**Diameter (mm)**	**Allowable Ball Diameter Variation**	**Deviation from Spherical Form**	**Surface Roughness Arithmetical Average**	**Basic Diameter Tolerance**	**Allowable Lot Diameter Variation**
Teflon	7.936	< 0.08 µm	< 0.08 µm	< 0.03 µm	0.76 µm	0.13 µm
Chrome steel	9.525	0.63 µm	0.63 µm	0.05 µm	2.54 µm	1.27 µm

A geometrical unsharpness of 44 µm was obtained selecting a collimation ratio L/D on IMAT of 1034 with a pinhole aperture D of 10 mm and a pinhole to sample distance L of 10.347 m. The maximum sample to camera distance was about 46 mm. This was deliberately set to reduce the unsharpness due to the scattering of the sample (neutron elastic cross section σ_s = 4.38 b compared to σ_{abs} = 0.012 b at 2.6 Å).

The sample material used for the first part of experiment is Teflon. The specimen was installed on top of an aluminium support (figure 2) and centrally aligned with respect to the gap of the quad Timepix. In fact, in order to perform the correction procedure, the specimen must be placed in correspondence of the contiguous borders of the electronic readout, as explained in the next section. The exposure time for sample and flat field radiographies was four hours each with a total collection time of about eight hours.

In the second part of the experiment, a chrome steel sphere (neutron elastic cross section σ_s = 10.98 b compared to σ_{abs} = 3.7 b at 2.6 Å) was used for tomography to test if the correction procedure was effective even with different sample materials.

4 Software correction

4.1 Issues description

The first step in the post-processing data analysis, after the data collection, consists of producing the white-beam neutron radiography of the specimen, to take advantage of the higher neutron counting statistics compared to energy-resolved neutron radiography data. These data clearly show the difference in the collection efficiency between the four Timepix pads, as well as the pixels (in black) in proximity of the gap between the chips where the charge collection is affected by the

2018 JINST 13 C04028

Figure 2. Setup of the experiment on IMAT. The sample is placed in front of the MCP detector and exposed to the neutron beam for eight hours.

electrons arriving at the gaps between the chips (figure 3). At the same time, the misalignment is clearly visible. In fact, when superposing a red circle with the exact diameter of the sphere as specified in the sample datasheet on to the image, the distortion and discrepancies between the two of them are noticeable (figure 3). A measurement of the diameter of the sphere image revealed that it was about 150 µm shorter than expected. The sample radiography is smaller because of the missing readout pixels in the middle part due to the presence of the gaps. The transmission image gives a clearer representation of the effect (figure top right), since the normalization cancels out the lack of uniformity due to both the different electric gains in each chip and the neutron beam disuniformities. However, the problem of the irregular shape due to the chips misalignment and the central gap still remains uncorrected.

4.2 Algorithm description

The algorithm was implemented in the MATLAB [8] programming environment. It consists of several steps which are execute automatically until the full iteration is completed. The main idea relies on the fact that there is a mathematical way to classify the roundness of a spherical specimen. This is called circularity factor and is defined as:

$$\mathbf{f_{circularity}} = \frac{\mathbf{4 \times \pi \times Area}}{\mathbf{Perimeter}^2} \tag{4.1}$$

and it is equal to one in case of a perfect circle, while it approaches zero when the form is more elongated toward one direction. Considering the desired optimum as being equal to one, we then operate a sequence of transformations on the image and calculate $f_{circularity}$ each time, to find the value closest to one. These transformations include rigid translations of each part of the original image associated to a single chip of the quad Timepix (figure 4), as well as rotations. The latter is performed with the bilinear interpolation method, where the output pixels resulting

2018 JINST 13 C04028

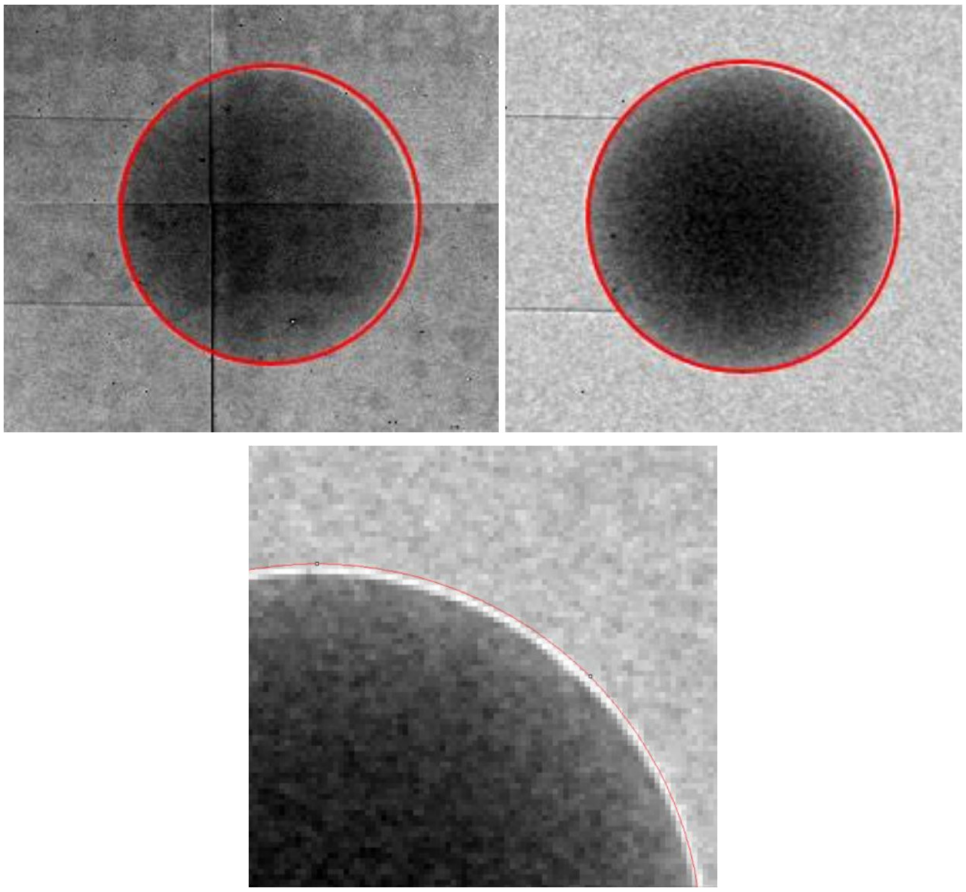

Figure 3. Radiography (top left), normalized (top right) and detailed view (bottom) image of the teflon sphere. The red circles represent the nominal diameter of the sphere.

from such transformations adopt the values of the weighted average of pixels in the nearest 2-by-2 neighborhood. Once the optimum set has been found, this can then be accepted as parameter set for the geometric corrections, since it reflects an intrinsic physical characteristic of the detector and there is no need to repeat the calculations. At the end, such transformations can be easily applied to other collected images stacks measured with the MCP camera in order to correct them.

Firstly, the program takes some input that is manually inserted by the user. The main parameters are the real size of the calibration sphere diameter which in our case was 7.937 mm, the size of the pixels in millimeters and the tolerance, meaning the maximum spatial range inside which the program classifies a found solution as acceptable. In this work, these two values were set to 55 micrometers, but they can be different, for instance in case the image has been acquired with a sub-pixel accuracy exploiting the "center of gravity algorithm" described in [5].

Secondly, the program opens and displays the radiography. Considering a standard output file, which has a resolution of 512×512 pixels, it splits the radiography into four parts, each one being a matrix of 256×256 pixels. Each portion represents the part of the sample which has been acquired by a single die of the quad Timepix. These quarters of a circle will be shifted in vertical and horizontal directions with a step size of a single pixel and rotated with a step of 0.25 degrees, to form a slightly different image every time. The new column or row that is created in the modified

2018 JINST 13 C04028

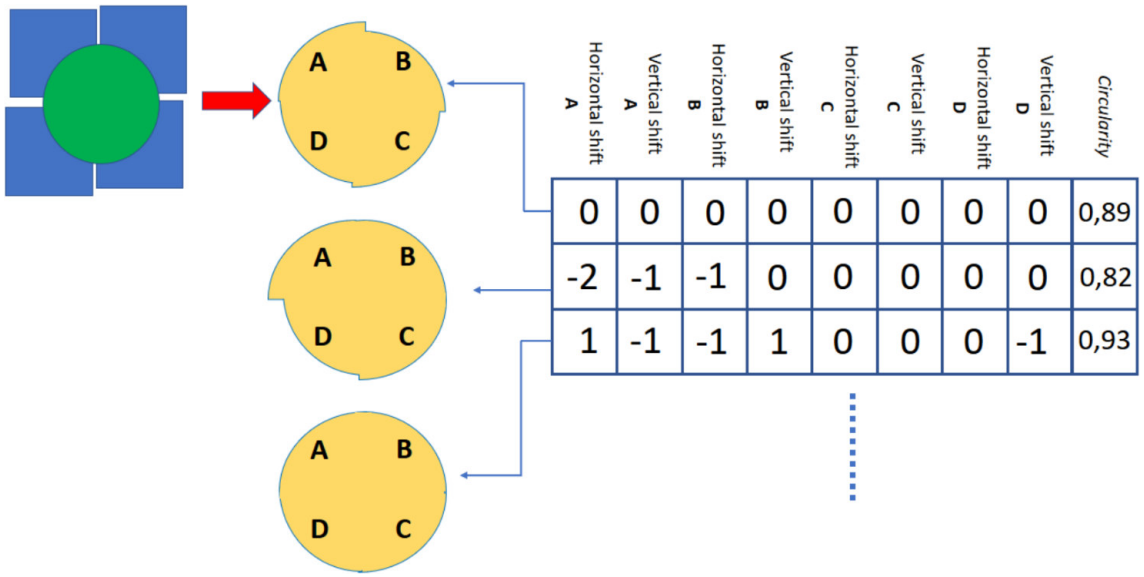

Figure 4. Sketch of the program operations on the acquired image. The original (on the top) is a deformed circle, because of the misalignment between the pads (A, B, C, D). The script calculates the circularity factor (0.89 in the example), then tries several combinations of parameters to obtain a new circularity factor. In the figure, it first moves the part A (related to the part of the sphere acquired by the PAD A) two pixels to the left and one pixel down; at the same time, it moves the part B one pixel to the left; then it calculates the circularity factor again. The same procedure is repeated until all the combinations have been executed.

image at the border of the sector when the shift is applied will be the exact copy of the adjacent one. This is the easiest approach, but other solutions, such as a linear interpolation between the two borders at the extremities of two adjacent sectors may be implemented as well. The maximum limit of the translations and rotations that have to be executed is very important. In fact, as twelve is the number of degrees of freedom for the full transformation, i.e. two translation directions (vertical and horizontal) plus the rotation for each of the four pads, the formula to calculate all the possible sets of parameters is:

$$P = m^d$$

where P is the total number of sets, m is the maximum shift to apply to each sector (in pixels and degrees), d is the number of degrees of freedom. In this work, the factor m has been set to 4 (no shift plus three shifts of one pixel each), because the gap between the pads was known to be around 150 micrometers. Even in this way, the number of sets was greater than 16 million. This means that care must be taken to set the parameters of this equation and avoid a huge number of images that could not be elaborated. Also, a substantial code optimization is needed.

Once the transformations have been applied to all the sectors the image is recomposed and, by using the "regionprops" function implemented in the MATLAB Image Processing Toolbox™ [10], and which is able to recognize circular objects inside an image and to calculate their perimeter and area, a new circularity factor is determined. If this value is closer to one than the previous iterative step, the new set of parameters associated to such result is saved. The algorithm then continues until all the combinations have been tried. At the end, the best set is printed out and saved. In this way, the physical gap between the chips is calculated, because the sum of the absolute value of the

2018 JINST 13 C04028

shift in either vertical or horizontal direction for adjacent pads may be converted in a real distance simply multiplying for the step unit, i.e. the set pixel size. In this specific case the set pixel size was 55 µm.

4.3 Graphical User Interface

After the correct set of parameters has been found, it is possible to visualize the changes brought by the transformation with a customized Graphical User Interface, UFFA Part 1 (a Useful Fits Fixer Application). This program is designed to open a FITS file format (i.e. the standard image format generated by the detector after the acquisition) and to allow control on each of the four pads related to the quad Timepix dies. It is possible to translate the sectors in vertical and horizontal directions, rotate them, as well as zooming in the center to see the artifacts due to the misalignment (figure 5).

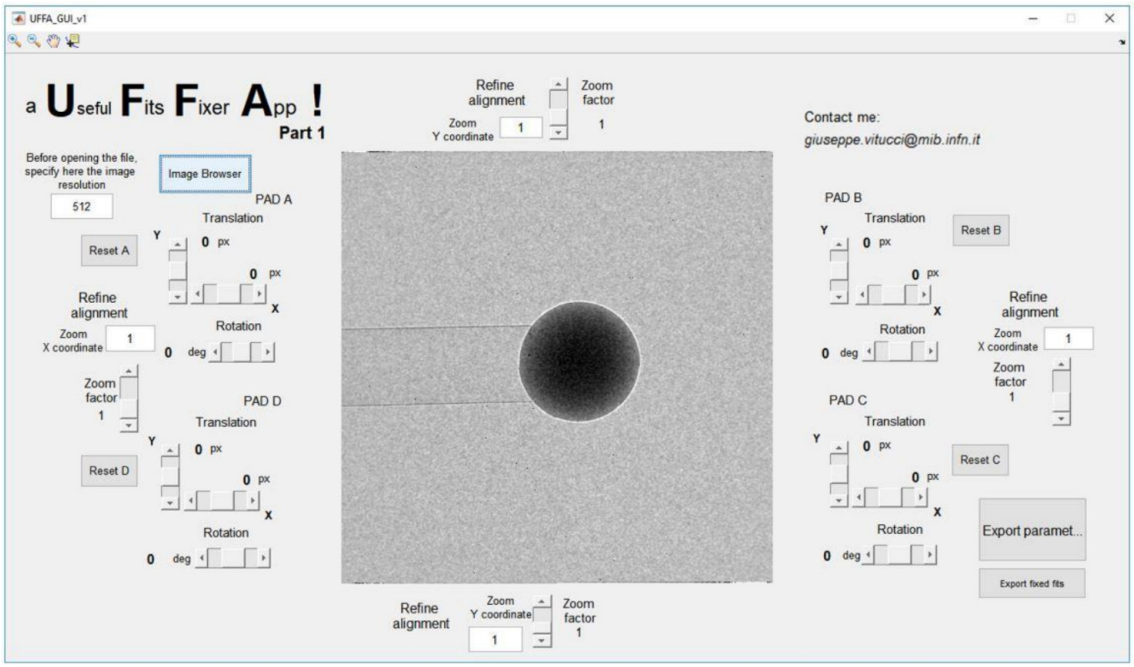

Figure 5. Graphical user interface of the program (UFFA Part 1). The "Part 1" assists the user with a live view of the changes applied to the image.

Once the correction set has been visualized and verified, the parameters can be exported in a text file and used as input into UFFA Part 2 (figure 6). This second analysis tool was developed to easily and rapidly apply the chip misalignment correction parameters extract by UFFA Part 1 to a large image dataset. This dataset can be, for instance, a full stack of neutron radiographies acquired during an energy-dispersive experiment or, more generally, a full set of projections of a neutron tomography. This is achieved by selecting the input folder dataset where all the images belonging to a single dataset are stored, and by specifying an output folder where the corrected dataset will be saved. The correction process is then executed automatically to all the files in the input folder.

5 Results

The best set of parameters was found after 40 hours of elaboration. The shifts and rotations were applied to the teflon ball radiography and the results are visualized in figure 7.

2018 JINST 13 C04028

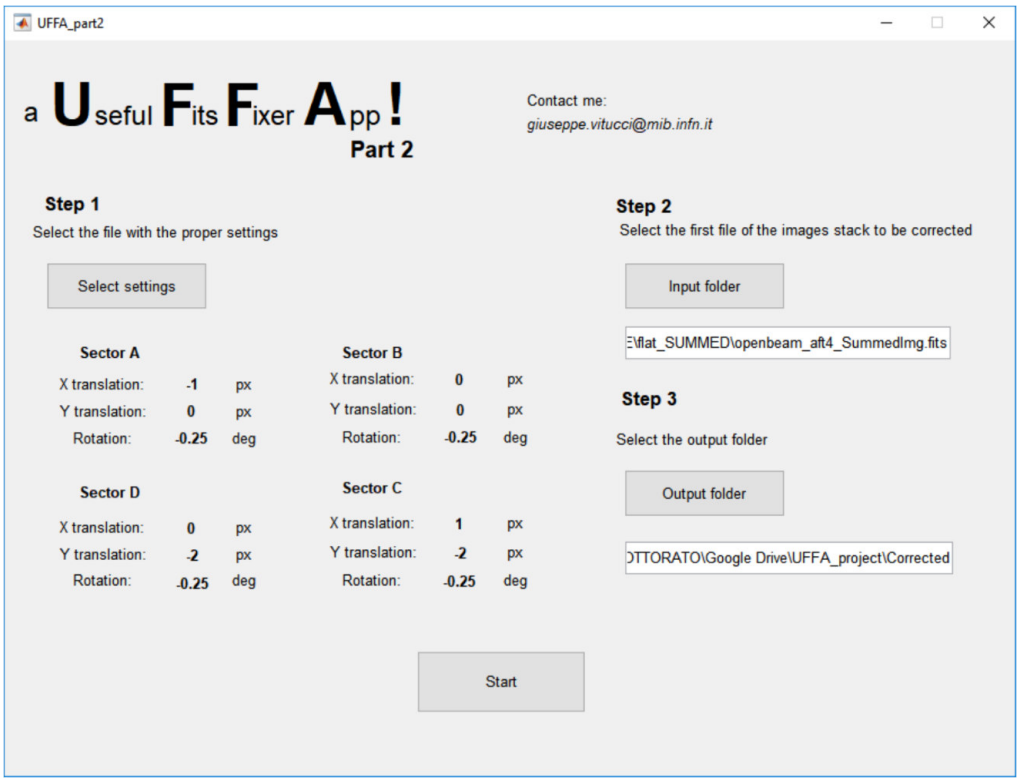

Figure 6. Graphical user interface of the program (UFFA Part 2). The "Part 2" automatically applies the changes to an entire stack of images in the input folder and save the results in an output folder.

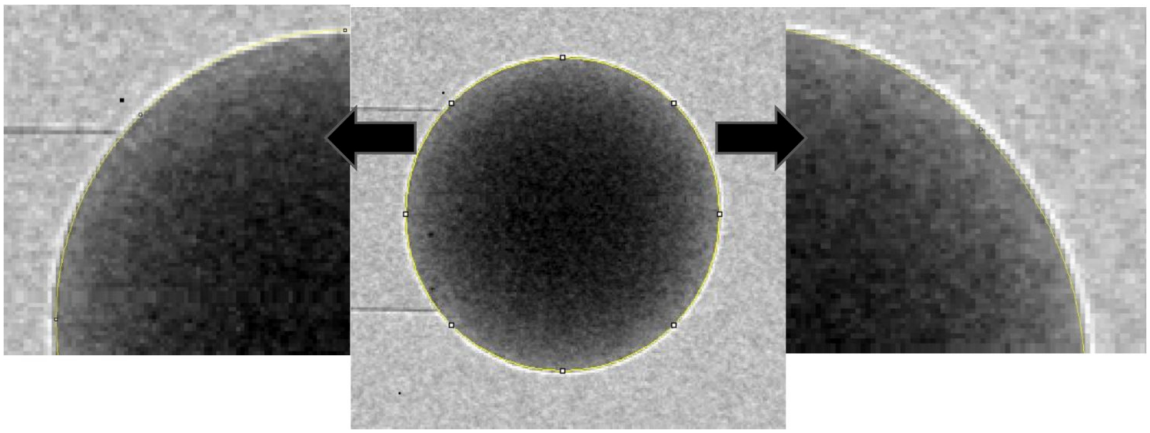

Vertical shift A	Horizontal shift A	Vertical shift B	Horizontal shift B	Vertical shift C	Horizontal shift C	Vertical shift D	Horizontal shift D	Rotation A	Rotation B	Rotation C	Rotation D
0	−1	0	0	−3	1	−3	0	0.25	0.25	0.25	0.25

Figure 7. Top. Detail of the radiography of the calibration sample. The contour of the sphere projection matches perfectly with the circle with the diameter specified by the vendor of the precision ball. Bottom: table of the parameters related to the quad Timepix implemented in the MCP-based neutron counting camera at the IMAT instrument. Each shift is equal to 55 µm, so that the gap between each pad can be calculated by the number of shifts. The higher the number of combinations tested, the more robust the result.

2018 JINST 13 C04028

The results found are obviously valid for the sample analyzed, but the robustness of this method can be verified with radiographies collected from different samples. For this reason, a full tomography of a different chrome steel precision sphere was collected. A set of 286 projections was taken with an exposure time of 180 seconds per frame over an angular range of 180 degrees. Each projection was corrected using the same parameters obtained for the teflon sphere case. Indeed, the misalignment gap between the quad Timepix chips was assumed to be independent from the specimen itself.

At first the circularity factor was checked. Figure 8 shows the scatter data of this factor related to each projection of the tomography, and the linear regression for both the original and corrected datasets. In the second case, the average of the circularity value is higher and closer to one.

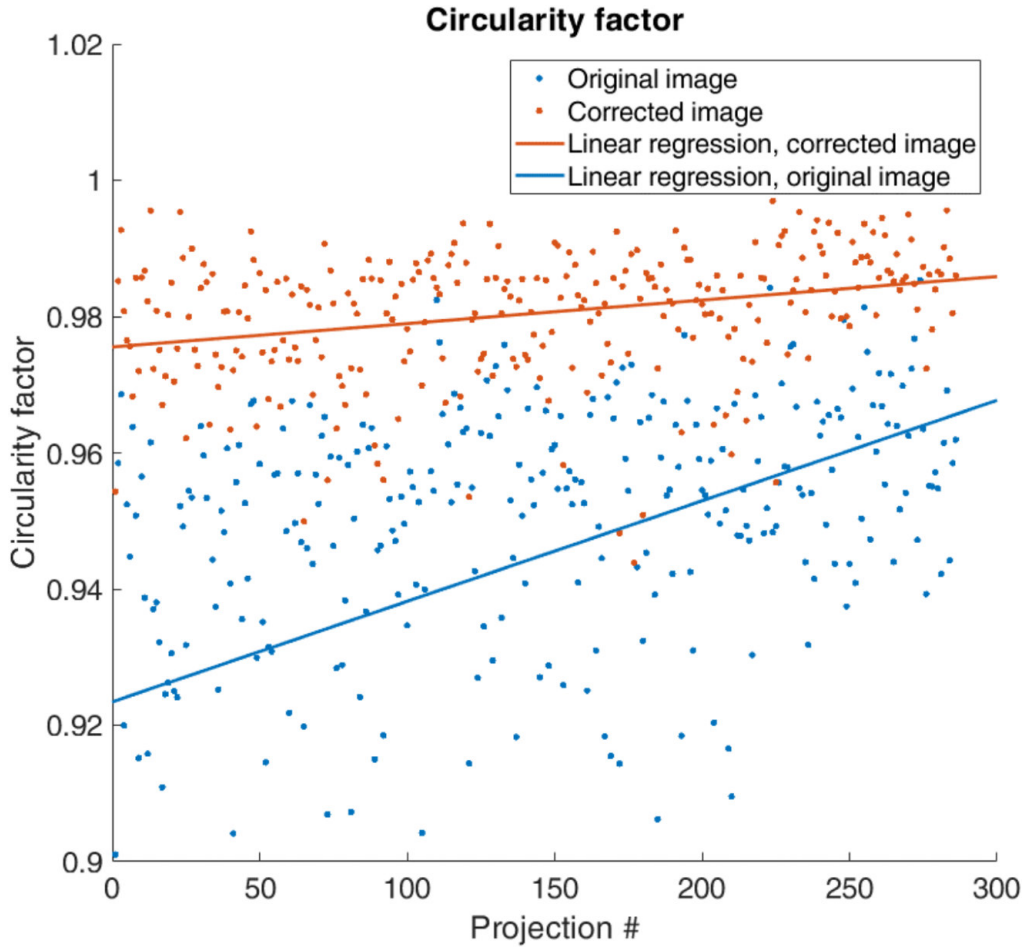

Figure 8. Circularity factor before and after the fix for a stack of 286 images. The circularity factor of all the images in the corrected stack is higher and almost constant in the range of 0.98 ± 0.02, while the circularity factor of the images in the original stack is lower and ranges over a wider interval (from 0.92 to 0.96).

A second consistency check comes from the measurement of the diameter of the sample projections (figure 9). The majority of the corrected projections lies inside the interval of tolerance of ± 55 µm determined by the discretization of the image through the matrix of pixels. According to the vendor, the chrome steel sphere had a diameter of 9.525 mm.

2018 JINST 13 C04028

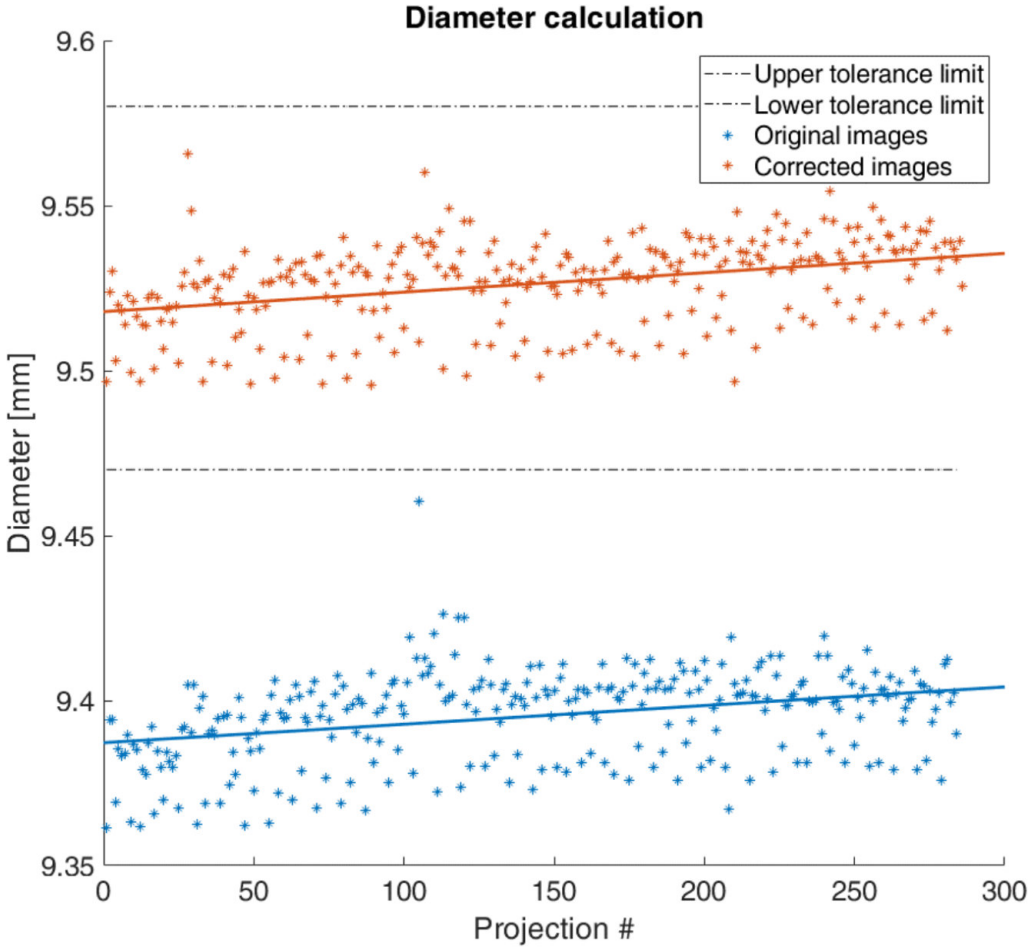

Figure 9. Diameter calculation of the sample projections by image analysis, both original and corrected. The corrected stack has images whose diameters agree with the specifications defined by the vendor, while in the original stack the sphere appears to be 0.15 mm smaller.

A final check was obtained by the evaluation of the diameter of the sphere extracted from the volume rendered data set after the computed tomography (CT) reconstruction of the specimen. In particular, a CT reconstruction based on SART (simultaneous algebraic reconstruction technique) algorithm was used by means of the Octopus software [11]. A better signal to noise ratio on the reconstructed slices was obtained by the SART algorithm compared with the filtered back-projection (FBP) algorithm. A post-process three dimensions $5 \times 5 \times 5$ median filter was applied to the reconstructed slices to reduce noise that is generated by the reconstruction algorithm. The subsequent volume rendering and segmentation was performed by the use of VgStudio Max software [12].

Figure 10 shows the result of the volume rendering of the tomography dataset which was corrected for the gap between the quad Timepix chips.

For comparison, the original tomography dataset was also analyzed and results are reported in table 2.

It is worth noting that closer results with respect to the certified sphere diameter of 9.525 mm were extracted for the corrected dataset as also reported in the 2D analysis case of figure 9.

2018 JINST 13 C04028

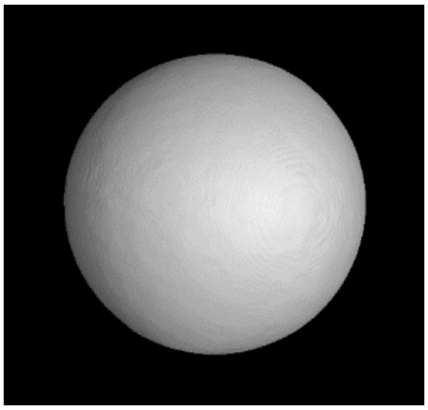

Figure 10. Volume rendered data set of the micrometric chrome steel sphere corrected for the quad Timepix chip gap. The nominal diameter of the sphere is 9.525 mm. The reconstructed object does not exhibit significant distortions from chip misalignments.

Table 2. Comparison of the result obtained for the original and corrected datasets.

Type of dataset	Volume (mm^3)	Deviation (mm^3)	Diameter (mm)
original	431.74	24.20	9.38±0.17
corrected	456.48	16.69	9.55±0.12

6 Conclusions

In this paper, a practical approach for the evaluation and post-process correction of the chips misalignment in quad Timepix electronic readout has been presented. The algorithm is capable of finding the gap parameters by trying several different combinations of parameters to reconstruct the original shape of a spherical calibration sample. The higher the number of trial combinations, the better is the achieved precision. In the future, some improvements will be addressed, such as the image reconstruction at the borders of each sector and within the gap areas and a code optimization for faster search of the optimum set. The correction procedures introduced here are straightforwardly extendable for future 2×N chip configurations which are in discussion as extensions of the current 2×2 formation, with one side of a chip being unavailable for tiling due to Timepix wirebonding.

Acknowledgments

We acknowledge the CNR-STFC Agreement 2014–2020 (N. 3420 2014-2020) concerning collaboration in scientific research at the ISIS Spallation Neutron Source, for financial support. We would like to thank Dr A. Kaestner for useful and constructive discussions.

References

[1] T. Minniti et al., *Materials analysis opportunities on the new neutron imaging facility IMAT@ISIS*, 2016 *JINST* **11** C03014.

[2] W. Kockelmann et al., *Status of the neutron imaging and diffraction instrument IMAT*, *Phys. Procedia* **69** (2015) 71.

2018 JINST 13 C04028

[3] A.S. Tremsin et al., *Detection efficiency, spatial and timing resolution of thermal and cold neutron counting MCP detectors*, *Nucl. Instrum. Meth.* **A 604** (2009) 140.

[4] C. Vallance et al., *Fast sensors for time-of-flight imaging applications*, *Phys. Chem. Chem. Phys.* **16** (2014) 383.

[5] A.S. Tremsin, J.V. Vallerga, J.B. McPhate, O.H.W. Siegmund and R. Raffanti, *High resolution photon counting with MCP-timepix quad parallel readout operating at* > 1 *KHz frame rates*, *IEEE Trans. Nucl. Sci.* **60** (2013) 578.

[6] X. Llopart, R. Ballabriga, M. Campbell, L. Tlustos and W. Wong, *Timepix, a* 65 *k programmable pixel readout chip for arrival time, energy and/or photon counting measurements*, *Nucl. Instrum. Meth.* **A 581** (2007) 485 [*Erratum ibid.* **A 585** (2008) 106].

[7] T. Minniti, K. Watanabe, G. Burca, D.E. Pooley and W. Kockelmann, *Characterization of the new neutron imaging and materials science facility IMAT*, *Nucl. Instrum. Meth.* **A 888** (2018) 184.

[8] MathWorks, (2018) https://www.mathworks.com/products/matlab.html.

[9] Bal-Tec™, (2018) http://www.precisionballs.com/.

[10] MathWorks, *Image Processing Toolbox™ Reference*, (2018) and online pdf version at https://it.mathworks.com/help/pdf_doc/images/images_ref.pdf.

[11] Octopus Imaging Software, (2018) https://octopusimaging.eu/.

[12] Volume Graphics, *VGStudio MAX*, (2018) https://www.volumegraphics.com/en/products/vgstudio-max.html.

2018 JINST 13 C04028